# Modeling of high electromagnetic field confinement metamaterials for both linear and non-linear applications

Elie Atie

SPIM

Thèse de Doctorat

UFC

école doctorale **sciences pour l'ingénieur et microtechniques**

UNIVERSITÉ DE FRANCHE-COMTÉ

# Modeling of high electromagnetic field confinement metamaterials for both linear and non-linear applications

ELIE ATIE

SPIM

Thèse de Doctorat

école doctorale **sciences pour l'ingénieur et microtechniques**

UNIVERSITÉ DE FRANCHE-COMTÉ

N°

THÈSE présentée par

ELIE ATIE

pour obtenir le

Grade de Docteur de
l'Université de Franche-Comté

Spécialité : **Optics and photonics**

# Modeling of high electromagnetic field confinement metamaterials for both linear and non-linear applications

Soutenue publiquement le 22 Decembre 2016 devant le Jury composé de :

| | | |
|---|---|---|
| FOUAD EL HAJ HASSAN | Rapporteur | Professeur à l'Université Libanaise, Liban |
| BRAHIM GUIZAL | Rapporteur | Professeur à l'Univesité de Montpellier II, France |
| AYMAN AL FALOU | Examinateur | Professeur à l'ISEN-Brest, France |
| WEHBE FARAH | Examinateur | Professeur à l'Universté St Joseph, Liban |
| FADI BAIDA | Directeur de thèse | Professeur à l'Université de Franche Comté, France |
| TONY TANNOUS | Co-Directeur de thèse | Professeur à l'Université de Balamand, Liban |

# Contents

# List of Figures

# List of Tables

# List of abreviations

| | |
|---|---|
| **BNA** | Bowtie Nano-Aperture |
| **FDTD** | Finite Difference Time domain method |
| **PML** | Perfectly Matched Layer |
| **PBC** | Periodic Boundary Condition |
| **EO** | Electro-Optic |
| **PhC** | Photonic Crystal |
| **LN** | Lithium Niobate |
| **NL** | NonLinear |
| **FWHM** | Full-Width at Half-Maximum |
| **SHG** | Second Harmonic Generation |
| **SI** | Silicon |
| **InP** | Indium Phosphide |
| **ISIP** | Interferometric-Spatial-Phase-Imaging |
| **AFM** | Atomic Force Microscopy |
| **SNOM** | Scanning Near-field Optical Microscopy |

# Acknowledgment

Firstly, I would like to express my sincere gratitude to my advisors Prof. Fadi BAIDA and Dr. Tony TANNOUS for the continuous support of my Ph.D study and related research, for their patience, motivation, and immense knowledge. Their guidance helped me in all the time of research and writing of this thesis. I could not have imagined having a better advisors and mentors for my Ph.D study. A special thanks goes to Prof. Fadi BAIDA for all the time he gives to me for all our discussion, I could not imagine or express how my work would be without your supervision.

Besides my advisors, I would like to thank the rest of my thesis committee: Prof. Fouad EL HAJ HASSAN, Prof. Brahim GUIZAL, Prof. Ayman AL FALOU and Prof. Wehbe FARAH, for their insightful comments and encouragement, but also for the discussion which incited me to widen my research from various perspectives.

My sincere thanks also goes to Dr. Jihad ATTIEH, who provided me an opportunity to join the university of Balamand and was always supporting me during my trip. Without they precious support it would not be possible to conduct this research and even to start my Ph.D.

I thank my fellow colleagues in FEMTO-ST and at Balamand for the stimulating discussions, for all the fun we have had in the last four years. I will always remember our enjoyable moments.

Last but not the least, I would like also to thank, my parents without them and their support It wouldn't be easy to be what I am, my sisters for their deep support and for

all the grammar corrections they did and a special thanks goes to my special one Diala for her support, encouragement and being the shining spot when the life goes to be dark. To all of them I say "the best is yet to come".

# Chapter 1

# Introduction

## 1.1 Research background

Evolution of technology, especially in terms of fabrication techniques and tools, were the reason behind the appearance of optical structures at the nano-meter scale. The capacity of fabricating such very small structures has opened the way towards a new scientific field: Nano-optics. In definition, nano-optics is the study of the behavior of light on the nanometer scale, and of the interaction of nanometer-scale objects with light. Despite the importance of the fabrication development, a theoretical method was needed to completely study this new field and certainly to solve the Maxwell's equations. Many numerical methods have been developed to present a full study of the electromagnetic field's propagation and properties. The Finite Differential Time Domain method (FDTD), most used method nowadays, was invented in 1966 when Yee proposed an algorithm [2] to solve the Maxwell curl equations directly in time domain on a space discretized window. After that, Taflov and Broduin [3] reported the numerical stability criterion for Yee algorithm. This method has continued to develop and many researchers proposed

different tools to ameliorate it in order to have accurate results, of the electromagnetic problems, similar to the realistic ones.

However, in 1960 the first laser light was invented [4] which was the reason behind the appearance of new optics field which was completely unknown: the nonlinear (NL) optics. In fact the important of the laser in this field comes from its high density of focused injected beam, which was not possible using other injection methods. Due to this highly dense and focused beam, many NL effects appeared, these effects are related to the susceptibility tensor $\bar{\bar{\chi}}^2$, $\bar{\bar{\chi}}^3$ or to a higher order tensor. The first NL phenomena observed was the second harmonic generation, after that many other phenomena were discovered such as the third harmonic generation, four wave mixing, Kerr effect, Pockels effect (electro-optic (EO) effect) and many others. In fact, the appearance of the NL effect is related to the material used to fabricate the optical structure or it could be observed due to an application of other external physical parameters; for example the application of an electric field into a non-centrosymmetric substrate induce the appearance of the EO effect.

Light confinement inside some particular nano structure and the enhancement of light transmitted from the structure have lead to the appearance of both linear and non-linear effects, each depending on the overall condition of the study. Confinement of light in a sub-wavelength area, high optical transmittance factor and the resonance of the structure are the main interesting parameters of a nano-structure and define its importance to achieve different applications. Those nano-structure properties have attracted many researches to study the optical response of various structures and many geometrical shapes have been proposed in a way that cover a wide range of applications.

In our work, we are interested in both linear and NL effects, that appear due to the light confinement, for different structures. In the first part of our work, we will

show a new application using a well known nano-structure, the Bowtie Nano-Aperture antenna (BNA). This structure is widely discussed and shows interesting characteristics (resonance with high electric field confinement) making it useful in various domains and applications. However, in the second part of this thesis, we will discuss the electro optical effect, an effect related to the second order susceptibility tensor and appears in non-centrosymmetric material. The EO effect or Pockels effect appears due to the application of an external electric field into the NL medium which induces a linear variation of the medium refractive index. In this part, a different type of photonic crystal (PhC) will be proposed and different FDTD algorithms will be used to simulate the optical response of these structures that exhibit large electro-magnetic confinement.

## 1.2 Bowtie Nano-Aperture (BNA) antenna

BNA antenna has become a very well known structure in the field of nano-photonics due to their ability to confine light in a nano-metric region. This light confinement was the reason behind the usability of the BNA in a very wide range of fields and for various applications.

### 1.2.1 State of the art of the BNA

The appearance of nano-antennas dates back to the end of the 20th century. The idea of optical nano-antennas comes from their counterparts: the antennas in radio-frequency. Similar to the radio frequency antenna which transforms the electromagnetic waves into an electrical signal and vice versa, the optical nano-antenna is responsible for transforming a propagating beam of light into a focused light in a nano-metric zone and inversely. This

double functionality of the nano-antennas make them, similarly to the radio-frequency antenna, able to operate in two functional modes: emission and detection.

From the first appearance of the nano-antenna, many geometrical shapes were proposed in order to enhance the property of the antenna in a way that corresponds to a specific desired application. The beginning was with the study of the optical properties of a single nano-particle and nano-wires metallic structure [5, 6], by studying the role of metal cluster for surface-enhanced processes like Raman scattering [7, 8, 9]. Searching for a better enhancement of optical field and confinement of light have conducted researchers into developing more complex geometry, nano-antennas have not been fabricated only from one nano-structure as in the case of nano-wire, researchers have proposed the combination of two structures which have lead to the appearance of the dimers [10, 6] , Bowtie[11, 12], diabolo [13, 14] and BNA [15, 16, 17, 18, 19]. Combined structures have the advantage of confining light in the vicinity of the nano-antenna center (gap between the two structures) [20, 18] and these nano-antennas present a very interesting sensitivity to the light polarization[21, 22, 23]. Various geometrical shapes were proposed in order to fabricate a nano-antenna showing optical properties that fit with multiple applications see figure 1.1.

The difference between a single nano-structures and paired ones was studied by Cubukcu et al [24]. The authors discuss the cases of a nano-rod and a triangular nano-structure and compare them, respectively, to the dimers (composed of two nano-rods) and Bowtie (composed of two triangular shapes) nano-antennas. The study demonstrates that the field enhancement calculated in the cases of paired nano-structures is more pronounced than the field enhancement calculated using the single nano-structure as shown in figure 1.2.

The difference in terms of the light confinement in the vicinity of a 2 nm gap of a

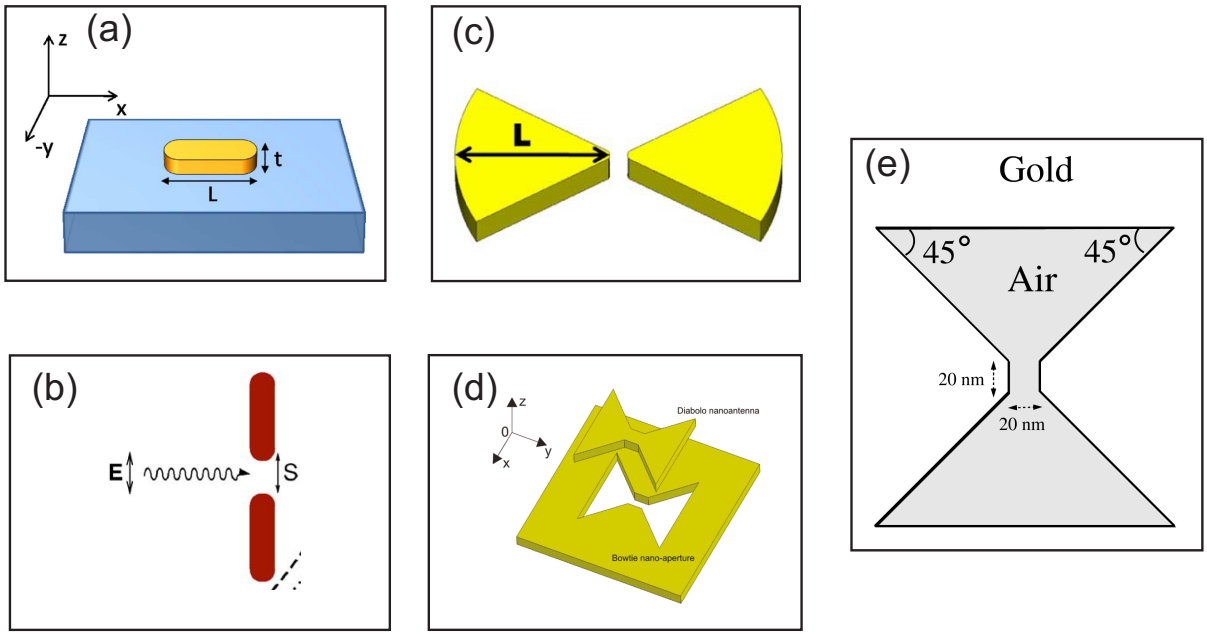


Figure 1.1: Figure showing different geometrical shapes of nano-antennas (a) nano-rod, (b) dimer, (c) Bowtie, (d) diabolo and (e) BNA.

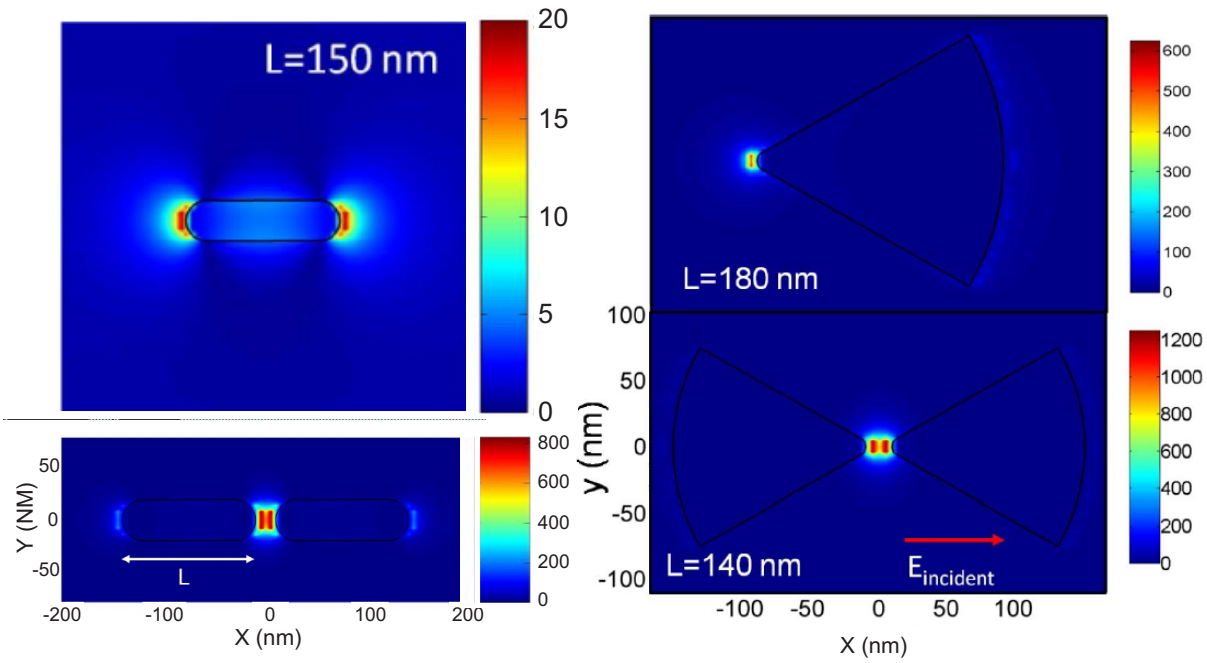


Figure 1.2: Difference in terms of electric field confinement between single and paired nano-structures.

Bowtie antenna and a dimers one was discussed in the study conducted by Hao et al [25]. The authors show that the enhancement in the case of a Bowtie antenna is higher than the one recorded by using a dimers antenna. Comparison between Bowtie shaped nano-antennas and other structures has been discussed in several other studies [26, 27].

However, the first appearance of the Bowtie antenna as an optical nano-antenna returns to the study presented by R. Grober et al [28] in 1997. In their study they have relied on the well-known characteristic of Bowtie antenna in the radio frequency domain, whereby a Bowtie is well-known to be an efficient planar antenna[29]. Their study demonstrated that the Bowtie antenna represents a new paradigm for near-field optical probes that combines spatial resolution well below the diffraction limit with transmission efficiency. Based on the study presented by R. Grober et al. [28], E. Oesterschulze et al. [30] conducted a study three years later in which they discussed a high transmission probe for scanning near-field optical microscopy that is based on a Bowtie antenna. The study investigates theoretically the transmission behavior of a Bowtie antenna probe based on a batch-fabricated silicon dioxide tip. In parallel, the study discussed the transmission efficiency and the field confinement, as functions of the antenna geometrical parameters and the gap dimension. This study has opened the way towards using the Bowtie aperture for various nano-optical applications due to its strong electric field energy localized in the gap and to its ability to be implemented at the apex of a fiber tip.

Thanks to the very interesting properties presented by E. Oesterschulze et al. [30], BNA antenna has attracted many researchers and many studies were published discussing its ability in various applications and domains. In 2002, K. Sendur et al [15] conducted a study in which they investigated the ability of the Bowtie aperture antenna to generate intense optical spots below the diffraction limit. It also discussed the effect of various parameters on the Bowtie aperture optical response, and compared the enhancement

of the field using square and circular apertures. An intensity enhancement of factor 5 was recorded numerically by using the FDTD simulation method. In addition, the study presented the Full-width at half-maximum (FWHM) and the maximum of the field intensity $|E|^2$ as a function of the aperture width and film thickness. They showed the variation of the FWHM and $|E|^2$ for a rectangular aperture, circular aperture and for a Bowtie aperture fig. 1.3(a). The optimum square aperture response was $1.45\ V^2.m^{-2}$ for a $35\ nm$ FWHM spot size while the optimum Bowtie antenna configuration gave a response of $55.7\ V^2.m^{-2}$ for the same spot size. This corresponds to a peak field intensity that is $38.4$ times larger for the Bowtie slot antenna than the square aperture on a gold, film. Furthermore, the study discussed the cases of two film metals: silver and gold as shown in figures 1.3(c) and (d), as well as the relation between the incidence angle and the field intensity $|E|^2$ as in figure 1.3(b).

As mentioned before, the geometrical shape of the structure has a great effects on the optical response and the confinement intensity. However, some geometrical parameters of the nano-structure also have a major effect on the optical response. The relation between the geometrical parameters of a BNA and: the resonance and the electric field confinement intensity, was discussed in the work conducted by I. Ibrahim [1] in 2010. In addition, the authors have demonstrated that the optical resonances of the BNA and the light confinement are due to the combination of a guided mode inside the aperture and Fabry-Perot modes along the metal thickness. Further more, the authors deduce an analytical formula from which the cut-off resonance wavelength (FP0) could be calculated:

$$\lambda_c(G, D) = \alpha D + \beta ln(G) + \delta D ln(G) + \gamma \tag{1.1}$$

where $\alpha$, $\beta$, $\delta$ and $\gamma$ are given in Table 1 of [1]. The study also presents the effect of the gap dimension and the lateral length of the BNA on its resonance. In figure 1.4(c) we see

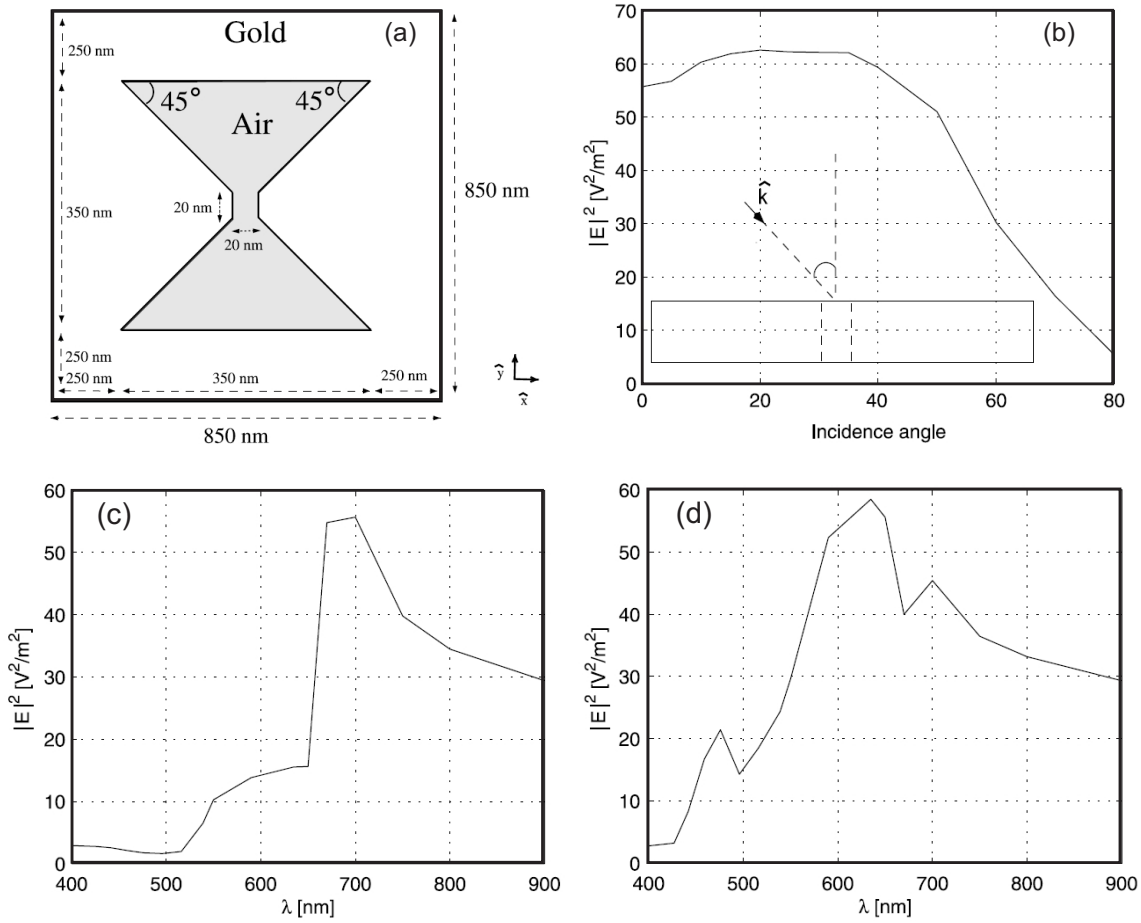


Figure 1.3: (a) Schematic of the BNA, (b) response of the Bowtie aperture for various incidence angles, (c) and (d) wavelength dependence of the maximum $|E|^2$ value for Bowtie aperture on gold and silver films, respectively.

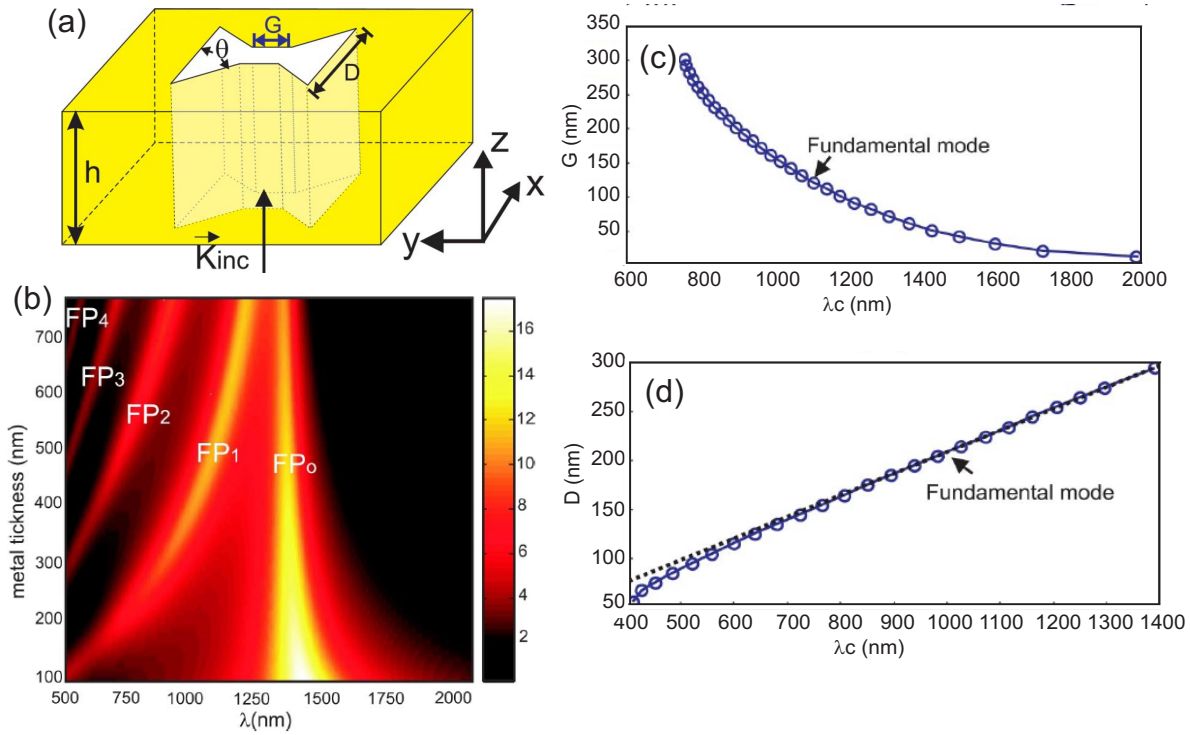


Figure 1.4: (a) Figure representing the Bowtie nano-aperture antenna, (b) Transmission spectrum of the BNA as a function of the metal-layer thickness obtained through 3D-FDTD code, (c) resonance wavelength variation as a function of the gap dimension $G$ with $D = 305\ nm$ and (d) resonance wavelength variation as a function of the lateral length $D$ with $G = 55\ nm$ [1].

that for a known lateral length $D = 305\ nm$ the resonance wavelength is red shifted when the gap dimension $G$ decreases, while in figure 1.4(d) the resonance wavelength is blue shifted when $D$ decreases. The authors noted that similar results are obtained for various materials. However, the metal thickness of the Bowtie aperture had a negligible effect on the cut-off resonance wavelength, as shown in figure 1.4(b).

On the other hand, other researchers were interested in studying the ability of using the BNA in many fields and various applications. A BNA used in nano-lithography was discussed by L.Wang et al [31]. The study demonstrates that holes of sub-$50\ nm$ dimension could be produced in photo-resist, using a BNA with a $30\ nm$ gap size fabricated in aluminum thin films coated on quartz substrates and illuminated by a $355\ nm$ laser beam polarized in the direction across the gap.

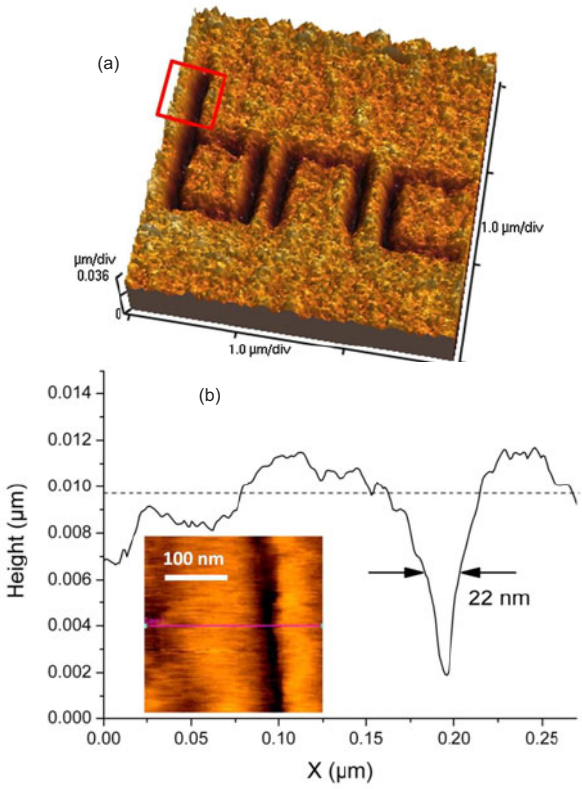


Figure 1.5: (a) AFM images of a lithography made on a photo-resist using the BNA (b) cross-sectional scan of the pattern taken from the position illustrated in the inset. Inset is the zoom-in image of the square area in (a).

In 2014 X. Wen et al [32] published their own research about using a BNA in nano-lithography. The study is based on combining the BNA nano-lithography system with an interferometric-spatial-phase-imaging (ISIP) system. The ISIP system gives a high precision control over the distance between the aperture and the photo-resist. The authors conclude by demonstrating that using this combination a resolution of $22\ nm$ is achieved, as shown in figure 1.5.

The optical properties of the BNA has lead as well to study the ability of using the nano-antennas for optical trapping of small particles [33, 34, 35, 36, 37, 38]. A theoretical study, based on the calculation of Maxwell's stress tensor and completed through the FDTD simulation, was achieved by N. Hameed et al. [39]. The authors demonstrate that the optical force exerted by a BNA on a latex bead due to the light confinement in the

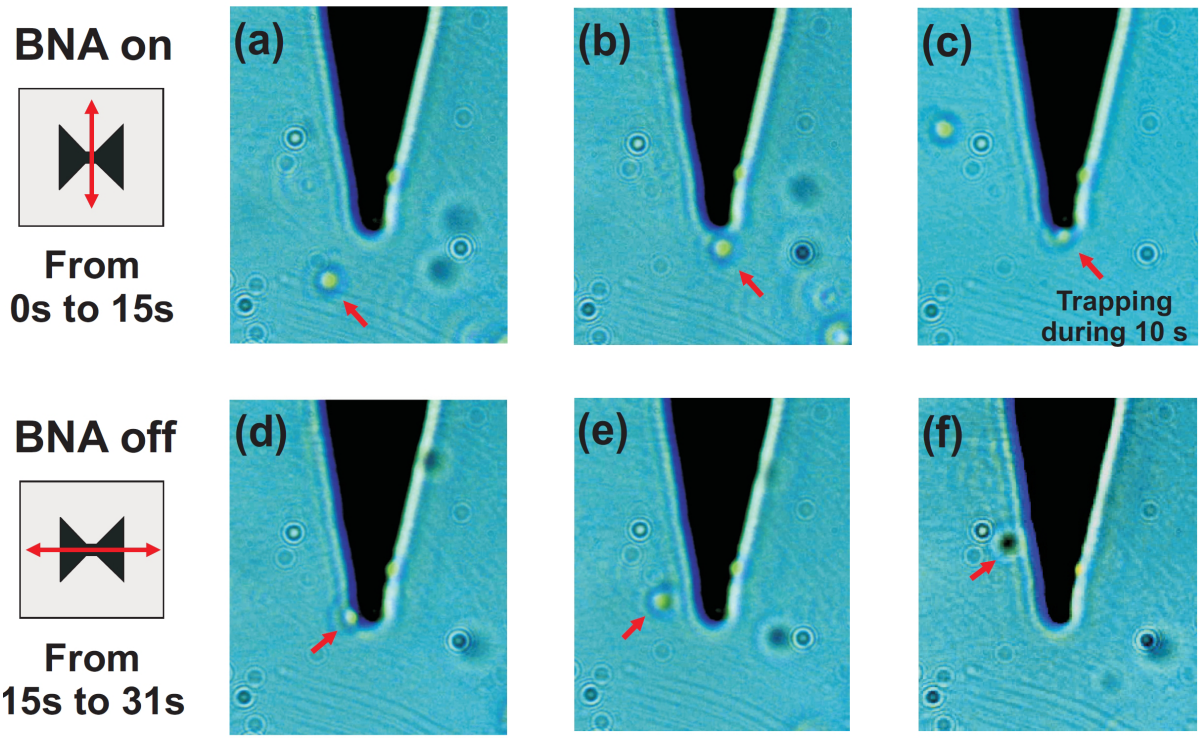


Figure 1.6: Demonstration of the 3D optical trapping of a 0.5 micrometer latex bead with a BNA on fiber tip, (a-c) the polarization of the in-fiber illumination ($\lambda = 1064\ nm$) is parallel to the polarization axis of the BNA: a particle is trapped at the tip apex by the BNA resonantly excited (time range from 0 to 15 seconds), (d-f) the input polarization is turned by $90^o$: the BNA is off-resonance. The initially trapped particle leaves the tip apex.

BNA vicinity is responsible for trapping the bead. The study also discusses the strength of the optical force as a function of the bead radius and from the distance between the BNA and the bead. On the other hand, an experimental study conducted by A. Eter et al. [40], presents the validation of the theoretical study presented in [39]. Due to the enhancement of the electric field in the gap center, the BNA, which has a lateral width $L = 165\ nm$ and a gap of $G = 35\ nm$ engraved at the apex of aluminum fiber tip, was able to trap a particle of radius $R = 250\ nm$ see figure 1.6.

BNA were discussed in many other studies and covered a wide range of applications and scientific fields. Studies have either discussed the advantage of using a BNA in a specific application or studied the optical response of the nano-aperture in a specific situation.

High field confinement of the electric field at the gap of the BNA of 47 $mW/\mu m^2$ is promising to achieve ultrahigh near-field optical recording, and the small spot size corresponds to storage densities up to 150 $Gbites/in^2$ as reported in [41]. However, high field confinement, resulting from the coupling between the BNA and individual fluorescence molecules, leads to enhanced molecules signal [42]. While coupling between the nano-aperture and a PhC [22] provides a path to overcome the diffraction limit in optical energy transfer to the nano-scale.

### 1.2.2 Thesis novelty

In all the applications in which the BNA is used, the later has to be placed in front of a sample or in a media with a relative refractive index. Therefore, the dependency between the optical response of the BNA and the sample position was not well discussed and in the applications in which the distance might be accurately measured, different types of mechanical tools such as AFM or shear force system have been used. In the third chapter of this thesis we will present the optical response of the BNA as a function of the distance from a sample placed in front of it. The results collected show a high sensitivity of the BNA to the distance from a sample. The study paved the way towards using the BNA as an optical tool promising an alternative to the mechanical nano-positioning techniques.

## 1.3 Electro-Optic effect

The EO effect is the change in refractive index of a material induced by the presence of a static (or low-frequency) electric field. In some materials, the change in refractive index depends linearly on the strength of the applied electric field. This change is known as

the linear EO effect or Pockels effect [43]. The EO effect involves on the second order NL susceptibility tensor, thus, it can only occur for non-centrosymmetric material such as Lithium Niobate (LN).

### 1.3.1 State of the art of the Pockels effect

NL effects were widely studied and they are the reason behind several applications used nowadays. NL effects consist on the interaction of a light beam when passing through a NL medium which leads to the modification of the beam frequency. The modulation of light occurs either due to an intrinsic property of the medium itself, as in the case of second harmonic generation SHG [44, 45] , Raman effects [46, 47], four-wave mixing [48, 49] or due to the application of an external motif as in the case of Pockels effect [50, 51, 52] and Kerr effect [49, 53]. SHG an Pockels effects are both depending on the second order NL susceptibility tensor thus they occur only for non-centrosymetric materials. However the Kerr effect and four-wave-mixing are related to the third order susceptibility tensor, therefore, they are present for all materials.

NL devices have been developed for applications in various domains such as communications, analog and digital signal processing, information processing, optical computing, and sensing. Among the NL devices, we mention: phase and amplitude modulators [54, 55], multiplexers [56], switch arrays [57, 58], couplers [59, 60], polarization controllers [61], deflectors [62, 63] and sensors for detecting temperature [64, 65] etc... Due to the NL effects, those devices allow much higher modulation frequencies than other methods, such as mechanical shutters [66, 67], moving mirrors [68], or acousto-optic devices [69, 70], due to the faster time response.

The NL effects have been widely studied and many researchers were interested in the

modulation of light through the enhancement of different NL effects each depending on the material used and or the domain of interest. Mach Zehnder structures have been used for different applications, based on the NL effect, as most of the photonic sensors (the electric field sensor [71], temperature sensor [72],..). Despite the efficiency of the Mach Zehnder structure, they suffer from a relatively big dimension (long interaction length due to the small index change). Therefore, the integration of the NL optical devices in a photonic integrated circuits has become a real question that lead many researchers to use the PhC as a promising nano-structure able to enhance different NL effects due to its optical properties (slow light phenomena and the confinement of light in the structure [73]).

Many materials were proposed to be used in the fabrication of the optical modulators based on the PhC, such as silicon [74], organic polymer [75, 76, 77] and other semiconducting materials (A. Liu, et al. 2005) [78]. This lead to a high EO coefficient and a reduction in the interaction length while maintaining a high sensitivity to the applied voltage. In the study by Gu et al. [74] a high speed compact silicon modulator based on PhC waveguides was demonstrated experimentally to work at a low driving voltage with carrier injection, by exploiting the slow group velocity of light within the PhC for the modulation wavelength. The interaction length of this modulator is reduced significantly compared to conventional modulators by scaling down the interaction length from millimeters to 80 $\mu m$. Moreover, J. Wübern et al [79] present a study in which they show a slotted PhC waveguide infiltrated with an EO active polymer material that is extremely sensitive to refractive index changes in the slot region, and thus capable of modulation with voltages of just 0.8 V. Schmidt et al. [80] reported on EO modulation with a sub-1-V sensitivity in a PhC slab waveguide resonator by using amorphous polytetrafluoroethylene (Teflon) as an optical waveguide substrate and on top they deposit a thick film of an EO active material (poly-methylmethacrylate) in which they fabricate

the PhC.

Using silicon or polymer material to fabricate the optical modulator [81, 82] represented a good step towards achieving a real photonic integrated optical modulator. These materials show very interesting characteristics in terms of interaction length, area and low-power operation. Despite the progress achieved using these materials, the proposed optical modulators based on PhCs are not considered for commercial use because these materials still present temperature limitation, and rely on the relatively weak free carrier dispersion effect and they are typically long and require high driving powers for obtaining a significant modulation depth and thus exhibit an intrinsic NL phase modulation characteristic. Therefore, the LN is considered as a promising material to be used in the fabrication of an optical modulator and overcome the disadvantages presented by other materials. The LN presents some very interesting physical properties [83] such as EO, acousto-optic, piezo-electric and pyro-electric effects. However, one of the major limitations of the LN modulator technology is the strong etching resistance [83] and thus the missing ability to monolithically integrate modulators with other photonic components.

Studying the NL effects has been widely developed through many experimental studies. However, the theoretical studies, and certainly for the EO effects face some constraints. Many studies can be found in the literature presenting theoretical studies based on various simulation techniques for the SHG, the Kerr effect, or even for the four-wave-mixing. However, it is rare to find a theoretical study, discussing the EO effect or the modulation of nano-structure in order to enhance this effect, aside from the studies achieved by our research group. In fact, most of the research discussing the Pockels effect make their theoretical studies without taking into account the confinement of light inside the structure, as they are working in a bulk NL media. In our group, studying the electro optical effect started in 2005.

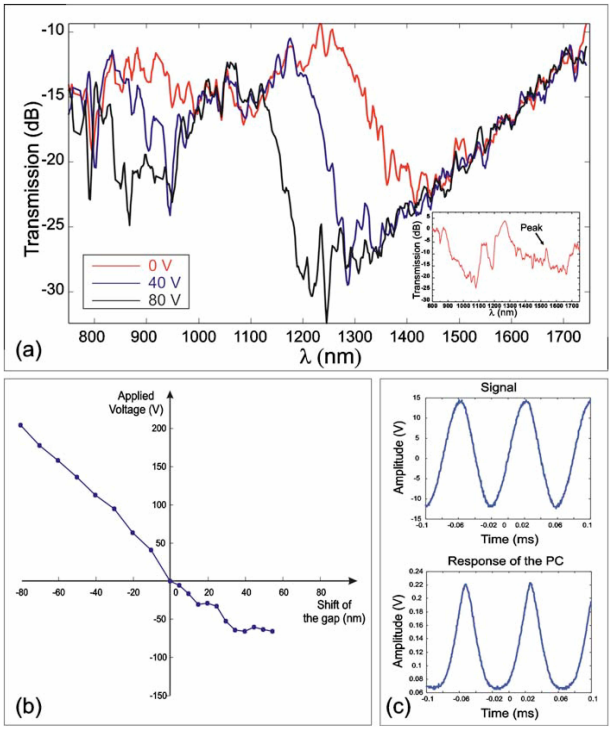


Figure 1.7: (a)Measured transmission of the PhC for different applied external voltages(0, 40, and 80 V). Inset: Measured transmission of a different LN substrate with the same geometry, where the central peak has been observed.(b) Wavelength shift measured for a $\lambda = 1300\ nm$ at 0 V as a function of external positive and negative voltages. (c) Modulation performance of the photonic crystal. The input is a sinusoidal signal at 13.5 V and 10 kHz. The output transmitted signal presents an extinction ratio of 5.2 dB. The measurement has been performed at a wavelength of 1550 nm for which the waveguide presents monomodal behavior.

The first study was achieved by Roussey et al. [51] in which they demonstrated how slow group velocities that are easily attainable at the band edge of PhC can drastically enhance the EO effect on tunable PhC components. The study showed a square lattice LN PhC, with $15 \times 15$ squared array of air holes etched by focused ion beam FIB on a gradient index LN waveguide, that has been used as an ultra-compact, low-voltage LN intensity modulator (see figure 1.7). They measured a shift of $312$ times bigger than the one predicted by classical Pockels effect applied to an unstructured LN substrate. The measured shift corresponds to a refractive index variation of $0.3$ for an applied external voltage of $80\ V$.

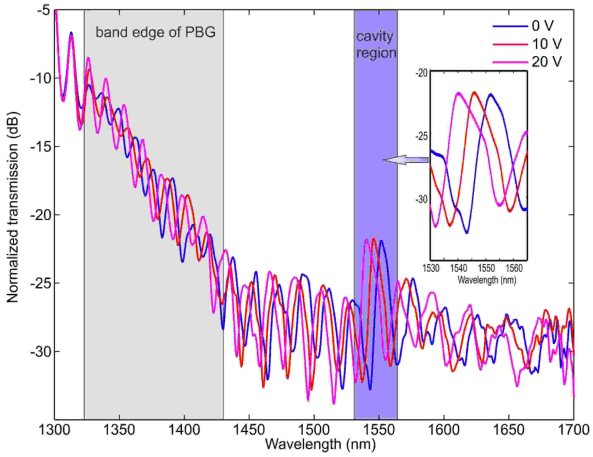


Figure 1.8: Normalized transmission spectra of the PhC cavity structure for three different applied voltage values (DC = 0 V, 10 V and 20 V) and the inset figure is the zoom of the cavity region.

In 2012, a second study by H. Lu et al [84, 85] theoretically and experimentally demonstrated the feasibility of a compact EO modulator on a LN PhC cavity structure with an active length of only $6\ \mu m$ made on an Annealed Proton Exchange (APE) LN waveguide with vertically deposited electrodes. The study showed that by using this configuration one can reach a tunability of $0.6\ nm/V$ and a relatively low driving electrical power ($10\ dBm$) (see figure 1.8). Based on their results, the authors state that more compact and low energy-consuming modulators may be realized by optimizing both the optical confinement of high quality factor PhC cavity and the electrical performance (approaching the electrodes and matching the impedance).

Moreover H. Lu et al. in 2013 [65] demonstrated that by using a PhC and by enhancing the pyro-electric effect, a temperature sensor could be realized. The enhancement of the pyro-electric effect generates an electric field in the PhC that depends on the temperature variation, which in its turn modifies the refractive index of the medium (due to the EO effect). The study presents a PhC cavity, of $5.2\ \mu m$ interaction-length on a LN air suspended membrane, used as a photonic temperature sensor with a temperature sensitivity of $0.359\ nm/^0C$ (see figure 1.9).

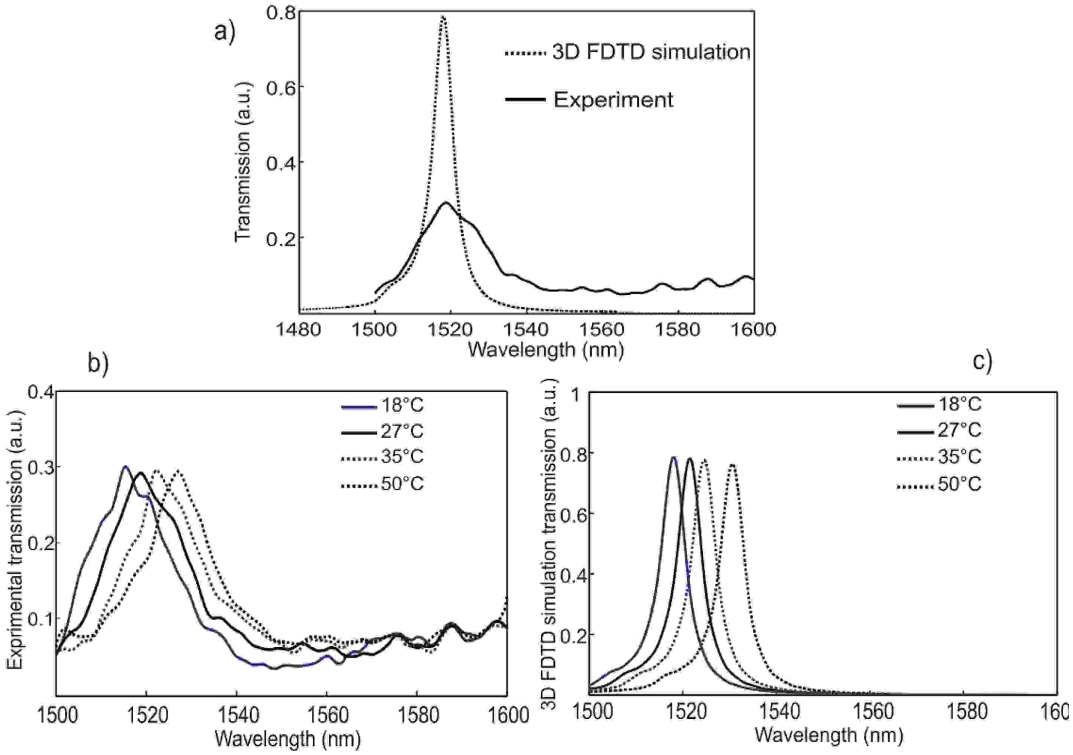


Figure 1.9: (a) Fabry-Perot resonance peak obtained by 3D-FDTD simulation of the device and the experimentally measured transmission, (b) experimentally measured transmission spectra of the peak as a function of the temperature, (c) 3D-FDTD simulation transmission spectra of the peak as a function of the temperature

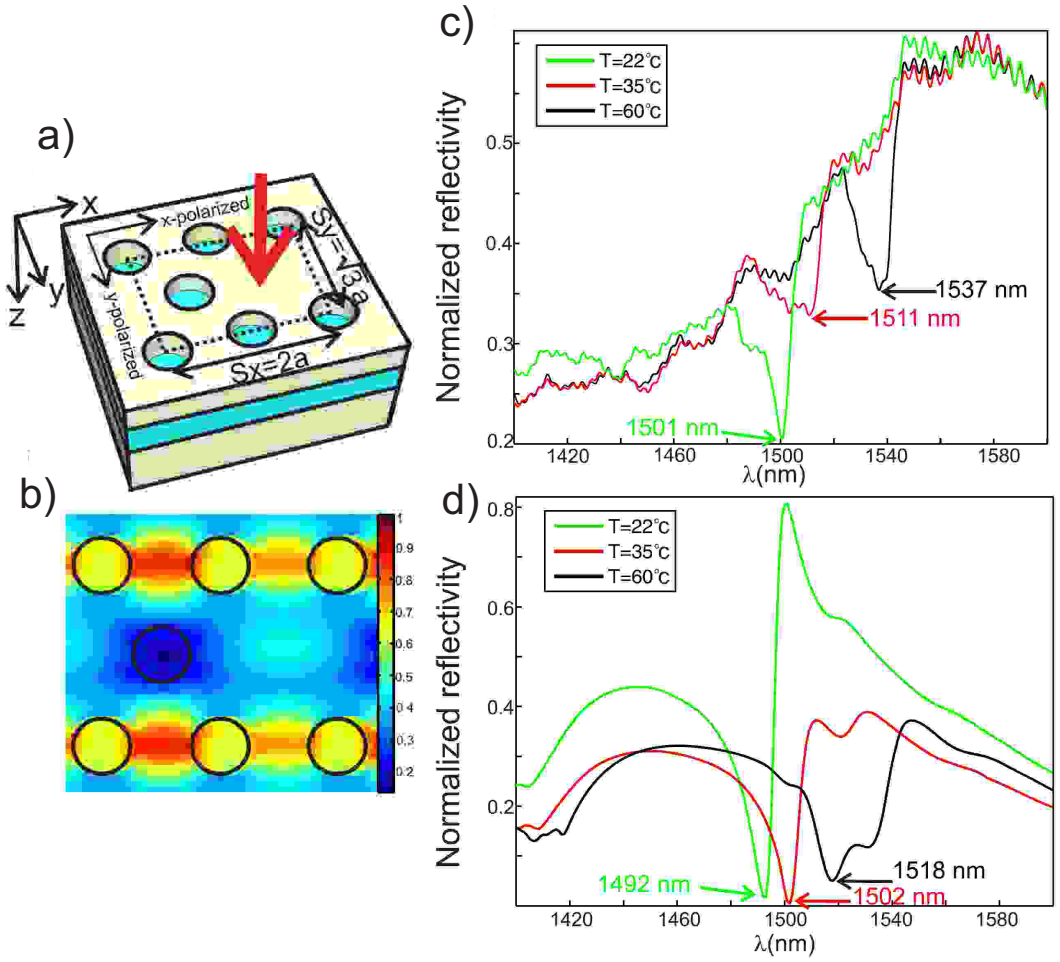


Figure 1.10: (a) Sketch of the Suzuki phase lattice fabricated on thin film LN. (b) Electric field amplitude distribution of one PhC cell. (c) Experimental normalized reflectivity of the Fano resonance in y-polarized excitation at different temperatures. (d) 3D-FDTD calculated finite size PhC reflectivity by y-polarized Gaussian beam incidence, with beam size of 15 $\mu m$ at different temperatures.

As well, during the Phd work of Wentao Qui [86], the authors studied a new applications using the EO effect for a PhC. The study was achieved by considering a Suzuki PhC structure (see figure 1.10(a)), fabricated on thin film LN, in order to discuss the ability of using this structure as a high-sensitivity temperature sensor. The results collected by both the numerical and experimental study showed good accordance. Due to the experimental study a sensitivity of 0.77 $nm/^oC$ with a PhC size of only 25 $\mu m \times 24$ $\mu m$ has been recorded, see figure 1.10(c) and (d).

Furthermore, a theoretical study discussing the case of a thin film LN rectangular lattice PhC has been discussed as well by Qui et al [87] (see figure 1.11). The authors discuss the case of variable PhC geometrical parameters in order to ensure the best resonance quality factor and to enable the high light confinement inside the structure. The structure approved to be a good candidate for electric field sensing. The study paves the way towards the improvement of the LN bulk devices such as sensors and modulators.

Theoretical studies of all works done by our research group since 2005 were based on the FDTD simulation method. The method used in [51, 65] was based on the calculation of the optical field factor in all the structure and a uniform modification of the refractive index of the media is then estimated and integrated into a second study that leads to a new optical response as a function of the applied electric field or heating temperature. However, in [87] a new method has been introduced in which a calculation of the variation of the refractive index is calculated at each grid cell of the simulation window which leads to a more accurate method for calculating the sensitivity of the structure to the applied electric field.

### 1.3.2 Thesis novelty

In our work, presented later in chapter 4, we will present different estimation methods to calculate the refractive index variation of the refractive index of the NL medium. In addition, we will showcase a new algorithm of an FDTD code in which we define a new self-consistent algorithm that is able, and during one simulation, to estimate and take into account the variation of the refractive index as a function of the applied electric field. The code is designed to modify the second order susceptibility tensor as a function of the applied electric field, and the obtained results show the optical response of the structure by taking into account the Pockels effect. Both NL and linear FDTD code algorithms will

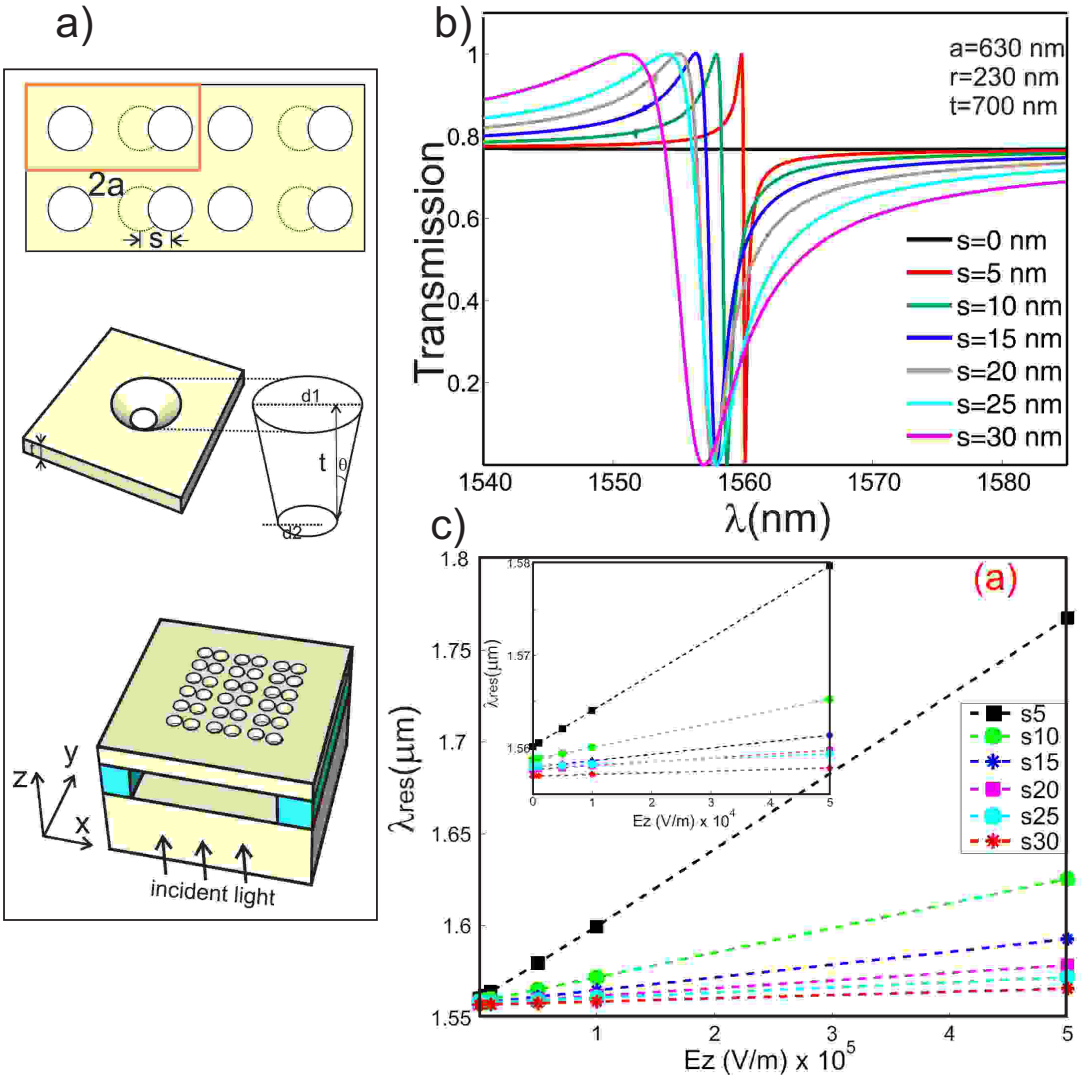


Figure 1.11: (a) Sketch of PhC fabricated on thin film LN presenting the different geometrical parameter. (b) FDTD calculation result of the normalized transmission spectra for $a = 630\ nm$, $r = 230\ nm$, $t = 700\ nm$ and varying $s$. (c) Numerically calculated plot showing the resonance wavelength as a function of the E-field (the inset show the zoom view of the first few data points) for infinite PhC air bridged structure with $a = 630\ nm$, $r = 230\ nm$, $t = 700\ nm$ and varying $s$.

be shown in the second chapter of this thesis.

## 1.4 Thesis partition

In addition to this present chapter, this thesis contains three other chapters. In the second chapter we will present the basic theory of Maxwell's equations which is the basis of the FDTD simulation. In addition we will present the algorithm of the FDTD code and the problematic and assumptions we took to develop a new FDTD code able to simulate, in a self-consistent way, the variation of the refractive index due to the EO property of the medium.

In chapter three, theoretical and experimental studies discussing the optical response sensitivity of a BNA to the distance separating it from a given substrate will be presented. Firstly, a theoretical study, using a homemade code 3D-FDTD will be shown. In the theoretical study we will discuss both operating modes of the BNA (collection and emission). The study will takes into account two types of substrate, with low and high refractive index, and the influence of the substrate optical index will be discussed. As well, both results, collected in near field and in far field, will be shown. However, the experimental study will only consider the case of a BNA operating in collection mode and facing a high optical index substrate. Further more, in the experimental study we show the results for two different BNA (having different geometrical parameters).

Chapter four is reserved to present the NL part of this thesis, the EO effect. In that chapter we will present a new FDTD self-consistent code used to calculate the optical response of a structure when applying a static electric field. We also discuss different assumptions to estimate the variation of the refractive index and all methods will be compared for various structures. The relationship between the optical field confinement

inside the structure and the EO effect will also be discussed in the chapter.

A general conclusion and future perspectives are presented in chapter five.

# Chapter 2

# Numerical tools and scientific problematic

## 2.1 Introduction

This chapter deals with the numerical method that will be used to model the light-matter interaction in the context of nano-optics domain. More precisely, we will be interested in simulating efficient linear and non-linear phenomena that can take place within nano-structures due to the confinement of the electromagnetic field inside such structures as it will be demonstrated in the next two chapters respectively. Therefore, in the current chapter we will present the property of our FDTD code that conduct to the modeling of plasmonic structure. In addition, we will discuss different dispersion models, in order to well describe the optical properties of metals over a wide range of wavelength. On the other hand, a nonlinear FDTD code will also be described which will allow the modeling of the electro-optic (EO) effect of nano-structures.

Various numerical methods were introduced to estimate the optical response of different structures. Those methods are based on solving Maxwell's equations and are divided into two groups: methods based on the resolution of Maxwell's equations in the frequency domain such as the plane wave expansion (PWE) method [88, 89], the transfer-matrix method (TMM) [90, 91] and the Rigorous coupled-wave analysis (RCWA) [92, 93], or in the spatial domain as the finite difference time domain (FDTD) method [94, 95, 96] and the finite elements method (FEM) [97, 98, 99], etc. The choice of a particular method depends on its domain of validity. In our work we are interested in using the Finite-Difference Time-Domain Method (FDTD). The main advantage of using the FDTD method in our work is that, by launching one calculation we can study the optical response of a defined structure in a wide frequency band using Fourier transformation to obtain the optical response as a function of the wavelength. By using FDTD method we can simulate the linear and nonlinear optical responses of the structure that we wish to study. We note that some restrictions on the structure geometry (the optical field confinement factror inside the structure) will be discussed on chapter 4.

Finite-Difference Time-Domain Method (FDTD) is a numerical tool first introduced by Yee [2] in 1966, in order to numerically solve the curl Maxwell's equations, consequently to study the propagation of electromagnetic fields, in time and space domain. Despite its simplicity and elegancy, Yee algorithm, has not received the sufficient interest immediately; High computational cost (memory and time consuming simulations) in addition to some inherent limits were the main reasons behind the lack of interest. In 1975 Taflov and Brodwin [3] reported the correct numerical stability criteria of the Yee algorithm. However the developments of the FDTD method and solving the inherent limits have continued through years. Many researchers contributed to the evolution of the FDTD such as Mur [100] who published in 1981 the numerically stable, second-order accurate, absorbing boundary condition, Berenger [101] and many others researchers [102, 103, 104, 105].

Now we can say that the FDTD is the most used method to simulate the electromagnetic fields.

FDTD has been used to numerically solve the Maxwell's curl equations for various structures and in different, linear and nonlinear, media. Solving the optical response in a linear medium using the FDTD has attracted the interest of many researchers and many studies, discuss various types of structures and show a high accordance between FDTD results and experimental ones. However, various phenomena could take place while studying the optical response of a nonlinear medium, depending on the characteristics of medium and the existence of some external parameters that might affect the medium properties. When talking about nonlinear media the widely know effects are: the Kerr effect which is related to third order susceptibility of the medium, the second harmonic generation and the EO effect related to the second order susceptibility.

In 1992, Goorjian et al [106] presented a new algorithm that permits the direct time integration of Maxwell's equations in 2-D for material media having linear and nonlinear instantaneous and Lorentz-dispersive effects in the electric polarization. The nonlinear modeling takes into account such quantum effects as the Kerr and Raman interactions. Also in 1992, Zheng and Chen [107] published their work presenting an FDTD technique to simulate the transient signal propagating in a nonlinear, assumed to be Kerr-type, substrate. However, Tran [108] has developed an alternative FDTD scheme for Kerr nonlinearity when the electric field is obtained from the flux density via the solution of a cubic equation.

On the other hand, second harmonic generation has also attracted many researchers to simulate the effect using the FDTD method. In 2000, Xu et al [109] used the FDTD with the tight binding approximation to analyze coupled resonators waveguide and they investigated the SHG process in the coupled resonators. SHG is a known phenomena

that occurs in a non-centrosymetric materials, however, various studies and models have been proposed to investigate the SHG in a centrosymetric material due to the broken symmetry at the interface. Other studies have investigated the SHG in metallic structures. An algorithm for nonlinear FDTD was proposed by Barakat et al [45] to estimate the enhancement of the SHG in a metallo-dielectric structure. The authors proposed to calculate the optical response of the structure for each wavelength separately in order to bypass the convolution product that appears in the polarization equation.

## 2.2 Problematic

In our study we are interested in presenting a new FDTD algorithm able to estimate the optical response of a nonlinear medium. More specifically we are interested in studying the optical response coming from the EO effect (Pockels effect). Pockels effect can only occur in materials that are noncentro-symmetric as it is described by a second-order nonlinear susceptibility. EO effect is the linear variation of the refractive index of a material as a function of the strength of the applied electric field. Therefore, the Pockels effects as well as the all other linear and non-linear effects, appear in Maxwell's equations due to the polarization term. Thus, due to medium property, the light polarization may show linear and non-linear terms. The general equation of the light polarization is given as:

$$\vec{P} = \vec{P}_L + \vec{P}_{NL} = \varepsilon_0(\chi^{(1)}\vec{E} + \chi^{(2)}\vec{E}\vec{E} + \chi^{(3)}\vec{E}\vec{E}\vec{E} + ...) \tag{2.1}$$

Where $\chi^{(n)}$ is the nth order nonlinear susceptibility. $\chi^{(1)}E$ describes the linear response of the material. $\chi^{(2)}\vec{E}\vec{E}$ defines the SHG, sum and the difference frequency generation and the linear EO effect by changing the second E to be the static electric field

$\chi^{(2)}\vec{E}\vec{E}_0$; $\chi^{(3)}\vec{E}\vec{E}\vec{E}$ is both four-wave mixing and the third harmonic generation. In our work we are interested in studying the variation of the material refractive index as a function of the applied external electric field (the EO effect). Thus, we limit the study to the second order nonlinear susceptibility $\chi^{(2)}$. Consequently, the nonlinear polarization will be expressed as:

$$\vec{P}_{NL}(\omega) = \varepsilon_0 \chi^{(2)}(\omega)\vec{E}(\omega)\vec{E}_0 \tag{2.2}$$

where $\vec{E}_0$ denotes the applied external electric field.

Therefore, In our study we will be interested in studying the cases of structure fabricated by using the Lithium Niobate (LN) material. LN, which belongs to the calss of trigonal crystal symetry, is going to be used as the nonlinear material, it is one of the best known crystals used for various linear and non-linear optical applications [110]. Consequently, its refractive index variation with respect to the external applied electric field is linked to the EO tensor as following:

$$\begin{Bmatrix} \Delta(1/n^2)_1 \\ \Delta(1/n^2)_2 \\ \Delta(1/n^2)_3 \\ \Delta(1/n^2)_4 \\ \Delta(1/n^2)_5 \\ \Delta(1/n^2)_6 \end{Bmatrix} = \begin{Bmatrix} 0 & -r_{22} & r_{13} \\ 0 & r_{22} & r_{13} \\ 0 & 0 & r_{33} \\ 0 & -r_{51} & 0 \\ r_{51} & 0 & 0 \\ -r_{22} & 0 & 0 \end{Bmatrix} \begin{Bmatrix} E_{0x} \\ E_{0y} \\ E_{0z} \end{Bmatrix} \tag{2.3}$$

where $r_{ij}$ are the elements of the EO tensor and $E_0$ are the external applied electric field elements. Therefore, for LN, there is only four distinctive non zero elements of the

EO tensor and $r_{33}$ ($r_{33} = 33\ pm/V$) is the largest elements among them [111].

Assuming that the largest electric field components is measured with the $r_{33}$ whcih is along the z crystalline direction. By neglecting the other small EO elements contributions and according to the Pockels effect, the refractive index variation can be simplified [43] as:

$$\Delta n = -\frac{1}{2}.n^3.r_{33}.E_0 \tag{2.4}$$

Therefore the implementation of the classic Pockels effect is not complicated in the FDTD code. A linear FDTD study is conducted in order to verify the classical Pockels effect in a bulk LN, we have calculated the phase velocity of a monochromatic wavelength propagating in LN while applying different external electric fields. The results of this study are presented in chapter 4.

On the other hand, when a structure is presented in a bulk noncentro-symetric material and due to the optical electric field confinement that take place in the structure, the intrinsic non-linear optical property of the material are modified according to the degree of non-linearity. Thus, the second order susceptibility tensor $\chi^{(2)}$ becomes dependent on the field confinement inside the structure [51, 85] through the relation:

$$\chi^{(2)}_{mod} = \chi^{(2)}_{bulk} \times f^2 \tag{2.5}$$

where f is the field factor that was defined as [51, 85]: the ratio of the total electromagnetic field calculated inside the structure to the electromagnetic field calculated over the same region but in the absnece of the structure (in the bulk). f is given by the equation:

$$f(\omega) = \frac{E^{structure}(\omega)}{E^{bulk}(\omega)} \tag{2.6}$$

This definition is valid for both electromagnetic (EM) and Electrostatic fields and leads to an average value of the field factor. By introducing the modified $\chi^{(2)}$ in equation 2.2, the Pockels effect becomes non-linear due to the term $|E(\omega)|^2 \times E(\omega)$:

$$\vec{P}_{NL}(\omega) = \varepsilon_0 \chi^{(2)} f^2 \vec{E}(\omega)\vec{E}_0 \tag{2.7}$$

Nevertheless, as it will be discussed in chapter 5, different methods for the determination of the field factor (f) can be applied. In all of them, the field factor depends on the EM wave frequency and thus its temporal variations that is needed to be implemented in the FDTD algorithm, is obtained by finding the Fourier transform of equation 2.7 :

$$\vec{P}_{NL}(t) = \varepsilon_0 \int \int_0^{\infty} \int \bar{\bar{\chi}}_b^{(2)}(t_1, t_2, t_3) f_{op}(t-t_1) f_{op}(t-t_2) \vec{E}(t-t_3)\vec{E}_0 dt_1 dt_2 dt_3 \tag{2.8}$$

However, equation 2.8 presents a triple convolution product which is very hard to calculate numerically. Therefore, to bypass this difficulty in our FDTD code, different assumptions will be studied and some assumptions are applied to simplify the calculation.

In the coming parts of this chapter we will present both linear and non-linear algorithms of the FDTD method. In addition, due to the presence of dispersive materials in our structures, such as metals, a brief description of different methods to simulate this dispersion with respect to the frequency range will be given. As well, we will present the

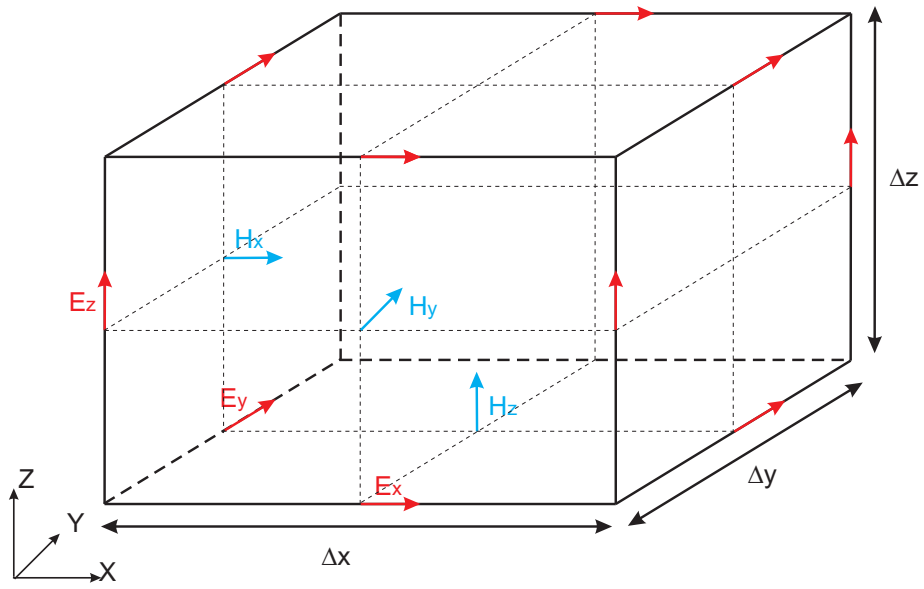


Figure 2.1: Elemental Yee cell, in which we represent the components of the electromagnetic field. Yee cell is defined by the spatial steps $\Delta x$, $\Delta y$ and $\Delta z$.

stability criteria for both algorithms and the concept of boundary conditions. We end this chapter by presenting the susceptibility tensor $\chi^{(2)}$ of nonlinear material, i.e., the LN.

## 2.3 FDTD principle

Yee algorithm [2] consists of discretizing Maxwell's equations in space and time domains. He decomposes the simulation window into cubic cells (see figure 2.1) and redefines the electric field equation and magnetic field equation by showing the spatial and temporal (see figure 2.2) relation between them by approximating the spatial and temporal derivatives by their central finite difference. For example the electric field at a time $(n+1)\Delta t$ is a function of the electric field at $(n)\Delta t$ and of the magnetic field at $(n+1/2)\Delta t$ see equation 2.14.

Maxwell's equations for the electric and magnetic fields are given by:

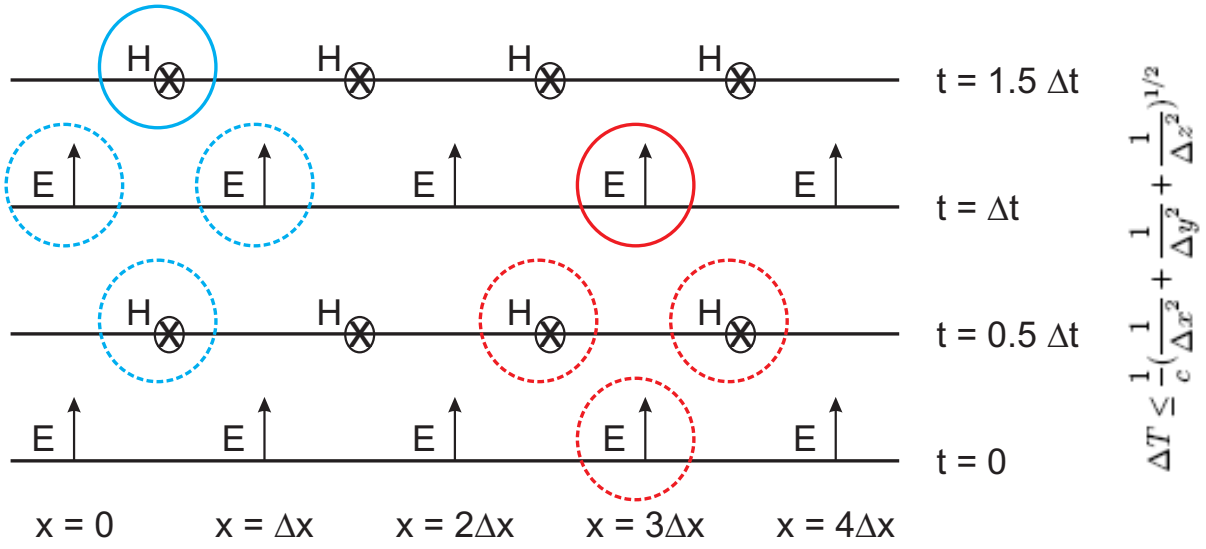


Figure 2.2: Space time chart of the Yee algorithm for a 1D wave propagation example showing the use of central differences for space derivatives and leapfrog for the time. Examples the three components with dashed circle are required to calculate the component with the same color with solid circle.

$$\frac{\partial \vec{B}}{\partial t} = -\nabla \times \vec{E} \tag{2.9}$$

$$\frac{\partial \vec{D}}{\partial t} = \nabla \times \vec{H} \tag{2.10}$$

Where, as usual, $\vec{E}$ is the electric field vector, $\vec{H}$ is the magnetic field vector, $\vec{D}$ is the displacement field vector and $\vec{B}$ denote the magnetic flux density vector. In practice, the number of fields is reduced to two by the constitutive relations,

$$\vec{D} = \varepsilon_0 \overleftrightarrow{\varepsilon_r}\, \vec{E} + \vec{P} \tag{2.11}$$

$$\vec{B} = \mu_0 \overleftrightarrow{\mu_r}\, \vec{H} \tag{2.12}$$

Where, $\mu_0$ and $\varepsilon_0$ are the magnetic permeability and dielectric permittivity of vacuum, respectively. The dimensionless quantities $\overleftrightarrow{\mu_r}$ and $\overleftrightarrow{\varepsilon_r}$ are the relative permeability and

permittivity tensors of the medium, respectively.

By developing Maxwell's equations to fit the approximation given by Yee's algorithm, in the case of linear, homogenous, isotropic and non-dispersive material, we get:

$$H_x^{n+1/2}(i,j,k) = H_x^{n-1/2}(i,j,k) + \frac{\Delta t}{\mu \Delta z}(E_y^n(i,j,k) - E_y^n(i,j,k-1)) - \frac{\Delta t}{\mu \Delta y}(E_z^n(i,j,k) - E_z^n(i,j-1,k)) \quad (2.13)$$

$$E_x^{n+1}(i,j,k) = E_x^n(i,j,k) + \frac{\Delta t}{\varepsilon \Delta y}(H_z^{n+1/2}(i,j+1,k) - H_z^{n+1/2}(i,j,k)) - \frac{\Delta t}{\varepsilon \Delta z}(H_y^{n+1/2}(i,j,k+1) - H_y^{n+1/2}(i,j,k)) \quad (2.14)$$

Expression 2.14 gives $E_x$ at time step $n+1$ in terms of previously values of $E_x$ at time step $n$, $H_y$ and $H_z$ at time step $n+1/2$. In a similar way, the finite difference expressions for $H_y^{n+1/2}(i,j,k)$, $H_z^{n+1/2}(i,j,k)$, $E_y^{n+1}(i,j,k)$ and $E_y^{n+1}(i,j,k)$ can be obtained see figure 2.2.

In the case of LN, the non-linear polarization term should be taken into account in the equation relating D to the electric field,

$$\vec{D}(\omega) = \varepsilon_0 \varepsilon_r \vec{E}(\omega) + \vec{P}(\omega) \quad (2.15)$$

Assuming an isotropic material ($\overleftrightarrow{\varepsilon_r} = \varepsilon_r$ and using equation 2.2 and 2.15 the electromagnetic field becomes:

$$H_x^{n+1/2}(i,j,k) = H_x^{n-1/2}(i,j,k) + \frac{\Delta t}{\mu(i,j,k)\Delta z}\left[E_y^n(i,j,k) - E_y^n(i,j,k-1)\right] - \frac{\Delta t}{\mu(i,j,k)\Delta y}\left[E_z^n(i,j,k) - E_z^n(i,j-1,k)\right] \quad (2.16)$$

$$H_y^{n+1/2}(i,j,k) = H_y^{n-1/2}(i,j,k) + \frac{\Delta t}{\mu(i,j,k)\Delta x}\left[(E_z^n(i,j,k) - E_z^n(i,j,k-1))\right] - \frac{\Delta t}{\mu(i,j,k)\Delta z}\left[(E_x^n(i,j,k) - E_x^n(i,j-1,k))\right\} \quad (2.17)$$

$$H_z^{n+1/2}(i,j,k) = H_z^{n-1/2}(i,j,k) + \frac{\Delta t}{\mu(i,j,k)\Delta y}\left[E_x^n(i,j,k) - E_x^n(i,j,k-1))\right] - \frac{\Delta t}{\mu(i,j,k)\Delta x}\left[E_y^n(i,j,k) - E_y^n(i,j-1,k)\right] \quad (2.18)$$

$$E_x^{n+1}(i,j,k) = E_x^n(i,j,k) + \frac{\Delta t}{\varepsilon(i,j,k)\Delta y}\left[H_z^{n+1/2}(i,j+1,k) - H_z^{n+1/2}(i,j,k)\right] - \frac{\Delta t}{\varepsilon(i,j,k)\Delta z}\left[H_y^{n+1/2}(i,j,k+1) - H_y^{n+1/2}(i,j,k)\right] - (P_x^{n+1}(i,j,k) - P_x^n(i,j,k)) \quad (2.19)$$

$$E_y^{n+1}(i,j,k) = E_y^n(i,j,k) + \frac{\Delta t}{\varepsilon(i,j,k)\Delta z}\left[H_x^{n+1/2}(i,j+1,k) - H_x^{n+1/2}(i,j,k)\right] - \frac{\Delta t}{\varepsilon(i,j,k)\Delta x}\left[H_z^{n+1/2}(i,j,k+1) - H_z^{n+1/2}(i,j,k)\right] - (P_y^{n+1}(i,j,k) - P_y^n(i,j,k)) \tag{2.20}$$

$$E_z^{n+1}(i,j,k) = E_z^n(i,j,k) + \frac{\Delta t}{\varepsilon(i,j,k)\Delta x}\left[H_y^{n+1/2}(i,j+1,k) - H_y^{n+1/2}(i,j,k)\right] - \frac{\Delta t}{\varepsilon(i,j,k)\Delta y}\left[H_x^{n+1/2}(i,j,k+1) - H_x^{n+1/2}(i,j,k)\right] - (P_z^{n+1}(i,j,k) - P_z^n(i,j,k)) \tag{2.21}$$

Expression 2.19 shows $E_x$ at time step $n+1$ in terms of previously values of $E_x$ and $P_x$ at time step $n$, in addition to $H_y$, $H_z$ at time step $n+1/2$ and $P_x$ at time step $n+1$. In a similar way, the finite difference expressions for $H_y^{n+1/2}(i,j,k)$, $H_z^{n+1/2}(i,j,k)$, $E_y^{n+1}(i,j,k)$ and $E_y^{n+1}(i,j,k)$ can be obtained.

## 2.4 FDTD stability criteria

Spatial and temporal meshing parameters should be well defined in the FDTD code in order to have accurate simulation results.

### 2.4.1 Spatial stability condition

The first parameter is the maximum cell dimension in the spatial step $\Delta x$ which should be short enough to well describe the desired structure. It should also be well defined to overcome any numerical dispersion coming from the transition between the analytical form of Maxwell's equations and the numerical approximation (central finit difference). A convergence numerical study shows that a spatial step of $\lambda_{min}/20$ of order of magnitude is needed to get a maximum error of $0.1$ on the phase velocity for an oblique wave propagating at $45^o$ from the grid axis [96]. $\lambda_{min}$ is defined as the smallest wavelength propagating in the grid so then:

$$\Delta x \leq \frac{\lambda_{min}}{20} \tag{2.22}$$

### 2.4.2 Temporal stability condition

In addition to the spatial step condition, a temporal step $\Delta T$ condition should be well considered. This criterion was given by Taflov and Brodwin in 1975 [3] to overcome the numerical instability. Once the spatial step is defined then the temporal step condition is given by the Courant-Friedrichs-Lewy [112] criterion:

$$\Delta t \leq \frac{1}{c}\left(\frac{1}{\Delta x^2} + \frac{1}{\Delta y^2} + \frac{1}{\Delta z^2}\right)^{1/2} \tag{2.23}$$

Where c represents the maximum velocity of the wave in a medium, generally taken to be the speed of light in vacuum. We have to note that while studying the linear response of a nano-structure we usually choose a time step close to the stability limit. Taking a shorter time step increases the simulation cost (time for each simulation) and didn't enhance the results accuracy. On the contrary, for a non-linear study we will see in chapter 4 that taking a smaller time step can bypass a diverging problem since $\Delta t$ is dependent on the

field factor temporal variation and not only on the spatial step.

## 2.5 Dispersion

The existence of metals in our plasmonic structures (nano-antenna) requires the integration of analytical models to well describe its electromagnetic dispersion properties:

$$\varepsilon = f(\omega) \tag{2.24}$$

Three main models of dispersion: Drude, Drude-lorentz and Drude critical point, are widely used depending on the metal nature and the wavelength range of interest.

### 2.5.1 Drude model

Drude model was proposed three years after the discovery of the electron by J. Thomson in 1897. In his theory, Drude considered the metal electrons as a gas of negative charged particles traversing a uniform positively charged medium [113] and then he suggestet applying the kinetic theory of gas to the electrons. However, Drude model is based on three main hypotheses:

- The interaction between electrons and other particles is only considered during the collision, otherwise the interaction is negligible.

- Collisions are considered to be instantaneous events that modify the velocity of an electron.

- An electron experiences a collision with a probability of 1/T; Where T is independent of the electrons position and is known as relaxation time, collision time, or mean free time. In Drude model, T is assumed to be independent of the electron position and is independent of time.

Based on these assumptions, the dielectric permittivity of metals according to the Drude model is given as:

$$\varepsilon_D(\omega) = 1 - \frac{\omega_p^2}{\omega(\omega + i\gamma_D)} \tag{2.25}$$

where $\gamma$ is the characteristic collision frequency of the free electron gas and $\omega_p^2 = ne^2/(\varepsilon_0 m)$ is the plasma frequency of the free electron gas, which depends on the density $n$ of the electrons in the metal and on the mass, $m$, of the electron.

The main advantage of the Drude model comes from its simplicity. In the case of silver and aluminum, adapting the values of $\omega_p$ and that of $\gamma$, the model is sufficient and allows us to correctly understand the physical phenomenon in the visible range. Whereas, in the case of gold, it is impossible to find a unique value for $\omega_p$ and for $\gamma$ to enable the use of this model over all the visible range. To overcome this issue, a Lorentzian part must be added to the Drude model.

### 2.5.2 Drude-Lorentz model

This model is an extended form of the Drude model by adding the Lorentzian term. It is based on the assumption that the movement between electrons and nucleus is harmonic. In addition by adding this part, the model becomes able to describe the permittivity of metals in a wider frequency band.

$$\varepsilon_r(\omega) = 1 - \frac{\omega_P^2}{\omega(\omega + i\gamma)} - \frac{\Delta\varepsilon.\Omega_l^2}{(\omega^2 - \Omega_l^2) + i\omega\Gamma_l} \tag{2.26}$$

$\Omega_l$ and $\Gamma_l$ represent, respectively, the pulsation free oscillation and the friction coefficient associated with the Lorentz terms. While $\Delta\varepsilon$ is a scalar factor between the two parts of the model.

### 2.5.3 Drude-critical points model

Describing the optical properties of some metals (e.g. Au) are more difficult to represent in the visible/near-UV region with the Drude or Drude-Lorentz model. The reason for that is the more important role played by inter-band transitions [114] in the violet/near-UV region (Au has at least two inter-band transitions). Describing this later with a Drude-Lorentz model [115] requires more Lorentzian terms and makes the model complicated with many unphysical parameters. For that, a combination of Drude and two Critical-Point (CP) model was proposed by Etchegoin et al [116]. Following this approach, the frequency-dependent optical properties of Au in the visible/near-UV range can be very well described by an analytic formula:

$$\varepsilon_{D2CP}(\omega) = \frac{\Omega_D^2}{\Omega^2 + i\omega\gamma_D} + \sum_{p=1}^{p=2} G_p(\omega) \tag{2.27}$$

$$G_p(\omega) = A_p\Omega_P\left(\frac{\varepsilon^{ip\phi}}{\Omega_P - \omega - ip\Gamma} + \frac{\varepsilon^{-ip\phi}}{\Omega_P + \omega + ip\Gamma}\right) \tag{2.28}$$

In equation 2.27 the symbols represent: $A_P$ amplitude; $\phi$ the phase; $\Omega_D$ energy

of the gap; and $\gamma_D$ broadening. Note that a comparative study between the Drude-Critical points and Drude-Lorentz model was achieved by Vial and Laroche [117] and they demonstrate that the Drude-critical points is more realistic to describe the dielectric function of Gold and Silver.

These three dispersion analytical models were integrated into the FDTD algorithm: Drude model by simply applying a Fourier transform of the constitutive equation [118, 119]. The Drude-Lorentz and Drude critical point models were adapted to the FDTD using a recursive convolution scheme [120, 117].

## 2.6 Boundary Conditions

As we have described in the previous sections, FDTD method consists of creating a simulation window in which we define the structure that we need to study. However the simulation window should be well defined and the method could not consider the case of an infinite window. In our work we will consider two kinds of boundary conditions depending on the structure that we are dealing with:

- In chapter 3, while looking into the optical response of a Bowtie nano-antenna BNA we will use a full 3D-FDTD code and thus the perfect matched layer (PML) will be applied on the six bounds of the simulation window in order to avoid any reflection on the window limits.

- In chapter 4, we will be looking into the refractive index variation of a multiple periodic structure. Therefore, a periodic 3D-FDTD code will be used and one periode of the structure is defined and due to the periodicity condition the simulation will infinitely reproduce the structure. In this code we will use two types of boundary

conditions: the PML on the top and at the bottom sides while the periodic boundary conditions (PBC) will be applied on the lateral bounds where the periodicity of the structure is applied.

### 2.6.1 Perfectly Matched Layer PML

Perfectly matched layer (PML) boundary condition was proposed by Berenger in 1994 [101]. PML technique relies on the principle of impedance matching at the interface between two media having the same refractive index. The PML is based on surrounding the simulation window by a perfect absorbant medium which has nonzero electric $\sigma^e$ and magnetic $\sigma^m$ conductivities (see figure 2.3). These two conductivities are in reality dependent on each other through the impedance matching condition:

$$\frac{\sigma^e}{\varepsilon} = \frac{\sigma^m}{\mu} \tag{2.29}$$

Unfortunately due to the high absorption in the PML, a parasitical reflection can be generated back into the structure. Those reflections come from the fact that the spatial discretization is not adapted to the variation of the electric field. To bypass this problem, the conductivity is considered to increase as we go further in the PML (polynomial behavior).

Therefore using the PML techniques, all propagating light outgoing from the simulation window is absorbed by the PML and consequently there is no reflected light to the interior ($10^{-6}$ to $10^{-7}$ reflection coefficient). We have to note that the PML is not able to absorb the evanescent wave. Thus, it is necessary to leave enough space between the structure and the PML region. A distance equal to $\lambda_{max}/2$ is fairly enough to eliminate

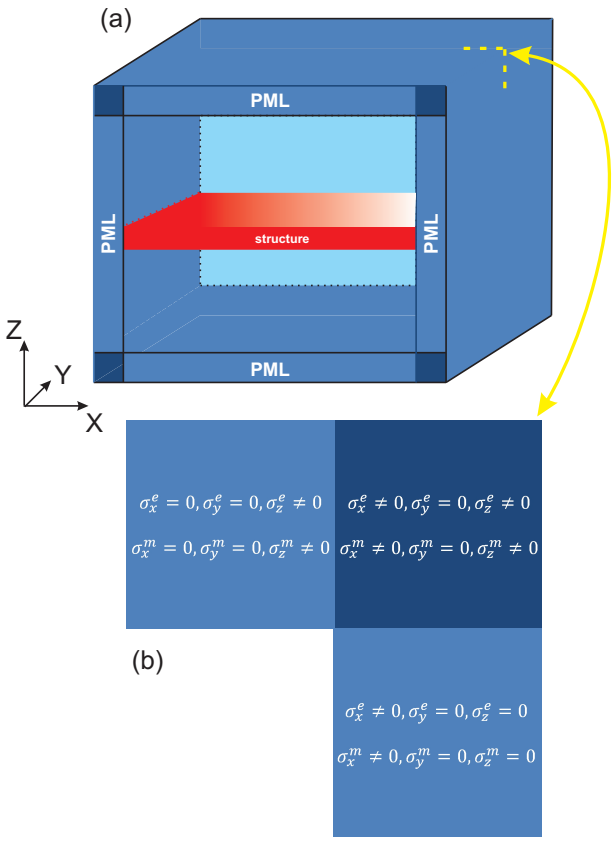


Figure 2.3: Scheme representing the simulation window of a full 3D-FDTD code, (a) show the PML at different sides of the simulation window as well as on the sides intersection zone (blue zone), (b) shows the needed conductivities of three different zones (circled area on figure (a)).

any effect due to the reflection of the evanescent wave, where $\lambda_{max}$ is the maximum value of the wavelength range in which we are interested.

### 2.6.2 Periodic Boundary Conditions (PBC)

For a periodic structure (e.g. photonic crystal), using a periodic 3D-FDTD code with the periodic boundary conditions [121, 122] consumes time required by the simulations. In addition it makes the simulation similar to an infinite structure case. The periodic boundary conditions are applied along the periodicity directions while PML is still considered in the other directions (non-periodic) (see figure 2.4). PBC is obtained through the Floquet-Bloch theorem which considers that the electromagnetic fields $\vec{E}$ and $\vec{B}$ at the boundary cell are the same as the electromagnetic fields at the first cell with a phase term difference $(e^{ik_x.p})$ .

$$\vec{E}(x = p_x, y, t) = \vec{E}(x = 0, y, t)e^{ik_x.p_x} \tag{2.30a}$$

$$\vec{E}(x, y = p_y, t) = \vec{E}(x, y = 0, t)e^{ik_y.p_y} \tag{2.30b}$$

$$\vec{H}(x = p_x, y, t) = \vec{H}(x = 0, y, t)e^{ik_x.p_x} \tag{2.30c}$$

$$\vec{H}(x, y = p_y, t) = \vec{H}(x, y = 0, t)e^{ik_y.p_y} \tag{2.30d}$$

We note that when using the periodic 3D-FDTD code, we only deal with the normal incidence. In the case of the normal incidence the phase shift term becomes equal to zero and thus it is easy to be integrated in the FDTD algorithm. Otherwise, in the case of an incident angle different from zero the phase shift term becomes frequency-dependent and it will be difficult to implement in the FDTD code [123].

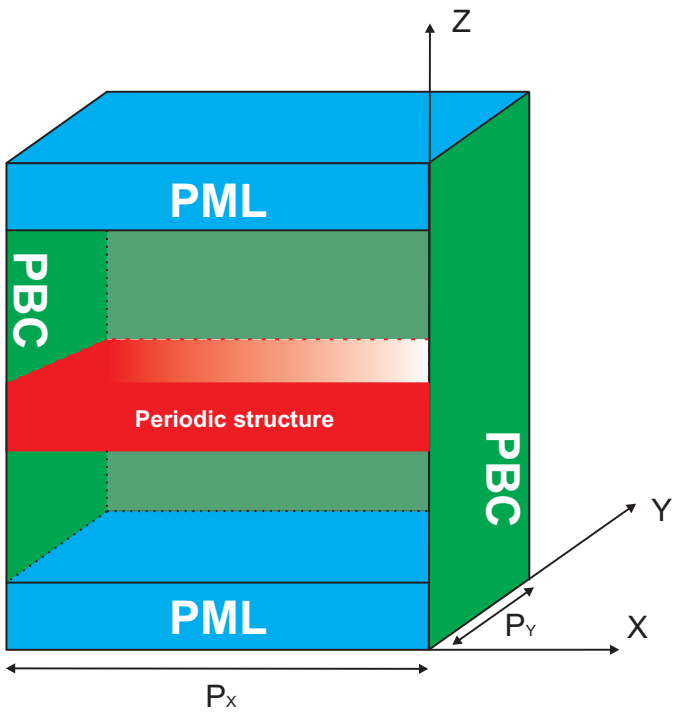


Figure 2.4: Scheme representing the simulation window of a periodic 3D-FDTD code. We see the PML at the top and bottom sides of the simulation window while the PBC is applied on the sides.

## 2.7 Second order susceptibility tensor of LN

Pockels effects, as we have seen in the previous part (see 2.2), is related to the second order susceptibility tensor. However, this tensor is a physical characteristic of the material in use, in other words, to its point group. Second order susceptibility tensor $\chi^{(2)}$, is a third rank tensor with 27 components $\chi^{(2)}_{ijk}$ in Cartesian coordinate system. Since the dielectric permeability tensor is real and symmetric, then the EO tensor must also be symmetric in its last two indices $\chi^{(2)}_{ijk} = \chi^{(2)}_{ikj}$. The third rank tensor can be represented through a contracted tensor $\chi_{ij}$, a two dimensional matrix with 18 different elements $r_{ih}$ out of

the initial 27 elements.

$$h = \begin{cases} 1, & \text{if } jk = 11 \\ 2, & \text{if } jk = 22 \\ 3, & \text{if } jk = 33 \\ 4, & \text{if } jk = 23, 32 \\ 5, & \text{if } jk = 13, 31 \\ 6, & \text{if } jk = 12, 21 \end{cases} \tag{2.31}$$

Using this EO tensor matrix, EO polarization of equation 2.2 will be given as:

$$\begin{Bmatrix} P_x \\ P_y \\ P_z \end{Bmatrix} = 2\varepsilon_0 \begin{Bmatrix} r_{11} & r_{12} & r_{13} & r_{14} & r_{15} & r_{16} \\ r_{21} & r_{22} & r_{23} & r_{24} & r_{25} & r_{26} \\ r_{31} & r_{32} & r_{33} & r_{34} & r_{35} & r_{36} \end{Bmatrix} \begin{Bmatrix} E_x E_{0x} \\ E_y E_{0y} \\ E_z E_{0z} \\ E_y E_{0z} + E_z E_{0y} \\ E_x E_{0z} + E_z E_{0x} \\ E_y E_{0x} + E_x E_{0y} \end{Bmatrix} \tag{2.32}$$

In our case, we are interested in the EO effect of a LN photonic crystal. However, LN has the point symmetry group 3m and thereby the second order susceptibility has an anisotropic behavior. Nonzero components of the EO coefficients of crystals of LN are $r_{22} = r_{21} = r_{16} = 3\ pm/V$, $r_{31} = r_{32} = r_{15} = r_{24} = 5\ pm/V$ and $r_{33} = 33\ pm/V$. Therefore, the EO polarization corresponding to the crystal in use is given as:

$$\begin{Bmatrix} P_x \\ P_y \\ P_z \end{Bmatrix} = 2\varepsilon_0 \begin{Bmatrix} 0 & 0 & 0 & 0 & r_{31} & -r_{22} \\ -r_{22} & r_{22} & 0 & r_{31} & 0 & 0 \\ r_{31} & r_{31} & r_{33} & 0 & 0 & 0 \end{Bmatrix} \begin{Bmatrix} E_x E_{0x} \\ E_y E_{0y} \\ E_z E_{0z} \\ E_y E_{0z} + E_z E_{0y} \\ E_x E_{0z} + E_z E_{0x} \\ E_y E_{0x} + E_x E_{0y} \end{Bmatrix} \tag{2.33}$$

From the equation 2.33 and the nonzero coefficients we can see that an electric field component along the optical axis (Z axis) is needed to exploit the biggest EO coefficient $r_{33}$. Therefore, the equation 2.33 leads to the three components of the EO polarization vector:

$$P_x = 2\varepsilon_0(r_{31}(E_x E_{0z} + E_z E_{0x}) + r_{22}(E_y E_{0x} + E_x E_{0y})) \tag{2.34a}$$

$$P_y = 2\varepsilon_0(-r_{22} E_x E_{0x} + r_{22} E_y E_{0y} + r_{31}(E_y E_{0z} + E_z E_{0y})) \tag{2.34b}$$

$$P_z = 2\varepsilon_0(r_{31} E_x E_{0x} + r_{31} E_y E_{0y} + r_{33} E_z E_{0z}) \tag{2.34c}$$

We can conclude that when the static electric field and the optical electric field, are parallel to the crystal axis of LN, the EO polarization term becomes more efficient.

By the way, the other 2 components $r_{22}$ and $r_{31}$ can be neglected in comparison with $r_{33}$ and thus Pz reduces to:

$$P_z = 2\varepsilon_0 r_{33} E_z E_{0z} \tag{2.35}$$

As expected, the EO polarization is proportional to the electric field meaning that it is a linear effect. Its implementation in the FDTD algorithm is very easy through the direct integration of the P expression into the constitutive relation. Consequently, the $E_z$ equation given by equation 2.21 becomes:

$$\begin{aligned} E_z^{n+1}(i,j,k) = E_z^n(i,j,k) &+ \frac{\Delta t}{\varepsilon \Delta x}\left[H_y^{n+1/2}(i,j+1,k) - H_y^{n+1/2}(i,j,k)\right] \\ &- \frac{\Delta t}{\varepsilon \Delta y}\left[H_x^{n+1/2}(i,j,k+1) - H_x^{n+1/2}(i,j,k)\right] \\ &- 2\varepsilon_0 r_{33} E_{0z}\left[E_z^n(i,j,k) - E_z^{n-1}(i,j,k)\right] \end{aligned} \tag{2.36}$$

In this chapter we have presented the numerical concept of FDTD in addition to the theory for solving Maxwell's equations by using the Yee algorithm [2]. The Maxwell's equations were presented in two ways to be able to consider both linear and EO effects of different structures. Different methods to describe the metal dispersion were presented as well, henceforth the simple Drude model will be used. In addition, we have presented the FDTD criteria and the boundary conditions. Theoretical results for linear and EO effects will be shown in chapters 3 and 4, respectively.

# Chapter 3

# Resonance sensitivity of a fibered Bowtie Nano-Aperture

## 3.1 Introduction

In this chapter we are interested in studying the optical sensitivity of the Bowtie Nano-Aperture BNA to the distance $D$ separating it from a given substrate [124]. The study shows the sensitivity of the Bowtie nano-aperture to the distance $D$, and consequently introduce the Bowtie nano-aperture as a promising tool for tip to sample control alternative to mechanical system used nowadays. We start by presenting a full numerical study achieved using a home made 3D-FDTD code, followed by an experimental study in order to verify the theoretical results. In the theoretical study, we consider the collection mode (CM) of the BNA executed by illuminating the tip with a plane wave from the substrate part and the emission mode (EM) by injecting light from the fiber side. Theoretical study will discuss the optical response of the BNA to the distance separating it from a high (Indium Phosphide InP) and low (Glass) refractive index substrate. Although we

limit the experimental study [23] to the collection mode and only consider the case of high refractive index substrate.

## 3.2 Theoretical study

### 3.2.1 Structure description

As we have mentioned above, in our work we are interested in studying the resonance properties of a BNA engraved at the apex of a fiber metal coated tip [125]. The latter has a conical shape (polymer of optical index $n = 1.52$) ended by a semi-spherical apex of radius $R = 500\ nm$ and coated with $105\ nm$ aluminum layer. The BNA has lateral size $L = 215\ nm$, gap dimension $G = 45\ nm$, bow angle $\theta = 45^o$ and has the same thickness as the aluminum layer see figure 3.1. Using the linear 3D-FDTD code described in chapter 2 we study the optical response of the BNA when it's placed at a distance $D$ from a substrate with refractive index $n = 3.17$ in the case of InP and $n = 1.5$ in the case of Glass. The computational window is surrounded by perfectly matched absorbing layer boundaries (PML) [101] in all three directions. As well, a linear Drude dispersion model is applied in the aim of modeling the metal dispersion($\varepsilon = f(\omega)$). A non-uniform meshing is applied in our calculation to accurately describe the BNAT where the smallest spatial step is $\delta x = \delta y = \delta z = 5\ nm$ in the region around the BNA and a largest step $\Delta x = \Delta y = \Delta z = 15\ nm$ for the remaining part of the window. The overall calculation window is a parallelepiped with $3.165 \times 3.165 \times 3.665\ \mu m^3$. These geometrical parameters were chosen so that the BNA resonance wavelength remains, when $D$ varies, in the spectral range of a usual continuum laser source.

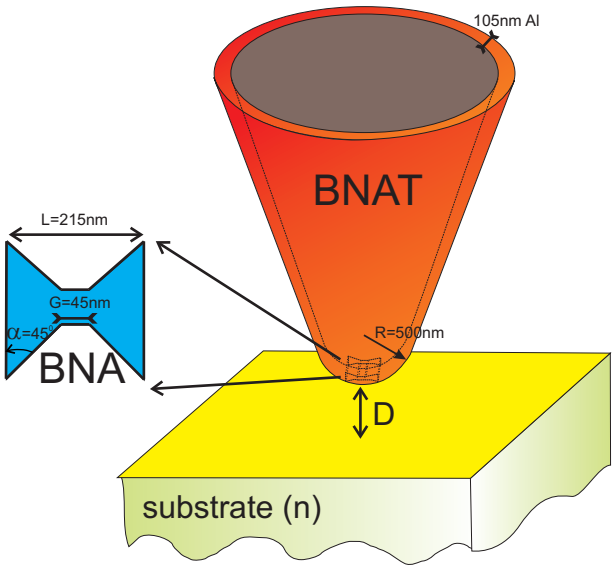


Figure 3.1: Bowtie shaped antenna (width $L = 215\ nm$, gap dimension $G = 45\ nm$) engraved at the end face of a fiber tip coated with $105\ nm$ aluminum layer, and placed at a distance $D$ from the substrate.

### 3.2.2 Antenna in vacuum

Firstly, we started our work by conducting a study, in which we discuss the resonance of the BNAT in vacuum (simulation window filled by a medium with refractive index $n = 1$ and without the presence of a substrate). In figure 3.2 we present the results corresponding to the antenna operating in collection mode. Figure 3.2(a) shows the near-field normalized spectrum recorded at the gap center of the BNA with a maximum denoting the resonance excitation at $\lambda = 1118.5\ nm$. The latter corresponds to the cut-off wavelength of the fundamental mode of the infinitely-long waveguide having a bowtie-shape section [1]. Normalization in that case is the division of intensity collected at the BNA gap center divided by the intensity collected at the same point without the presence of the BNA. We note that for the BNA operating in the emission mode the same resonance spectrum is obtained.

Light polarization is a key parameter affecting the resonance of the BNA which could be ON or OFF depending on the light polarization direction. When the electric field is

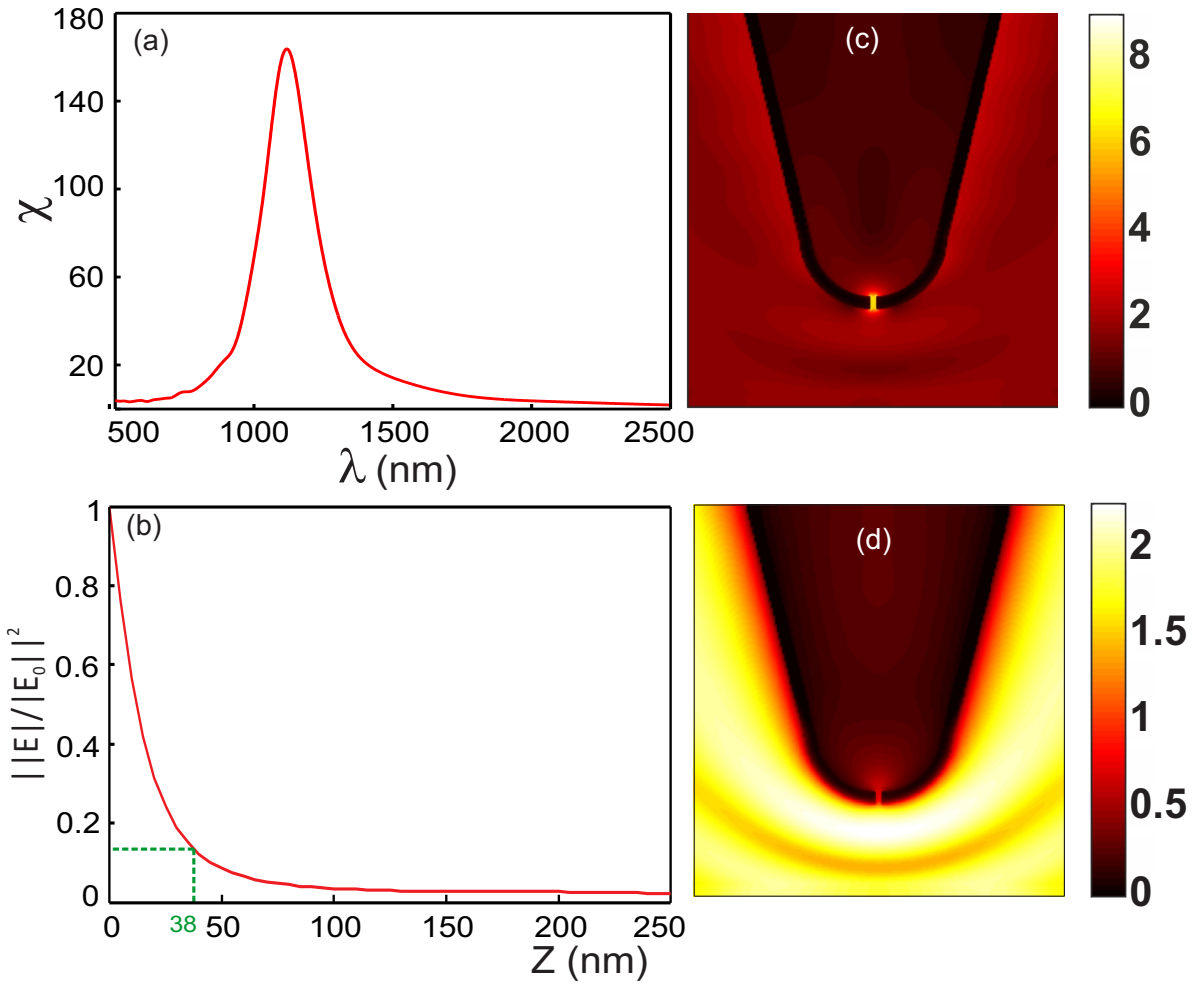


Figure 3.2: Optical response of BNA operating in vacuum and operating in collection mode (a)Near-field spectrum detected at the gap center,(c) and(d) present the distribution of the forth root of the electric field amplitude in the YZ plane through the center of the gap when the BNA is ON and OFF resonance respectively (b) Variations of the intensity in front of the tip along its axis (BNA ON resonance), $d = 38\ nm$ corresponds to the decay-length.

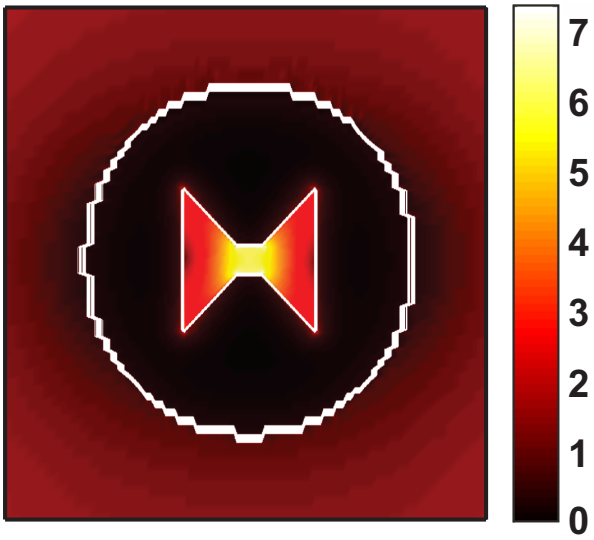


Figure 3.3: Electric field distribution in XY plan taken at the middle of the BNA .

directed toward the metallic arms of the BNA the antenna is on resonance see figure 3.2(b). whereas the antenna is off resonance when the illumination is turned by $90^o$ (see figure 3.2(d)). As we can clearly see by a comparison of both figures, the light enhancement is negligible when the BNA is off resonance. The case of resonant BNA will be considered in all coming results. As well, figure 3.2(b) demonstrates that the high confinement of the electric field takes place in the BNA gap and not in all the opened area (see figure 3.3). In fact, at the cutoff wavelength, the group velocity of the guided mode tends to zero while the associated phase velocity tends to infinity. Consequently, this slow light mode is at the origin of the electric field enhancement in the gap zone [1].

A cross-section of the intensity map (figure 3.2(b)) made along the tip axis is presented in figure 3.2(c). From this figure we can estimate the distance limit. This latter corresponds to the maximum distance between the tip apex and an object for which the resonance properties of the BNA is not affected. In fact, this distance $d$ can be estimated as the one for which the intensity of the electric field decreases by a factor of $1/e^2$. For both emission and collection modes the calculations demonstrate that $d = 38nm$.
Let us mention that in the following, the resonance wavelength (RW) of the BNAT can be

determined differently according to the calculated signal: near-field signal in the gap zone (detector at a single grid cell) or collected energy inside the fiber (energy flux through a section of the fiber). Thus, we have defined two different RW, namely a near-field RW ($RW^{NF}$) and a far-field one ($RW^{FF}$). A relation between the far and near field resonance wavelengths in the case of simple geometries could be determined due to the formula given in [126]. As well, we have defined the normalized near field $\chi^{NF}$ and far field $\chi^{FF}$ enhancement factor results. Near field enhancement factor $\chi^{NF}$ results are defined as the energy calculated at BNA gap center divided by the energy calculated at the same point without the BNAT. While the far field enhancement factor $\chi^{FF}$ are defined as the Poynting vector flux through an internal transverse section of the tip calculated far from its apex in order to eliminate possible surface plasmon waves propagating at the inner and/or the outer metallic walls of the tip. In fact, even if these waves are excited by the BNA, they cannot significantly contribute to the collected far-field power due to their absorption by the metal during their propagation. A small diffused part of light can affect the detected signal when the plasmon waves encounter small protrusions (metallic or dielectric surface irregularities) during propagation.

### 3.2.3 Collection mode

In figure 3.4 we present the near field resonance spectra of the BNA for different tip-to-substrate distances. Figures 3.4 (a) and (b) represent the case of a BNAT placed in front of an InP substrate and glass substrate, respectively. Note that, the results shown in both figures represent the normalized enhancement factor. By comparing the results shown in figures 3.4 (a) and (b) we can clearly notice that the influence of the substrate is much more important when the BNA is close to the substrate. We should mention that in the case of the InP substrate the RW presents a shift of $\Delta\lambda = 316\ nm$ while

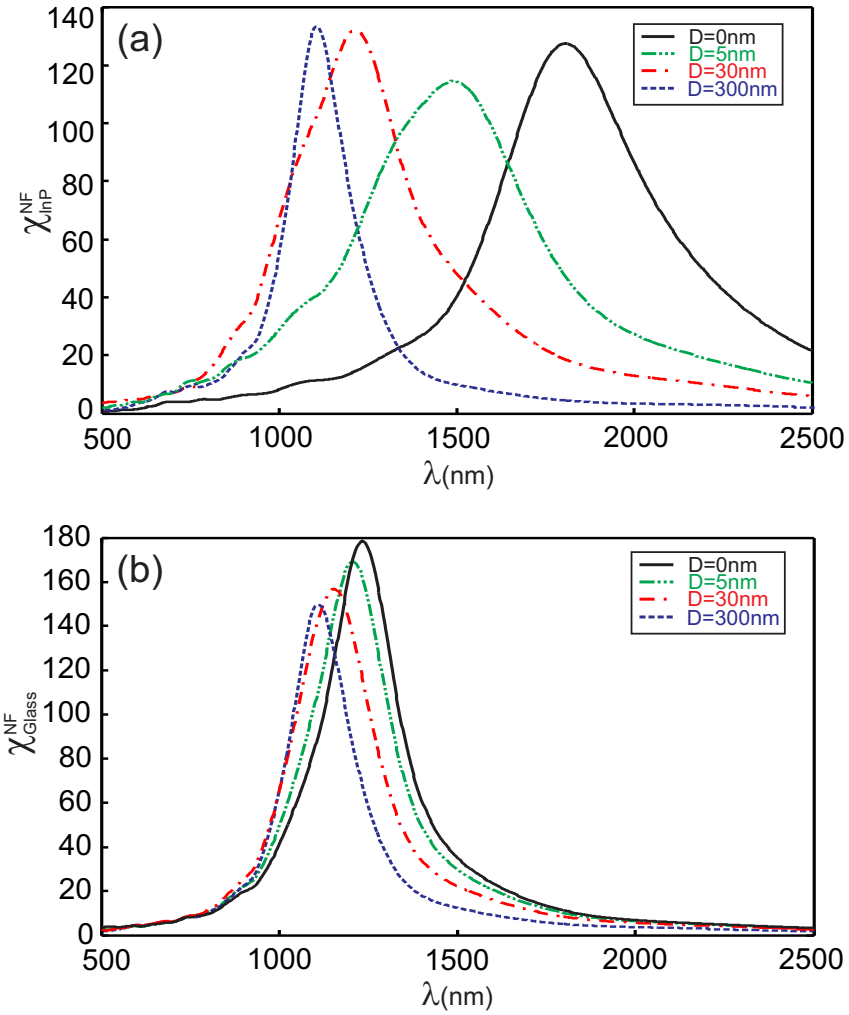


Figure 3.4: Resonance spectra of the BNA versus the distance separating it from: (a) an InP substrate, (b) a glass substrate.

it's only $\Delta\lambda = 26\ nm$ in the case of the glass substrate for a distance variation from $D = 0\ nm$ to $D = 5\ nm$, denoting the high sensitivity of the BNA to the substrate optical index.

#### 3.2.3.1 Resonance Wavelength variation

To well understand the resonance sensitivity of the BNA against the substrate we have started by studying the resonance wavelength variation as a function of the distance $D$ when this latter varies from $0\ nm$ to $300\ nm$.

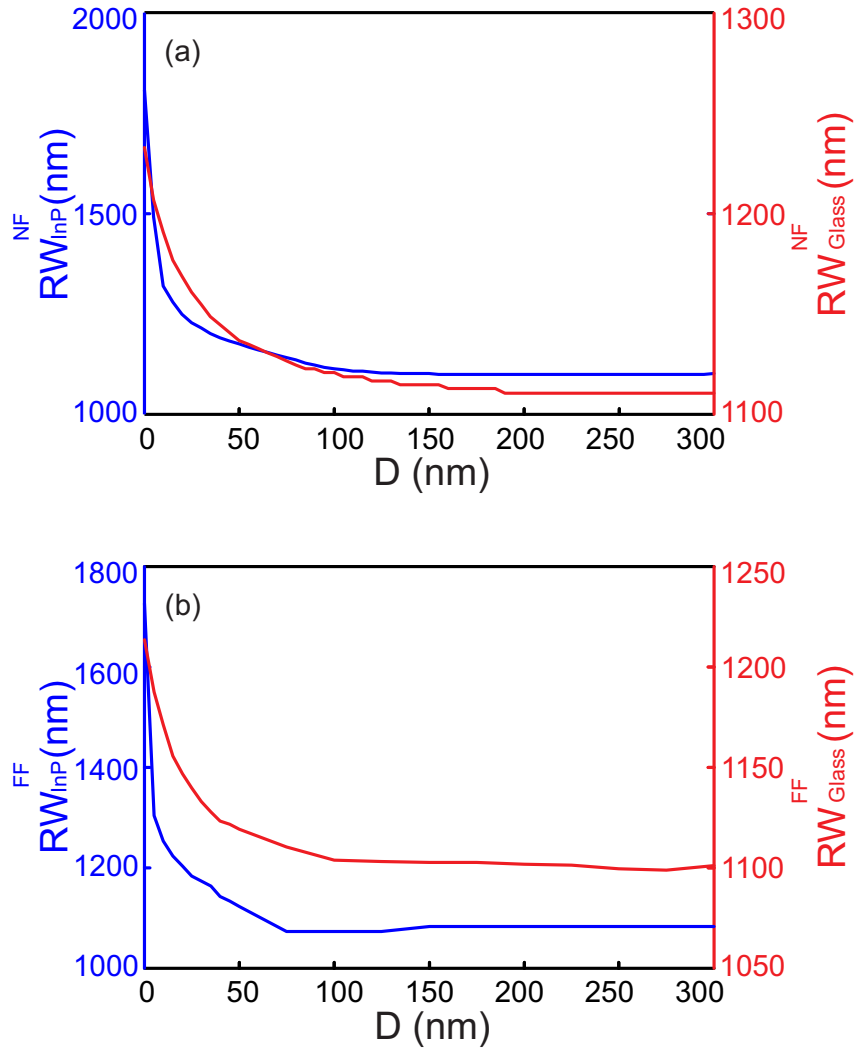


Figure 3.5: Resonance wavelength variation as a function of the distance, (a) results collected in Near-Field, (b) results collected in Far-Field.

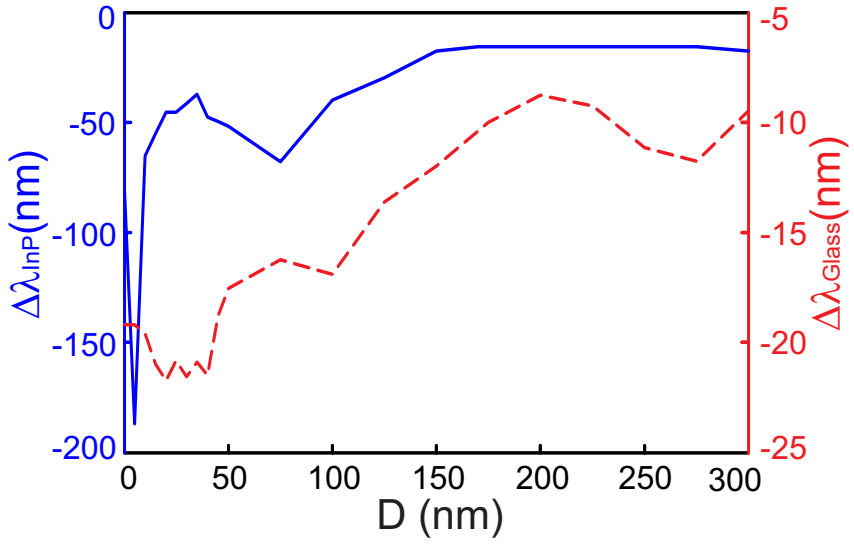


Figure 3.6: Difference between Near-field and Far-Field resonance wavelength.

Figures 3.5(a) and (b) represent the resonance wavelength variations as a function of the distance in near field and far field, respectively. In both figures, the blue solid line corresponds to the $RW$ variation when the BNA is placed in front of a high index substrate (InP) while the red solid line corresponds to the case of a glass substrate. We notice that the $RW$ variation proves a prompt decline with respect to $D$. As we have concluded earlier from figure 3.4, $RW$ presents a much important blue shift in the case of a high optical index substrate (i.e. InP). In fact, when the BNA is placed in front of an InP substrate the near field $RW$ goes from $\lambda = 1808\ nm$ for $D = 0\ nm$ to $\lambda = 1319\ nm$ for $D = 10\ nm$ while for a similar distance variation of BNA in front of a glass substrate the $RW$ varies from $\lambda = 1233\ nm$ to $\lambda = 1190\ nm$. $RW$ shows the same variation for both $NF$ and $FF$ results, the variation is remarkable between $D = 0\ nm$ and $D = 100\ nm$, while for higher distance, $\lambda$ tends to reach the $RW$ of the BNA when operating in vacuum. However, a significant blue-shift, between the resonance wavelength obtained in far field and near field resonance wavelength (see figure 3.6), occurs due to the Rayleigh scattering effect (power in $1/\lambda^4$). In fact, the BNA acts as a dipole that diffuses light inside the fiber. Its near-field spectrum density is then different from the diffused far-field power because the diffused energy depends on the

frequency.

#### 3.2.3.2 Enhancement factor variation

As discussed earlier, the BNA exhibits two optical properties: the resonance wavelength and the enhancement factor. The $RW$ was studied in the previous section, and in the same manner a study concerning the enhancement factor variation as a function of distance $D$ will be conducted in this section. Figures 3.7 (a) and (b) show the enhancement factor as a function of the distance $D$ in near field ($\chi^{NF}$) and far field ($\chi^{FF}$), respectively. We notice that, in both near field and far field, the enhancement factor variation in the case of InP substrate shows a more remarkable oscillation than the one detected in the case of the glass substrate. In fact this oscillation denotes the efficiency of the interference waves propagating back and forth between the tip and the substrate.

Enhancement factor variation presented in figure 3.7 corresponds to the enhancement factor at the resonance wavelength which in its turn depends on the distance variation. Figure 3.8 gives us a better understanding of the variation of the enhancement factor being a function of the distance by choosing three different operating wavelengths. We can clearly see that, depending on each wavelength and for the same BNA, the variation of $\chi$ presents different behaviors: decreasing (black line corresponds to $\lambda = 1100\ nm$), increasing (red line corresponds to $\lambda = 1700\ nm$) and presenting a maxima at a given distance (blue line corresponds to $\lambda = 1500\ nm$). Consequently, we can design the BNA to operate in a way that the collected power by the fiber shows a maximum at a desired distance which may correspond for example to the feedback set point of the shear force signal usually used in SNOM experience. By the way, these results open the way towards an alternative nano-positioning technique and toward a BNA designed for nano-sensing application.

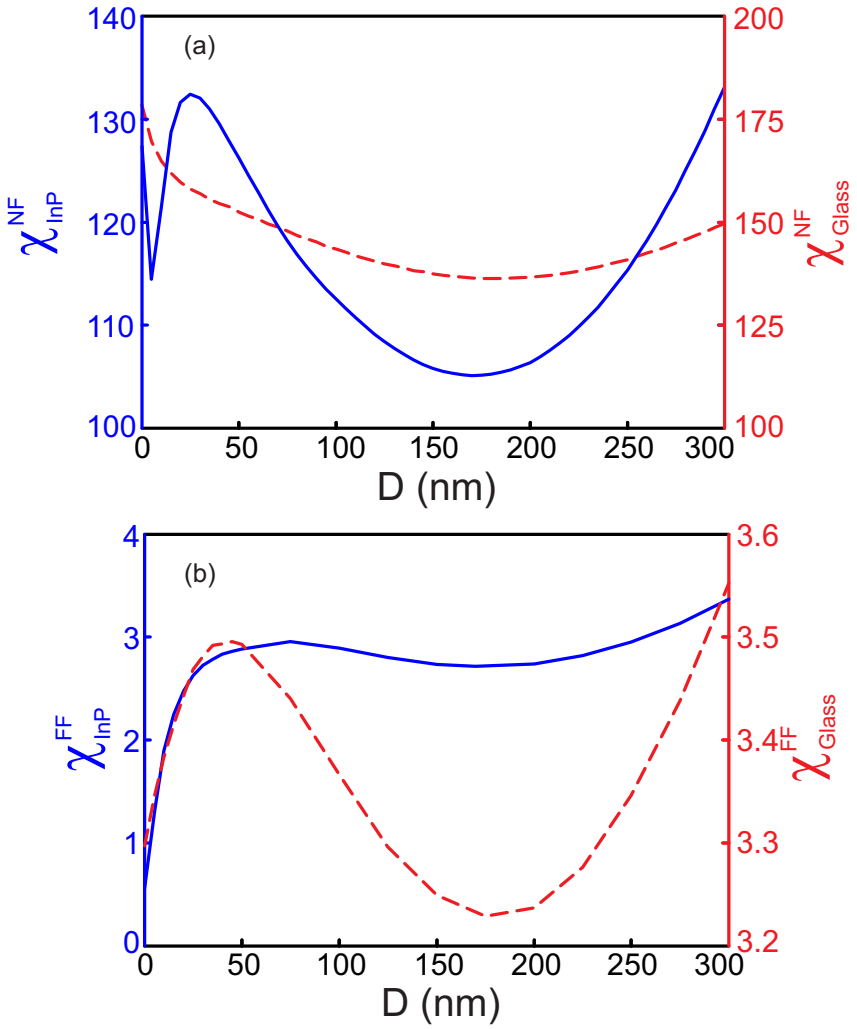


Figure 3.7: Enhancement factor variation as a function of the distance. (a) Results collected in Near-Field (b) Results collected in Far-Field.

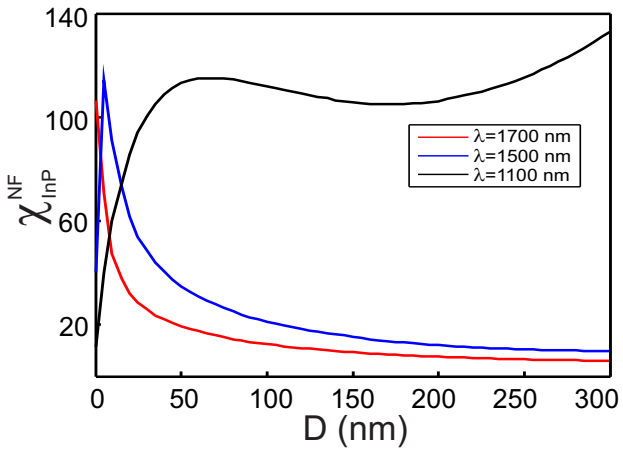


Figure 3.8: Enhancement factor for three wavelength black line corresponds to $\lambda = 1100\ nm$, blue line for $\lambda = 1500\ nm$ and red line for $\lambda = 1700\ nm$.

#### 3.2.3.3 Optical index sensitivity

As we have demonstrated earlier in this chapter the sensitivity of the BNA, either in terms of resonance wavelength or enhancement factor, is dependent on the optical index of the substrate. In addition, we concluded that the BNA presents a higher sensitivity in front of a high optical index substrate.

To well understand the influence of the substrate on the BNA optical properties, a study showing the response of the BNA facing a substrate with optical index going from $n = 1$ (vacuum medium) to $n = 3.5$ was conducted. Results shown in figure 3.9 represent the ones collected in far field. In fact, based on the results found in the previous sections, the far field and the near field outcomes, do not show a significant difference except the blue shift in term of resonance wavelength due to the Rayleigh scattering effect. In figure 3.9(a) we present the $RW$ variation, while in figure 3.9(b) we present the enhancement factor variation as a function of the optical index $n$. We clearly notice

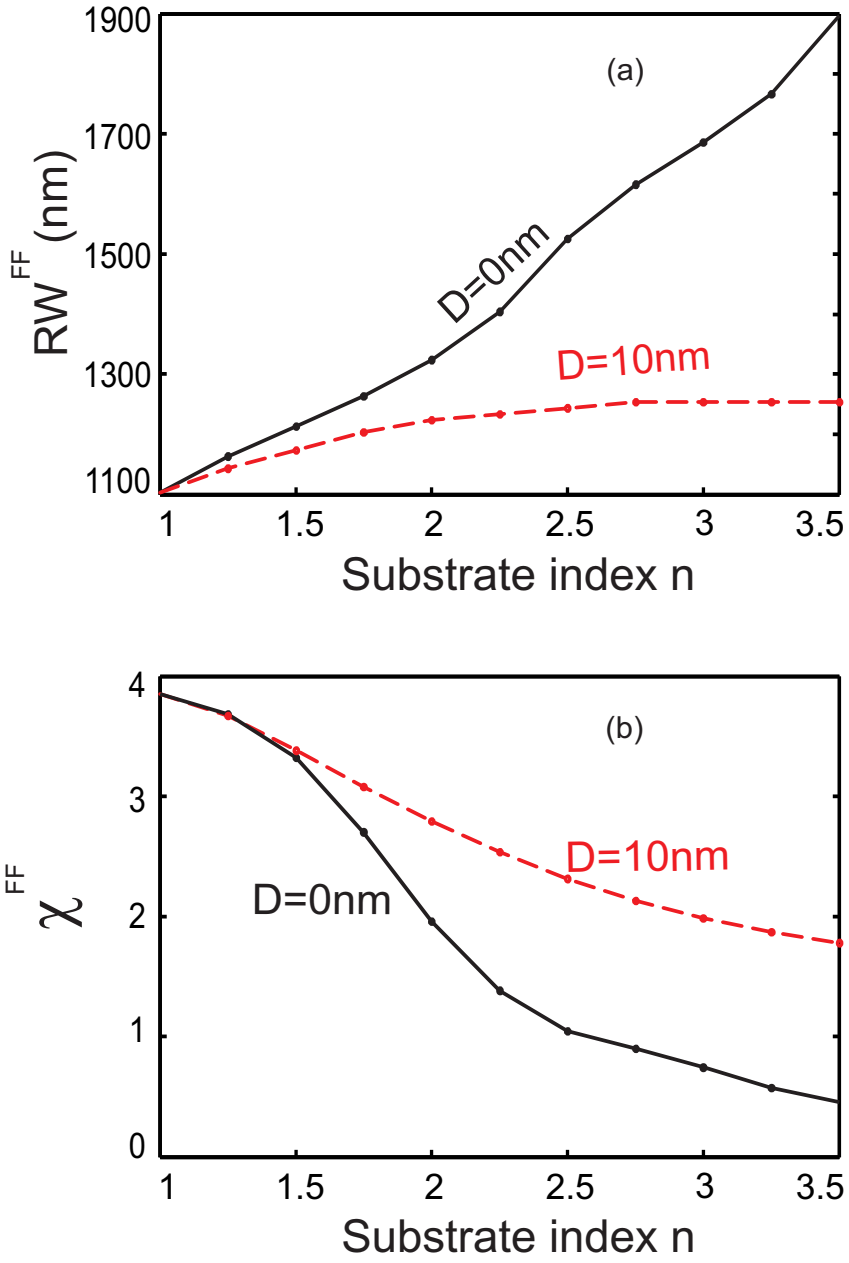


Figure 3.9: (a),(b) Show respectively the variation in far field, of the resonance wavelength and the enhancement factor, as a function of the substrate optical index for $D = 0\ nm$ (black curve) and $D = 10\ nm$ (red curve).

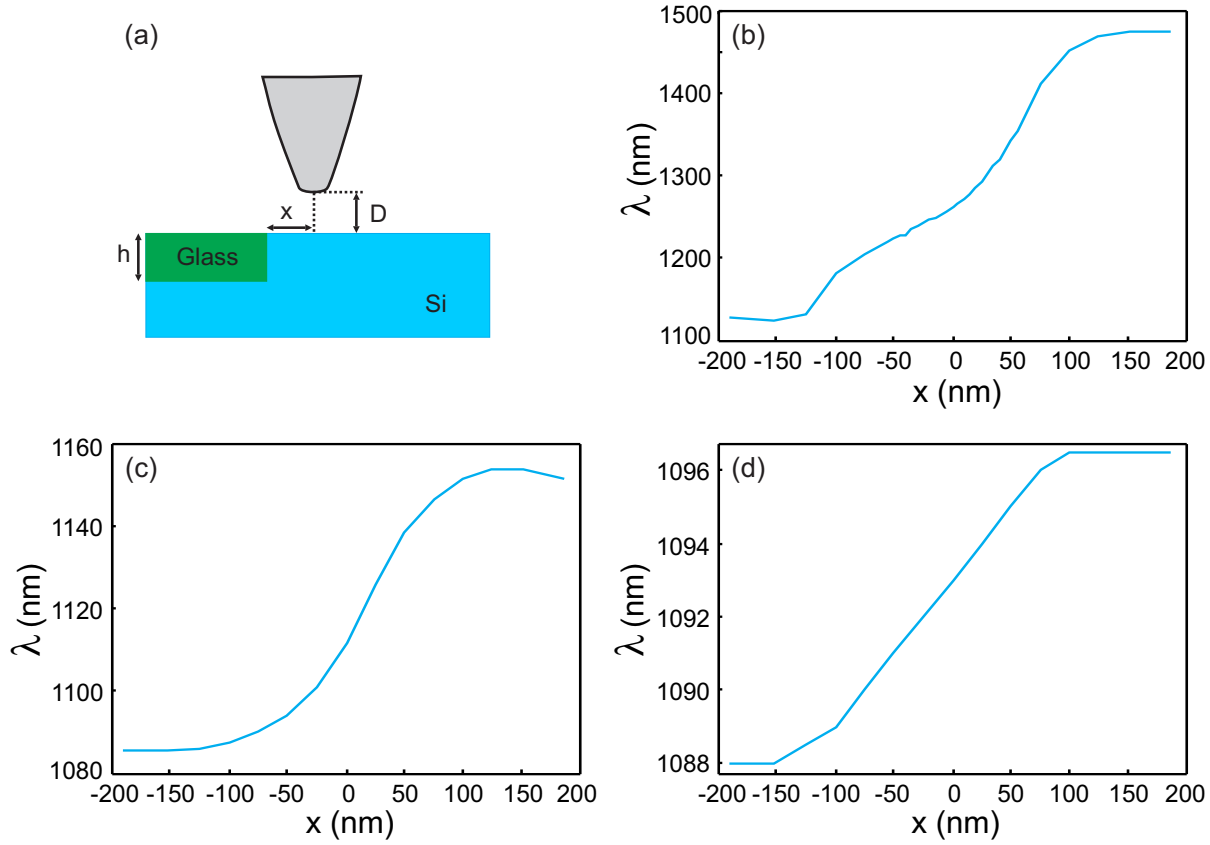


Figure 3.10: Resonance wavelength variations as a function of the distance ($x$) between the BNA center and an index step (glass-Si with $h = 100\ nm$) for three different values of $D$, (a) schematic of the supposed configuration. results for BNA at $5\ nm$, $50\ nm$ and $150\ nm$ in (b), (c) and (d) respectively.

that the optical index of the substrate is a critical parameter which highly influences the optical properties of the antenna. Consequently, the BNA should be optimized depending on the desired application.

longitudinal sensitivity of the Bowtie nano-aperture has been demonstrated and the antenna response is highly related to the distance separating it from the substrate. However, to well understand the sensitivity of the antenna a study was completed in order to estimate the lateral sensitivity of the Bowtie nano-aperture. Calculated results show that the antenna displays sub-wavelength lateral sensitivity as shown in figure 3.10. In this figure we consider the case of a BNA facing a silicon (Si) substrate in which we integrate a small piece of glass (depth $h = 100\ nm$), thus the BNA will be considered as facing a

substrate with an index step (see figure 3.10(a)). In our simulations we have considered three different distances separating the BNA from the substrate $D = 5\ nm$ 3.10(b), $D = 50\ nm$ 3.10(c) and $D = 150\ nm$ 3.10(d). The BNA is then moved laterally to figure out the optical response variation of the BNA with respect to the distance $x$ from the Glass step. The sensitivity of the BNA is higher for small distances as expected. In fact, when the BNA is close to the substrate, the variation of the medium effective optical index as a function of $x$ will be more important which induces a higher optical sensitivity.

### 3.2.4 Emission mode

After studying the optical response of the BNA when operating in collection mode, we will further adduce the optical response of a BNA operating in emission mode. Emission mode consists of injecting light inside the fiber, however theoretically the Gaussian beam is injected from the end of the metallic fibered tip. The goal of this section is that it clearly verifies the independence of the BNA resonance sensitivity from the operating mode. The optical response, and consequently the resonance sensitivity, only dependent on the geometrical parameters and the on the medium overall refractive index.

#### 3.2.4.1 Resonance wavelength and enhancement factor variation

In figure 3.11 we presents the optical response sensitivity of the BNA to the distance variations. Figures 3.11(a) and (b) present respectively, near field resonance wavelength variation and enhancement factor (at the resonance) of the BNA. Results clearly align with those recorded in collection mode: the $RW$ variation when the BNA is placed in front of a high optical refractive index is significantly greater than that recorded in front of a low refractive index substrate. For an InP substrate the near field $RW$ varies

from $\lambda = 1932\ nm$ to $\lambda = 1365\ nm$ for a distance variation from $D = 0\ nm$ to $D = 10\ nm$. However, for a similar distance variation when the BNA is placed in front of glass substrate the $RW$ variation goes from $\lambda = 1224\ nm$ to $\lambda = 1171\ nm$. On the other hand, the enhancement factor shows a higher intensity than that recorded in collection mode (see figure 3.5) and this is due to the non-leakage of light in the simulation window. We have to note that the normalization in the emission mode is obtained by dividing the results collected at the BNA gap center by the results collected at the same point by removing the metal from the tip, which is at a distance equal to the half-thickness of the metal from the polymer tip.

Due to the similarities in the results for both collection and emission modes we stop the comparison between both modes and assume that all results would be produced with an acceptable difference between both of them. In the following, we will present an experimental study of a BNA operating in collection mode, the study will prove the benefit of using such a system as a remote sensing or as a distance controller.

### 3.2.5 Bowtie antenna

Resonance sensitivity is not only a characteristics related only to the BNA. In fact, any resonant structure should present the same sensitivity phenomena and its optical response will varies as a function of the relative index of the medium. In order to verify this idea we will consider a Bowtie nano-antenna and discuss its sensitivity in term of resonance wavelength and enhancement field in the gap center. We consider a BA with lateral width $L = 220\ nm$ and with a gap dimension $G = 25\ nm$. The BA is suspended in air and separated by a distance $D$ from an InP substrate. See figure 3.12.

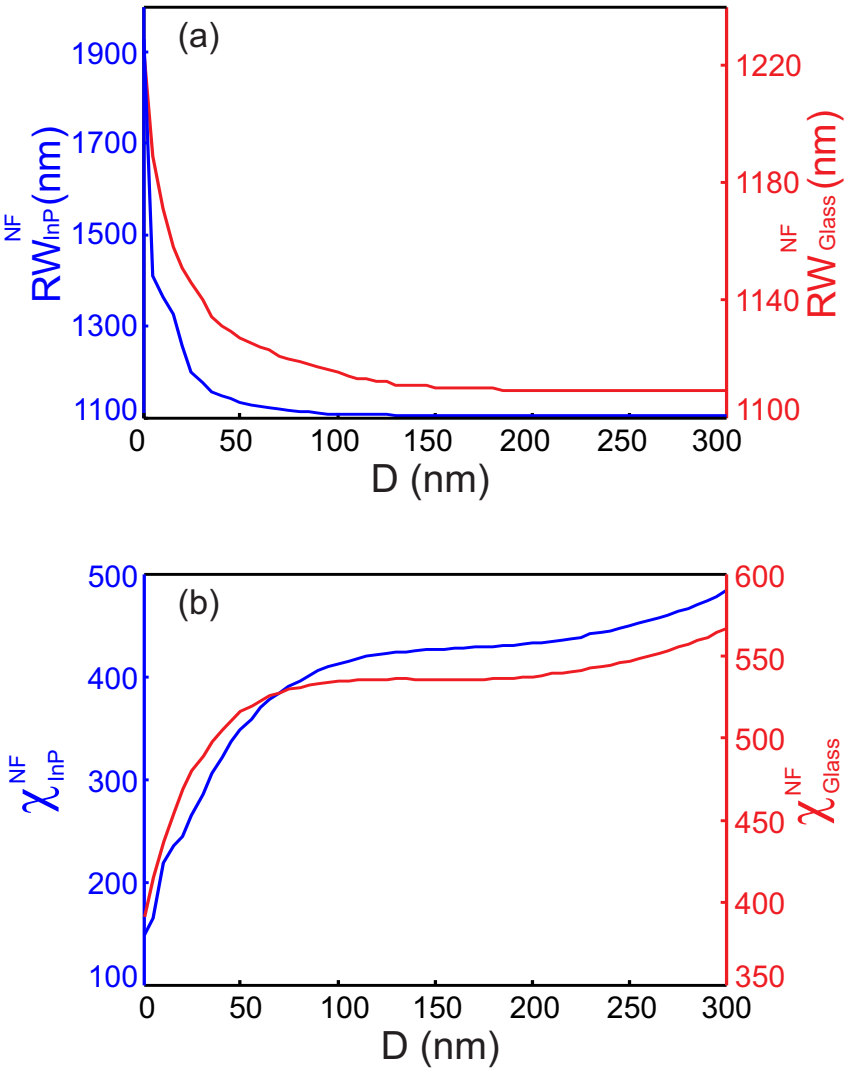


Figure 3.11: Resonance wavelength and enhancement factor variation as a function of the distance from an InP substrate (blue curve) and glass substrate (red curve), respectively. Results are collected in Near Field.

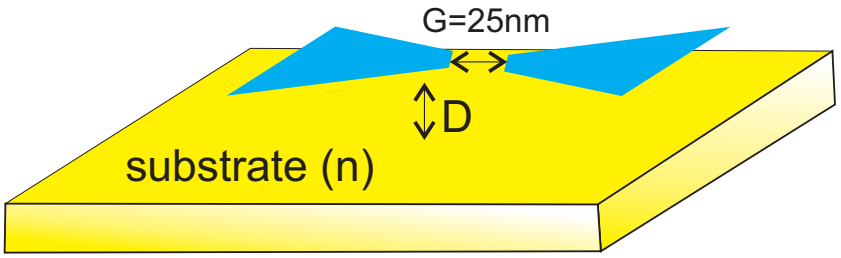


Figure 3.12: Schematic of a bowtie antenna with gap $G = 25\ nm$ placed at a distance D from a substrate with optical index n.

#### 3.2.5.1 Bowtie antenna sensitivity

Resonance sensitivity of the BA is discussed as a function of the distance $D$ separating it from an InP substrate. In figure 3.13(a) we present the resonance wavelength variation while in 3.13(b) we present the resonance intensity variation. We can notice that for a distance variation of 10 $nm$ from $D = 0$ $nm$ to $D = 10$ $nm$ $RW$ goes from 1815 nm to 1122 $nm$ which is bigger than the variation calculated for the BNA in previous section.

However in figure 3.14 we present the intensity variation calculated for three different wavelength we can see that similarly to the case of BNA the BA intensity variation is dependent on the injected light wavelength. For $\lambda = 1100$ $nm$ the intensity present variation present a maxima for $D = 160$ $nm$ while for $\lambda = 1500$ $nm$ the maxima is calculated for $D = 5$ $nm$ and for $\lambda = 1700$ $nm$ the intensity is decreasing when the distance increase.

## 3.3 Experimental study

An experimental study was conducted in order to verify the capability of using a BNA as a remote sensor, in other words to achieve an experimental verification of the high optical sensitivity to the distance variation. The study was conducted thanks to our colleague Ali EL ETER who was working under the supervision of Thierry GROSJEAN. In the following parts we will describe the different parts of the experimental study starting by the fabrication process, then the experimental setup and finally by presenting our results.

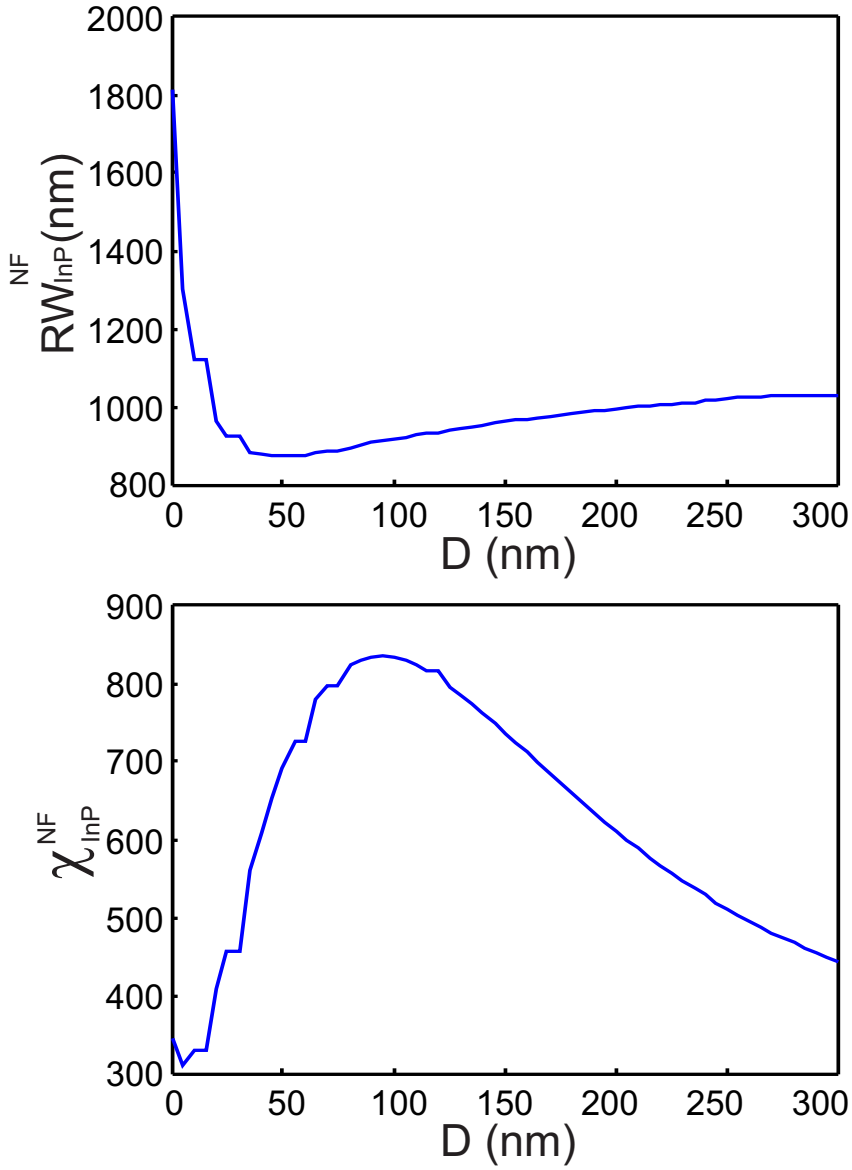


Figure 3.13: Optical response of Bowtie antenna as a function of the distance. (a) Resonance wavelength variation (b) Enhancement factor variation. Results are collected in Near Field.

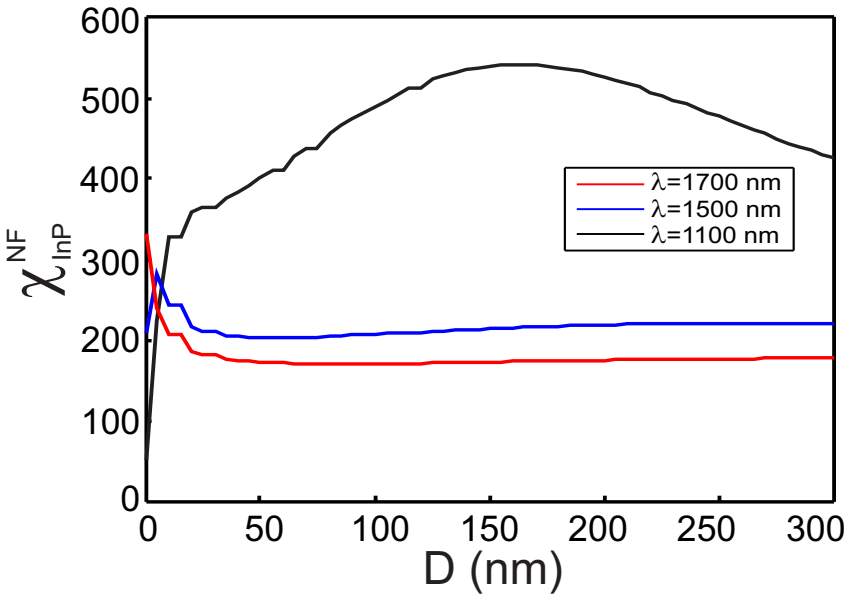


Figure 3.14: Resonance wavelength and enhancement factor variation as a function of the distance fro an InP substrate (blue curve) and glass substrate (red curve), respectively. results are collected in Near Field.

### 3.3.1 Fabrication process

The fabrication of the metallic coated fiber tip involves in several steps. Firstly, a polymer tip is produced at the cleaved facet of an optical fiber, then coating the polymer tip with a metal (aluminum) layer and finally the aperture is engraved at the top of the tip.

#### 3.3.1.1 Tip fabrication

The fabrication of the polymer tip is achieved by LOVALITE company [1]. This startup company is a leader in polymer tip fabrication at the end of an optical fiber. The process involves a drop of polymerizable solution (pentaerythritol triacrylate (polymer) + eosin (photo initiator)) that is deposited at the cleaved end of the fiber. After that, and in order to create a conical-shape polymer tip, laser light must be injected from the other side of the fiber [127]. The illuminated part of the solution would be polymerized in a

[1] http ://www.lovalite.com

conical shape. Then, the tip is immersed in an alcoholic solution which eliminates the non-polymerized solution.

#### 3.3.1.2 Metal coating

Once the polymer tip is created, a metallic (aluminum) layer should cover the tip to allow the confinement of light and eliminate any leakage of light outside the tip. This part is achieved at MIMENTO technology center by using the evaporation techniques. We have to note that to increase the thermal resistance of the metal layer a titanium layer of $5\,nm$ is deposited before the aluminum layer. The titanium layer has no remarkable effects on the optical response of the BNA.

#### 3.3.1.3 Etching

The final step of fabricating the BNA at the top of a metallic coated tip is achieved using a Focal Ion Beam (dual Beam FEI Helios 600i with a Raith Elphy Multibeam attachment)to engrave the metal by respecting the geometrical parameters of the BNA. This step is also achieved at the MIMENTO technical center. Figure 3.15 shows a BNA engraved at the tip apex.

#### 3.3.1.4 Experimental set-up

Nano-antenna is approached to a Si flat surface (commercial wafer) and studied optically with the experimental set-up shown in Figure 3.17. The BNAs on fiber tip are mounted onto a tuning fork and placed into a SNOM head from NT-MDT company (NTEGRA System). A shear-force detection based feedback loop is used to position the tip in close

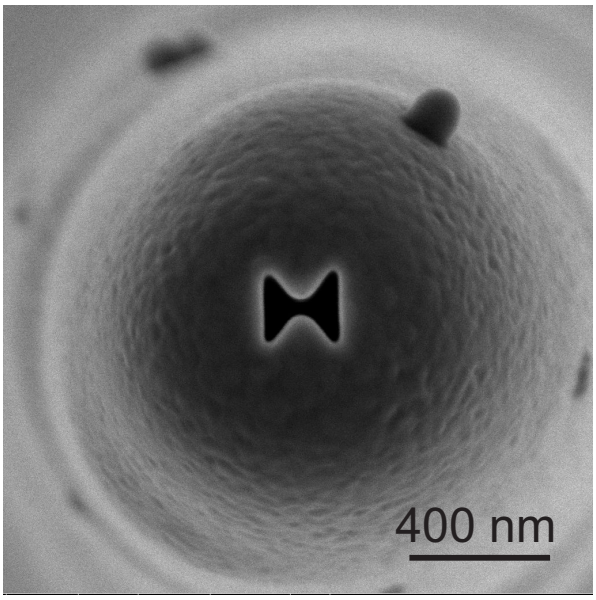


Figure 3.15: SEM micrograph of a BNA on a SNOM fiber tip (top view).

proximity of the surface of the Si wafer. The Si sample is mounted onto a calibrated piezo stage (PI company) to be accurately moved away from the tip along the longitudinal direction (perpendicular to the sample surface). The BNA on tip is used in collection mode. Laser light at $1550\,nm\,(4mW)$ is slightly focused within a lens onto the tip apex through the Si wafer. The fiber output is coupled to an InGaAS photodiode (Thorlabs), and a synchronous detection scheme is used to enhance signal-to-noise ratio. The output voltage is directly monitored with a numerical oscilloscope connected to a computer. The BNA is resonantly excited by aligning the polarization direction of the incident optical waves along the BNA's polarization axis, i.e., the symmetry axis of the BNA that passes through each metal triangle's tip.

### 3.3.2 Experimental results

The experimental study was conducted for two different BNA. The first BNA (BNA1) has the same geometrical parameters as the BNA presented in the theoretical study (see

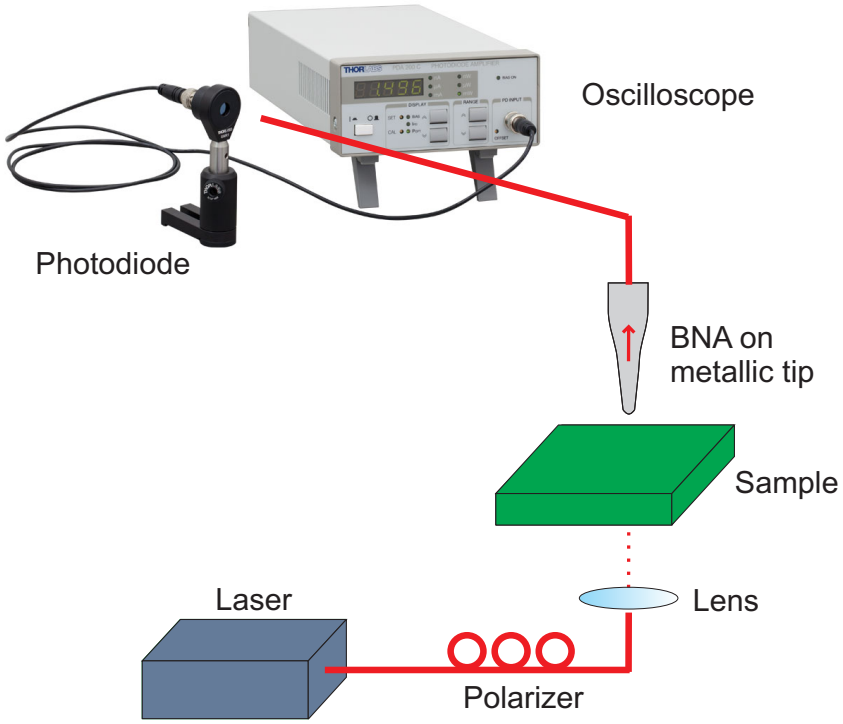


Figure 3.16: Scheme of the experimental set up.

figure 3.1). The second BNA (BNA2) has a smaller gap than BNA1 with 20 $nm$ and a larger lateral side around 250 $nm$. We have previously demonstrated through the theoretical part that BNA1 has a resonance wavelength of 1500 $nm$ when it is placed at $D = 5$ $nm$ from the sample we will see later that the BNA2 presents a resonance wavelength of 1850 $nm$ for the same distance.

#### 3.3.2.1 Polarization

We have mentioned in the previous parts the effect of light polarization on the BNA optical response. Due to its importance, as it indicates the status of the BNA (ON resonance or OFF resonance), we started the experimental study by presenting the polarization diagram see figure 3.17. In fact a weakly focused linearly polarized beam is projected onto the BNA and thus the signal collected by the tip (signal only come from the BNA resonance) is measured as a function of the incident polarization direction. We notice

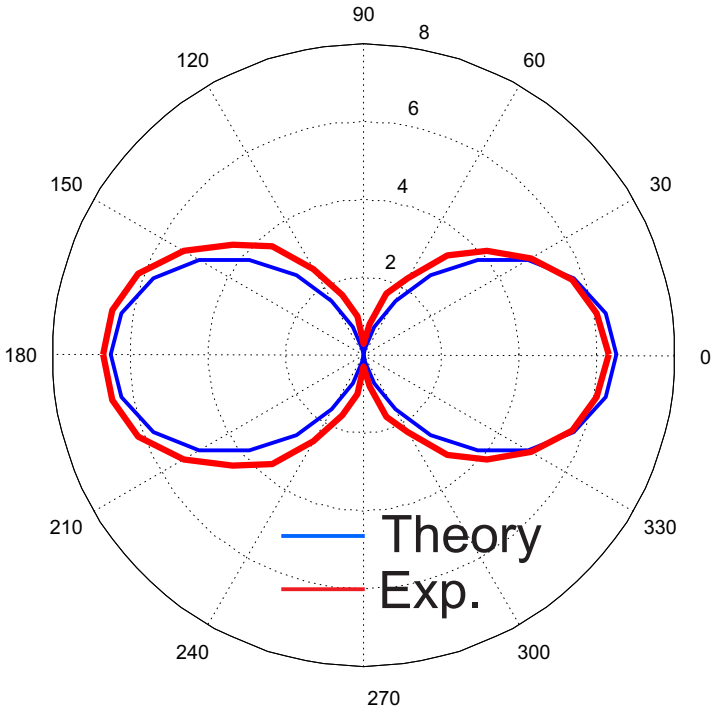


Figure 3.17: Experimental and ideal polarization diagrams of the BNA-on-tip.

that the diagram represents two lobes and is identical to the polarization diagram of an ideal oriented dipole described by a cosine function. The BNA gives a polarization ratio of 1:20 for BNA1 and 1:8 for BNA2.

#### 3.3.2.2 Intensity variation

In figure 3.18 we present the intensity variation as a function of the distance separating the BNA from the sample. We remark that for BNA1 3.18(a) the intensity collected decreases as we increase the distance, whereas for BNA2 3.18(b) the intensity increases as we vary the distance from $D = 20\ nm$ to $D = 45\ nm$, however it decreases as $D$ increases. The point for which the intensity presents a maximum is dependent on multiple parameter: geometric parameters of the BNA, optical index of the substrate as well as the operating wavelength. The closest attempted distance is about $20\ nm$ due to experimental limits as going closer would break our tip, consequently the maximum

presented on figure 3.8 couldn't be verified experimentally.

By calculating the tangential slopes of the experimental curves, we figure out the voltage variation at different points of the curves, which is generally used in the nano-positioning techniques in scanning probe microscopies. BNA1 presents about $-119\,mV.nm^{-1}$, $-41\ mV.nm^{-1}$, $-15\ mV.nm^{-1}$ and $-5\ mV.nm^{-1}$ at tip-to-sample distances of $15\ nm$, $30\ nm$, $100\ nm$ and $200\ nm$, respectively. However, BNA2 experimental curves of Fig. 3.18(b) show local tangential slopes about $233\ mV.nm^{-1}$, $46\ mV.nm^{-1}$, $-19\ mV.nm^{-1}$ and $-4\ mV.nm^{-1}$ for the same distances. Since the millivolt range is beyond the noise level of the current highly sensitive optical detection devices, one can expect with BNA-on-tips distance control schemes to achieve a sub-nanometer accuracy along the longitudinal direction perpendicular to the sample surface. The advantage of using a BNA for distance control comes from the fact that, in case of shear force and atomic force microscopy, transverse spatial resolution can be of the order of the angstrom, thus the spatial sensing depth is limited to a few nanometers. Whereas in the case of a BNA we can expect distance regulation to be at least two orders of magnitude higher with subwavelength sensing lateral area see figure 3.10.

## 3.4 Conclusion

In summary, we have presented a complete theoretical study demonstrating the high resonance sensitivity, of a BNA engraved at the apex of a metallic fibered tip and placed at a distance $D$ from a given substrate, to the distance variation. Theoretical study considered the cases of two substrates, high (InP) and low (Glass) refractive index, and the two possible functional modes (emission and collection) of the BNA. Also we have numerically discussed the optical response of a BNA as a function of the substrate refractive index and

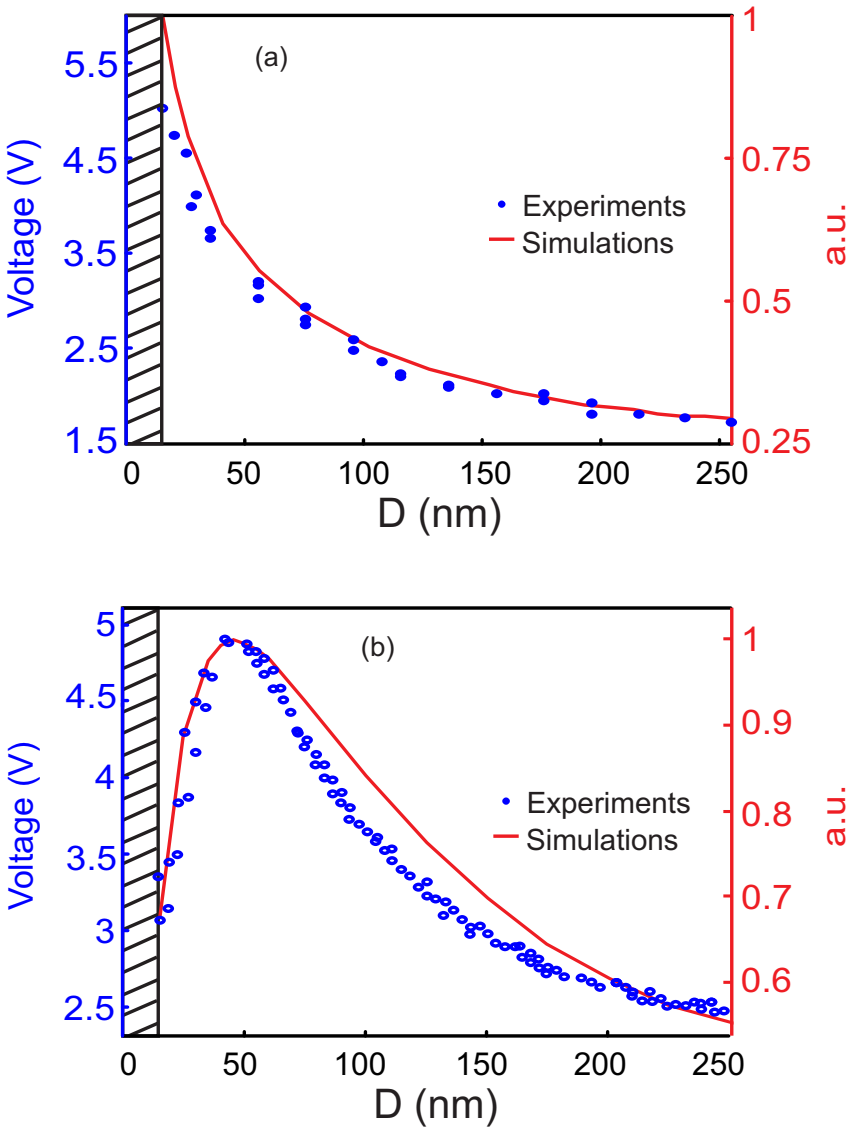


Figure 3.18: Experimental (blue point line) and theoretical (red solid line) result, presenting the variation of the intensity as a function of the distance by injecting a monochromatic light with $\lambda = 1500\ nm$, (a) for the first BNA and, (b) for the second BNA.

when facing a substrate with index step. However, the experimental study only considers the collection mode of a BNA facing a high refractive index substrate. Experimental results are in harmony with the numerical results. The study shows up a novel application for the Bowtie Nano-Aperture (BNA) as a stand-alone optical near-field probes that allows a faithful interaction control with a given sample as a function of the distance separating them. Our results open the way to a new class of nano-positioning technique based on the monitoring of diffraction-free plasmon resonance, offering an alternative to nano-mechanical and diffraction-limited optical interference-based devices.

# Chapter 4

# Modeling of the enhanced Pockels effect by FDTD

## 4.1 Introduction

This chapter is reserved to the study conducted and the steps we implemented in order to build an original FDTD code that was able to simulate the nonlinear optical response coming from the electro-optic (EO) effect in a self-consistent way. In this chapter we will present, in addition to the steps we have taken to develop the code and the assumptions taken into account, a comparison between these results and the ones obtained by using four other different ways to estimate the variation of the refractive index of the medium. The beginning will be by determining the optical index variation in Lithium Niobate (LN) due to the application of an external electric field, conventional Pockels effect, thus we prove the ability of using FDTD to study the Pockels effect. Then we will show the case of a Bragg mirror using a one-dimensional FDTD code as well as a the case of a combination of 2 Bragg separated by a cavity. In addition, we will study the case of two

dimensional Photonic Crystal (PhC) by using a $3D$ periodic FDTD code to evaluate the optical response. All cases will be compared with results that we obtained while using the others methods.

## 4.2 Validation of the classical Pockels effect

We will start our work by simply validating our FDTD algorithm through the simulation of the EO effect in the case of a conventional Pockels effect. For that we will consider a simulation window filled with homogeneous LN material and we will use a $1D$ FDTD code. LN is going to be used as the nonlinear material due to its important physical characteristics [83].

As described previously, the NL effect is introduced into the FDTD algorithm by considering the NL polarizability that leads to an additional current term $\frac{\partial(\varepsilon\chi^{(2)}.\vec{E}\vec{E}_0)}{\partial t}$ in the Maxwell-Ampre equation. The main objective is then to validate the modification of the LN optical index according to the relation [43]:

$$\Delta n = -\frac{1}{2}.r_{33}.n_e^3.E_0 \tag{4.1}$$

Where $n_e = 2.138$ is the refractive index of LN [128], $r_{33} = 33.10^{-12}\ m/V$ is the largest element of the second order susceptibility tensor of LN [111] and $E_0$ is the applied electric field.

To this end we consider a LN simulation window subjected to an homogeneous external electric field with various strength. A monochromatic plane wave $(\lambda = 1000\ nm)$ is then injected inside the window. This wave is linearly polarized along the optical axis

$(OZ)$ of the LN crystal. Consequently, for an external electric field parallel to this axis, only the $z-$component of the polarizability is non zero. We only need to inject this value $P_z = 2\varepsilon_0 r_{33} E_z E_0$ into equation 2.21. Due to the small value of $r_{33}$, we need to consider a very large propagation distance in order to be able to measure the index variation through the modification of the phase velocity of the wave. Then, this variation of the optical refractive index as a function of the applied electric field could be compared to its analytical value mentioned above.

In our simulation we have considered three different strength of the external electric field with $E_0 = 1.10^7\ V/m$, $E_0 = 1.10^8\ V/m$ and $E_0 = 1.10^9\ V/m$ respectively. The calculation of the phase velocity of each wave while applying the electric field leads us to deduce the corresponding index of refraction of the medium and thus to the variation of this index as a function of $E_0$. In the first step we calculate the wavelength of the wave propagating along the window, note that in the FDTD code we inject a monochromatic plane wave with $\lambda = 1000\ nm$. In table 4.1 we show the wavelength of the propagating beam $(\lambda_p)$ for the corresponding $E_0$. $\lambda_p$ is calculated by multiplying the period (the difference between two crests of the graph representing the spatial electric field variation along the propagation axis) by the medium refractive index $n_e$.

| strength of the electric field | $\lambda_p$ |
|---|---|
| 0 | 1000 |
| $10^7$ | 999.30 |
| $10^8$ | 992.45 |
| $10^9$ | 932.16 |

Table 4.1: This table presents the calculated wavelength propagating in Bulk when an electric field $E_0$ is applied.

Consequently, from the results of table 4.1 we can calculate the variation of the refractive index with respect to $E_0$. The calculation of $\Delta n$ is done through the relation:

$$\Delta n = \frac{\lambda}{period} - n_e \tag{4.2}$$

The results showing the variation of the refractive index with respect to the external electric field are given in table 4.2.

| $E_0$ | $\Delta(n)$ FDTD | $\Delta(n)$ Boyd |
|---|---|---|
| 0 | 0 | 0 |
| $10^7$ | $1.612.10^{-3}$ | $1.6125.10^{-3}$ |
| $10^8$ | $1.612.10^{-2}$ | $1.6125.10^{-2}$ |
| $10^9$ | $1.612.10^{-1}$ | $1.6125.10^{-1}$ |

Table 4.2: Variation of the refractive index of the bulk as a function of the applied electric field, results calculated using equation 4.2.

As mentioned above, we have to note that in order to measure the variation of the refractive index in an accurate way we needed to perform the simulation in a very large simulation window. In fact, the variation of the period is so small while applying the external electric field, we had to measure more than 1 period. Our simulation window has 40000 spatial steps along the Z-axis (propagation axis), uniform spatial step $\Delta(z) = 0.5\ nm$ and the calculation was achieved for $nt = 7 \times 10^4$ where nt is the total number of time steps ($\delta t = \Delta(z)/2c$ ; c is the velocity of light in vacuum). This correspond to an interaction real time of $8.33 \times 10^{-19}\ s$ .

These results confirm that the Pockels effect, in its conventional form (bulk materials), is accurately modeled by the FDTD (see table 4.2) when the polarizability term $\vec{P}$ is taken into account in the updated equations 2.19, 2.20 and 2.21. Nonetheless, when assuming that the intrinsic NL properties of the material are modified by electromagnetic confinement, the resolution of Maxwell's equations becomes very difficult due to the dispersion properties induced by the optical response of the nano-structures. The next section is devoted to the presentation of the precise problematic of the FDTD algorithm,

in this case and in the four different methods that were proposed to solve it, including our original self-consistent method.

## 4.3 Enhanced Pockels effect modeling

### 4.3.1 Factual background

As mentioned previously, the EO effect which is a linear effect in the case of bulky media, becomes non-linear when assuming an intrinsic modification of the susceptibility tensor induced by the light confinement. This main assumption that was introduced by [49] and experimentally verified (in a certain configuration) since 2005 by Roussey et al. in refs [51] and H. Lu [65] can be expressed through:

$$\bar{\bar{\chi}}^{(2)}_{mod}(x,y,z,\omega) = \bar{\bar{\chi}}^{(2)}_{bulk}(x,y,z,\omega) f^2_{op}(x,y,z,\omega) \tag{4.3}$$

Where $\bar{\bar{\chi}}^{(2)}_{mod}$ is the modified second order susceptibility of the medium induced by the light confinement, $\bar{\bar{\chi}}^{(2)}_{bulk}$ is the initial second order susceptibility (in bulk where no field confinement exists) and $f_{op}$ is the optical electric field factor given in equation 2.6.

This last equation is at the origin of the non-linearity due to the term $f^2_{op}(x,y,z,\omega)$ that is, in addition, multiplied by $\vec{E}(x,y,z,\omega)$ in the expression of $\vec{P}$ which then becomes:

$$\vec{P}(x,y,z,\omega) = \varepsilon_0 \bar{\bar{\chi}}^{(2)}_{bulk}(x,y,z,\omega) f^2_{op}(x,y,z,\omega) \vec{E}(x,y,z,\omega) \vec{E}_0 \tag{4.4}$$

The implementation of this equation into the FDTD requires to express it in the time space through its Fourier transform which can be writen as:

$$\vec{P}(t) = \varepsilon_0 \int \int_0^{\infty} \int \bar{\bar{\chi}}_b^{(2)}(t_1, t_2, t_3) f_{op}(t - t_1) f_{op}(t - t_2) \vec{E}(t - t_3) \vec{E}_0 dt_1 dt_2 dt_3 \tag{4.5}$$

As we known, the numerical calculation of this triple convolution is a very hard task due to the fact that all six EM field components must be stored at all the computational window nodes and for all time steps. Consequently, some assumptions are needed for its implementation into the FDTD algorithm.

### 4.3.2 General assumptions

The first simplification concerns the anisotropy of LN (linear term $\bar{\bar{\chi}}^{(1)}$). In fact, LN, which is the material of interest in our case, exhibits a quite large birefringence of $\Delta n = 7.3 \times 10^{-2}$ at $\lambda = 1550\ nm$ [1] [83]. Nonetheless, we will assume LN as isotropic with an average optical index of $n = 2.138$ [129, 130]. This approximation will be justified in the following through the comparison of numerical FDTD results demonstrating barely differences between isotropic and anisotropic simulations [87] for the spectral range of interest.

The second assumption that is commonly adopted by theoreticians is to suppose that the material is non dispersive. Consequently, both $\chi_b^{(1)}$ and $\bar{\bar{\chi}}_b^{(2)}$ are considered as invariant function of the EM wavelength. Generally, this approximation is justified whenever we consider a narrow spectral response. For LN, the optical index ($n = \sqrt{1 + \chi_{(1)}}$) is

[1] http://www.lambdaphoto.co.uk/pdfs/Inrad_datasheet_LNB.pdf

ordinarily given by a Sellmeier equation [83] while there are no precise data for the second order susceptibility except at some fixed values of the wavelength ($\lambda = 633\ nm$ and $\lambda = 1550\ nm$ [128, 131]).

Finally, we want to emphasize the fact that, in general, all the three components of the polarizability should be taken into account by the FDTD algorithm. In fact and contrary to the commonly studied configuration in bulk optics where a linearly polarized guided mode inside an LN waveguide is considered, a nano-patterned structure will induce the depolarization of the EM field through the diffraction phenomenon. Consequently, even if experimental data show that the EO coefficient $r_{33}$ is at least 3 times larger than the other coefficients (see equation 2.33), the amplitude of the diffracted electric field can counterbalance this weakness and contribute efficiently to the polarizability. Moreover, this is still valid even if the electrostatic field is aligned along the crystal axis ($\vec{E}_0 = E_0\vec{e}_Z$). More rigorously, the latter field also undergoes depolarization by the presence of a nano-structure but this phenomenon will be neglected in the following 2 structure and will only be discused for the infinit PhC structure (see figure 4.11) .

Taking into account this last remark, and using the expression of $\chi$ as a function of the $r_{ij}$ coefficients, equations 2.34a can be written as:

$$P_{x;nl}(x,y,z,\omega) = 2\epsilon_0 r_{31}^b f_{op}^2(x,y,z,\omega)E_x(x,y,z,\omega)E_{0z}(x,y,z) \tag{4.6a}$$

$$P_{y;nl}(x,y,z,\omega) = 2\epsilon_0 r_{31}^b f_{op}^2(x,y,z,\omega)E_y(x,y,z,\omega)E_{0z}(x,y,z) \tag{4.6b}$$

$$P_{z;nl}(x,y,z,\omega) = 2\epsilon_0 r_{33}^b f_{op}^2(x,y,z,\omega)E_z(x,y,z,\omega)E_{0z}(x,y,z) \tag{4.6c}$$

To implement these equations into the FDTD algorithm, different assumptions for the calculation of the $f_{op}$ term will be adopted leading to different methods that will be detailed and discussed in the next section.

## 4.4 Calculation of the optical field factor $f_{op}$

Estimating the variation of the optical index as a function of the applied electric field was performed in different studies and four different assumptions were used. However, all these methods are based on calculating the variation of the refractive index over the whole medium and then included in an FDTD simulation. On the other hand, the variation of the optical index is calculated through the formula:

$$\Delta n(x,y,z,\omega) = -\frac{1}{2}.n_e^3.r_{33}^{bulk}.f_{op}^2(x,y,z,\omega).f_{el}(x,y,z).E_0 \tag{4.7}$$

Where $f_{el}$ represents the electro-static field factor and $f_{op}$ is the optical factor given as the confinement of the optical electric field in the structure divided by the confinement of the optical electric field in the bulk as shown below.

$$f_{op}(x,y,z,\omega) = \frac{||E_{structure}(x,y,z,\omega)||}{||E_{bulk}(x,y,z,\omega)||} \tag{4.8}$$

The difference between the four methods comes from the way the optical field factor are calculated and consequently the variation of the optical index. Note that the electro-static field factor is considered to be calculated in the same way as the optical field factor but without the contribution of the wavelength.

- In the first approximation, the transmission spectrum of the structure with $E_0 = 0\ V/m$ is calculated using one FDTD simulation and Fourier transform is done to pass from time domain to frequency domain. The average of the optical field confinement in the structure is then calculated at the nearest resonance wavelength $||\vec{E}_{structure}(x,y,z,\lambda_{res})||$ due to the fact that the confinement is maximum

at the resonance. The same steps are repeated for a bulk substrate of LN and the optical field confinement in the bulk is calculated at the same wavelength $||\vec{E}_{bulk}(x, y, z, \lambda_{res})||$. Consequently, the optical field factor is calculated by dividing the two average terms:

$$f_{op}^{Avg\_\lambda_R} = f_{op}(\lambda_{res}) = \int\int\int \frac{||\vec{E}_{structure}(x, y, z, \lambda_{res})||dxdydz}{||\vec{E}_{bulk}(x, y, z, \lambda_{res})||dxdydz} \tag{4.9}$$

- The second approximation focuses on calculating the confinement of the field factor at each point of the structure at the resonance wavelength. Thus the field factor for both structures $||\vec{E}_{structure}||$ and $||\vec{E}_{bulk}||$ are calculated for each spatial position. Note that the field confinement inside the bulk could be taken as a constant since the light is homogenous and so is the substrate.

$$f_{op}^{point\_\lambda_R} = f_{op}(x, y, z, \lambda_{res}) = \frac{||\vec{E}_{structure}(x, y, z, \lambda_{res})||}{||\vec{E}_{bulk}(x, y, z, \lambda_{res})||} \tag{4.10}$$

- In the third method the calculation of the optical field factor would be done for all wavelengths, separately. In fact there is no reason to consider a large $f_{op}$ away from the resonance wavelength. Thus we will calculate the average of the field confinement inside the structure for each wavelength $||\vec{E}_{structure}(x, y, z, \lambda)||$. The same procedure is applied to calculate the field confinement in the bulk LN $||\vec{E}_{bulk}(x, y, z, \lambda)||$

$$f_{op}^{Avg\_\lambda} = f_{op}(\lambda) = \int\int\int \frac{||\vec{E}_{structure}(x, y, z, \lambda)||dxdydz}{||\vec{E}_{bulk}(x, y, z, \lambda)||dxdydz} \tag{4.11}$$

- The fourth approximation is similar to the second one whereas the difference comes from the fact that the field confinement will be calculated in each spatial cell and for all wavelengths, separately. Thus, each spatial cell will have its own $||\vec{E}_{structure}(x,y,z,\lambda)||$, however, the $||\vec{E}_{bulk}(x,y,z,\lambda)||$ could be taken as a constant throughout the bulk and depending on the wavelength only.

$$f_{op}^{point\_\lambda} = f_{op}(x,y,z,\lambda) = \frac{||\vec{E}_{structure}(x,y,z,\lambda)||}{||\vec{E}_{bulk}(x,y,z,\lambda)||} \tag{4.12}$$

In addition to the just cited four methods, we will introduce another (self-consistent) one in which we estimate the variation of the optical index of the medium and the corresponding optical response. However, the variation of the optical index in this method is not achieved directly but through the modification of the second order susceptibility tensor elements. The relation between the second order susceptibility tensor elements and the refractive index of the medium is given by M. Izdebski et al. [132] as:

$$\chi_{ijk} = n^4 r_{ijk} \tag{4.13}$$

in which $n$ is the ordinary refractive index of the medium (LN). After that the modified tensor elements will be introduced in the equation to calculate the nonlinear polarization:

$$\vec{P}_i(x,y,z,\omega) = 2.\epsilon_0.\sum_{ij} \bar{\bar{\chi}}_{ijk}^{modified}(x,y,z,\omega)\vec{E}_{opt}(x,y,z,\omega).\vec{E}_0 \tag{4.14}$$

Therefore, in the self-consistent method the optical field factor in the presence of the substrate is calculated at each time step of the simulation and for each spatial position.

The modification of the optical field factor leads to a modification for the susceptibility tensor elements and consequently to the polarization of the propagating light. We note that the light polarization is also depending on the strength of the applied external electric field.

## 4.5 Comparative study and results

As we have mentioned earlier three types of structures will be studied in the coming sections. We begin with the simplest form of PhC, the Bragg reflector, then we consider the case of two Bragg gratings separated by a cavity, and finally we will present a more complicated form which is a 2 D PhC exhibiting a Fano resonance.

### 4.5.1 Bragg reflector

In the first step the case of a simple 1-D PhC, Bragg reflector, will be treated. A Bragg reflector is a structure composed from multiple layers of alternating media with different refractive index. When the wavelength of the propagating beam in the Bragg is close to four times the optical thickness of the layers, each layer boundary causes a partial reflection which combine through constructive interferences to act as a high quality reflector. The reflectivity efficiency and the band gap width are dependent on the number of the grating periods and on the difference between the refractive indices of the media.

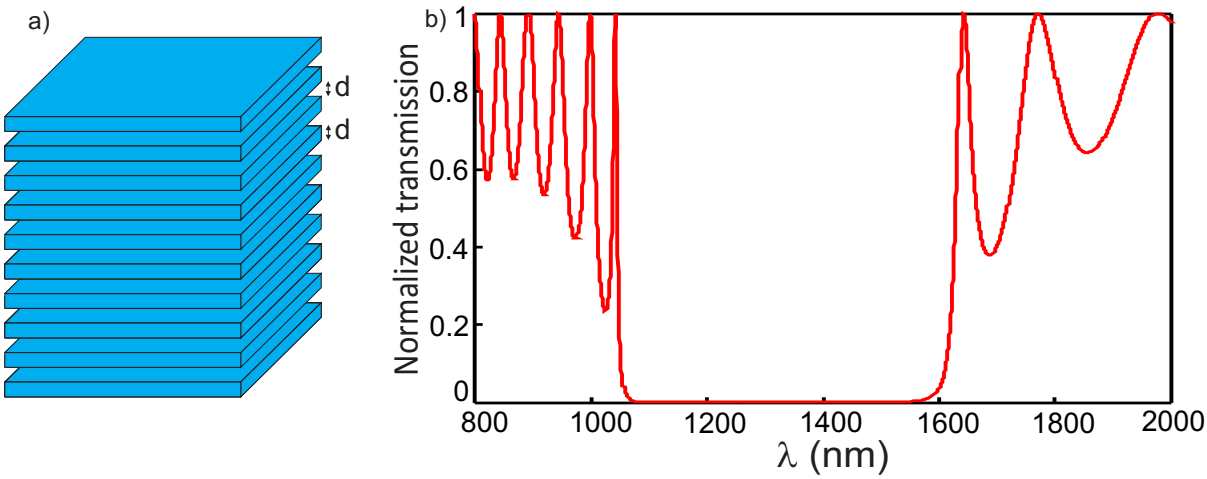


Figure 4.1: In our study we used a 10 layer of LN Bragg reflector, (a) Schematic of the Bragg reflector, (b) the resonance spectrum

#### 4.5.1.1 Optimizing the Bragg geometry

At the beginning we looked for a Bragg reflector with a large band gap and sharp band edge. In our study we have chosen a Bragg reflector (see figure 4.1(a)) composed by alternating 10 layers of LN and vacuum ($n_{LN} = 2.138$ and $n_{vacuum} = 1$) with each layer having a thickness of $200\ nm$. Furthermore, a 3D-FDTD simulation was initiated in order to obtain the resonance spectrum of this Bragg. In our simulation, we apply the PBC along the X-axis and Y-axis and the PML is applied along the Z direction, thus, the structure is infinitely repeated along X and Y. Furthermore, a uniform spatial step is defined along the three direction with $\Delta x = \Delta y = \Delta z = 20\ nm$. The study shows that under these criteria a reflection of 100% occurred for wavelength between $\lambda = 1070\ nm$ and $\lambda = 1600\ nm$.The transmission spectrum is presented in figure 4.1(b). As we can see 10 periods are enough to get almost 100% reflectivity (0% transmission). Vertical edges of the band gap are enough abrupt to allow possible modulation of the transmitted signal.

#### 4.5.1.2 Bragg with applied static field

On the same structure considered earlier, we now apply an external static electric field. and then we study the variation of the refractive index in the LN. The variation of the refractive index of LN layers will induce a shift in the transmission spectrum of the Bragg reflector. The position of the band gap will be modified as well as the sharpness of the band gap edges. In figure 4.2 we present the transmission spectrum of the Bragg reflector as a function of the applied electric field. We notice that the band gap is more red shifted when the strength of the electric field is greater. The external electric field is assumed to be applied using two electrodes placed in parallel with the Brag direction and different voltages were applied. The results collected using the self consistent method for different $E_0$ are presented in figure 4.2. The red curve represents the transmission spectrum corresponding to an applied electric field $E_0 = 10^6\ V/m$, the green curve corresponds to $E_0 = 10^7\ V/m$ and the black one to $E_0 = 10^8\ V/m$. In addition the blue curve represents the spectral response in the absence of any external field in order to compare all the results. We noticed that the slope of the curve corresponding to the higher band gap edge is inversely proportional to the strength of the applied field (there is a decrease when the applied electric field become stronger). However, the lower band gap edge curve does not show an important modification, it is red shifted for stronger electric fields (shifted in the same way as the band gap), while it almost conserves the same slope.

The variation of the high band edge (wavelength at the maximum intensity) versus the strength of the applied static electric field is represented in the inset of figure 4.3. We can see that the variation is not linear and this is due to the confinement of the optical electric field.

The difference between the two band gap limits response under the application of an

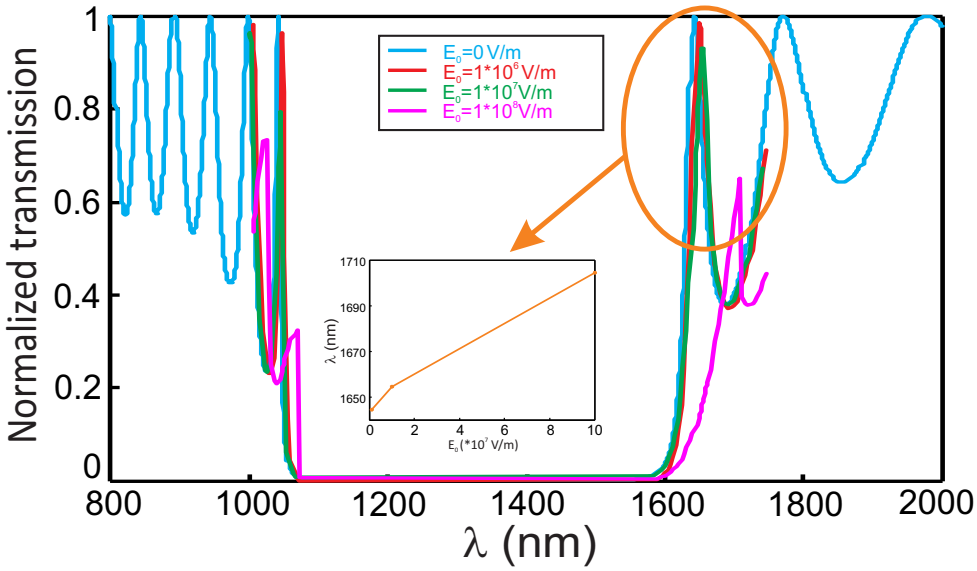


Figure 4.2: Transmission spectrum of the Bragg while applying an external electric field, results are collected using the self consistent method. The inset represent the variation of the wavelength as a function of $E_0$.

external electric field is due to the confinement mode corresponding to each wavelength. In figure 4.3 we present the distribution of the electric field in the structure under the propagation of two monochromatic beams with $\lambda_{low} = 1043\ nm$ (figure 4.3(a)) and $\lambda_{high} = 1643\ nm$ (figure 4.3(c)). For a detailed field variation between the two wavelength figure 4.3(b) and (d) show a cross section of figure 4.3(a) and (c), respectively. The electric field distribution shows that for $\lambda_{low}$ the field is confined in the vacuum layers while for $\lambda_{high}$ the field is confined in the LN layers. Further, the index of vacuum does not change in function of the electric field and only the index of LN layers change which is the reason why the low limits almost conserve its original shape.

We note that for E higher than $E = 10^8\ V/m$ the calculation using the self consistent method diverges. On the other hand, the same calculations using the other methods have all given results that are quite similar, thus, using the simplest method for a structure that does not present a high field confinement is good enough, and no need to complicate the method.

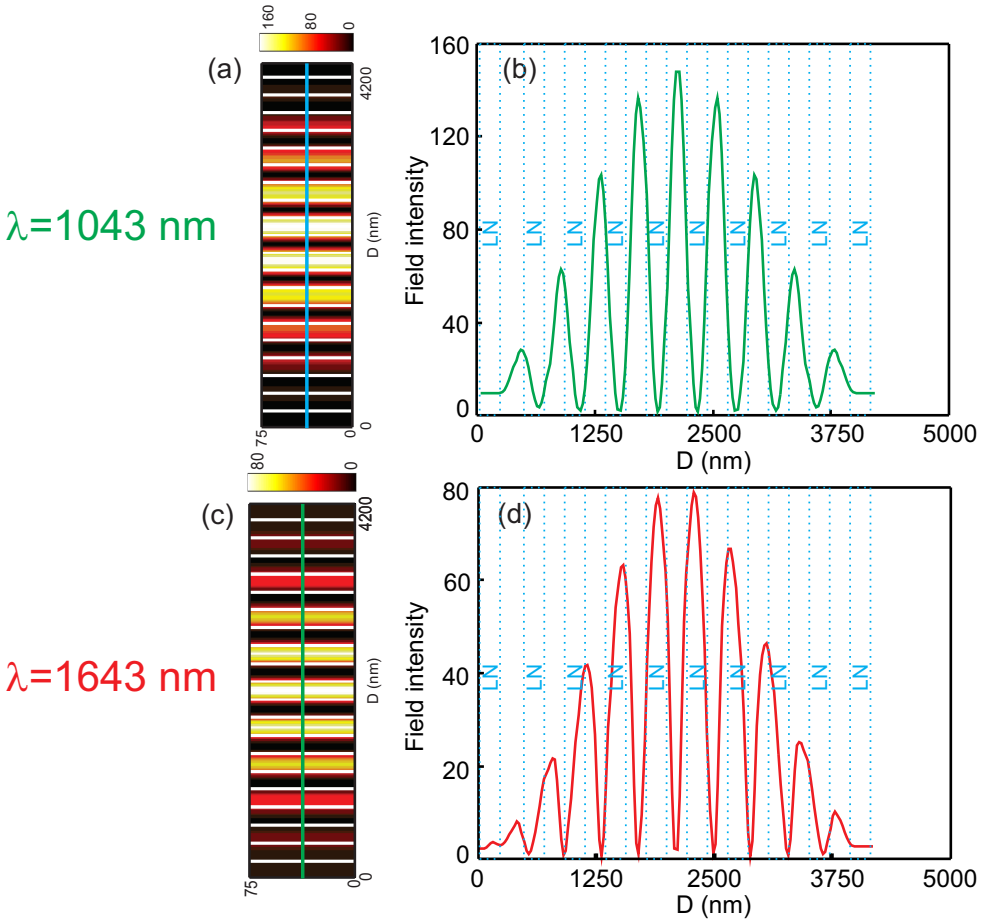


Figure 4.3: (a) Distribution of the electric field inside the Bragg reflector for $\lambda = 1043\ nm$, (b) cross section of the intensity variation along the structure (blue line on (a)), (c) Distribution of the electric field inside the Bragg reflector for $\lambda = 1643\ nm$, (d) cross section of the intensity variation along the structure (green line on (c)).

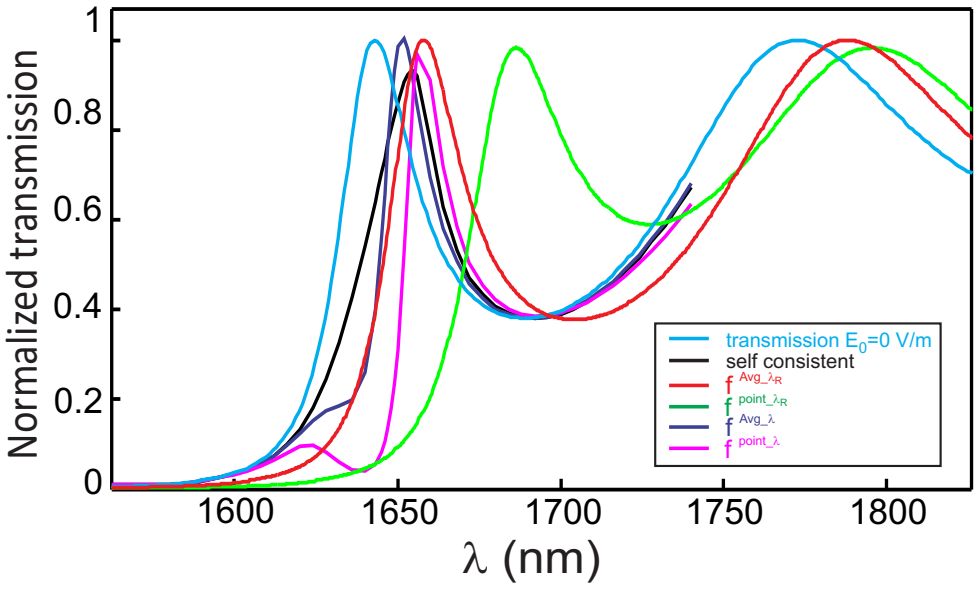


Figure 4.4: Resonance spectrum of the Bragg while applying an external electric field $E_0 = 10^7\ V/m$, all methods are used in order to compare the different response.

#### 4.5.1.3 Comparative study between all methods

A comparative study between various methods to calculate the optical response as a function of the refractive index variation was conducted. In the comparative study we have only considered the application of an external electric field with $E = 10^7\ V/m$, and we assume that for all other EO field the comparison will be similar. The results are shown in figure 4.4, in which, the blue curve shows the optical response in absence of the external field, the black curve corresponds to the self consistent method, and the red represents the optical response while applying the average_resonance method, the green curve is for point_resonance method, the dark blue curve corresponds to the average_lambda method and finally the magenta curve describes the response for the point_lambda method. Note that in figure 4.4 we focus on the high band edge to represent the discrepancy between the results collected from the various methods.

As we can see from these results the difference between outcomes of each method is not very significant. All the methods show the same property for the optical response as

a function of the applied electric field, and that is the intensity at the maximum and the slope of the edge both decrease. Therefore, each method presents a red shift different from the others and the behavior is somewhat different. However, the self consistent results are located around the middle of the other results and it seems to look as an average result between the results of the other methods.

### 4.5.2 Two Bragg separated by a cavity

In this section, we are going to study, in the same way as in the previous section, the case of two Bragg reflector separated by a LN cavity. The structure presents a pronounced resonance with an important quality factor. Thus the electro-magnetic confinements becomes larger allowing a large modification of the optical index.

#### 4.5.2.1 Optimizing the Bragg cavity geometry

Similarly to the Bragg reflector used in the previous section, the Bragg cavity is considered to be the combination of an LN layer separated by a vacuum layer of equal thicknesses. The scheme of the structure is represented in figure 4.5(a) in which the optical response is expected to be directly dependent on the number of layers and the thickness of the cavity. The quality factor of the peak presented in the band gap is related to the number of layers constituting the Bragg however its position is related to the refractive index and thickness of the cavity.

In our case we have chosen each Bragg reflector formed with $5$ LN layers. The cavity is then symmetrical and has a thickness of $D = 330\ nm$. The $5$ layers were sufficient in order to get a peak with an important quality factor (Q) and relatively a important electro-magnetic field confinement. In fact, the quality factor is related to the field factor; field

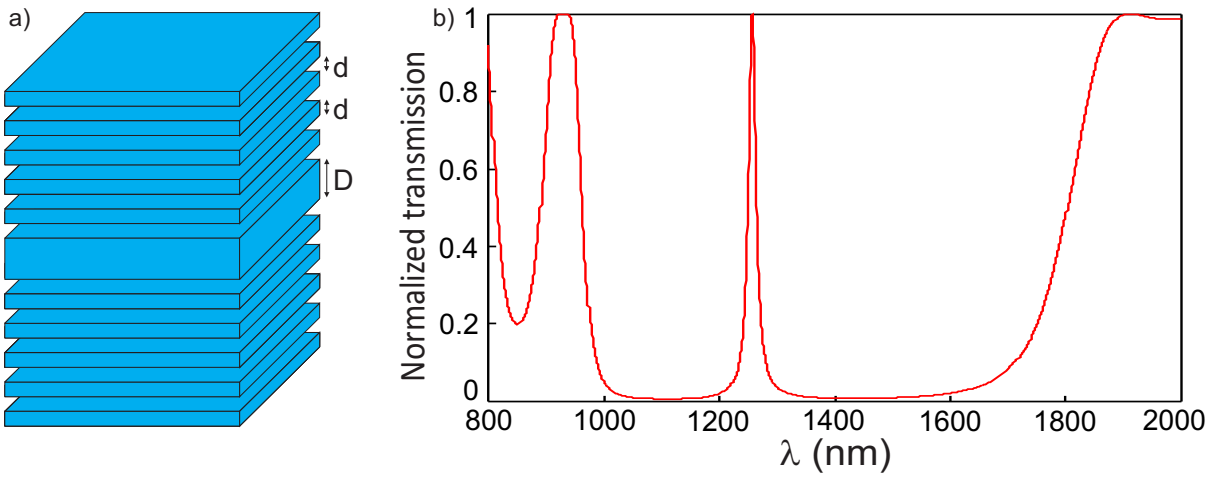


Figure 4.5: A Bragg cavity structure composed of 5 LN layers from each side, (a) schematic of the structure, (b) resonance spectrum.

factor is bigger for high quality factor; thus we were looking for an intermediate quality factor to optimize the optical response of the structure and also the simulation time (simulation time is proportional to the confinement EM field factor). From figure 4.5(b) we see that the optical response of the structure shows a band gap between $\lambda = 1070\,nm$ and $\lambda = 1670\ nm$. Furthermore, we can see that a resonance occurred in the band gap due to the presence of the cavity and the resonance peak of this anomaly is at $\lambda = 1400\ nm$ with a quality factor $Q = 63$.

The simulation was achieved using a periodic 3D-FDTD, the periodicity was applied along the x and y direction, thus, the structure and the light propagation were along the Z-axis. Therefore, the PBC is applied along the X and Y direction and the PML at the upper and down interfaces. The simulation window is spatially discretized with uniform meshing along the three directions with $\Delta x = \Delta y = \Delta z = 10\ nm$.

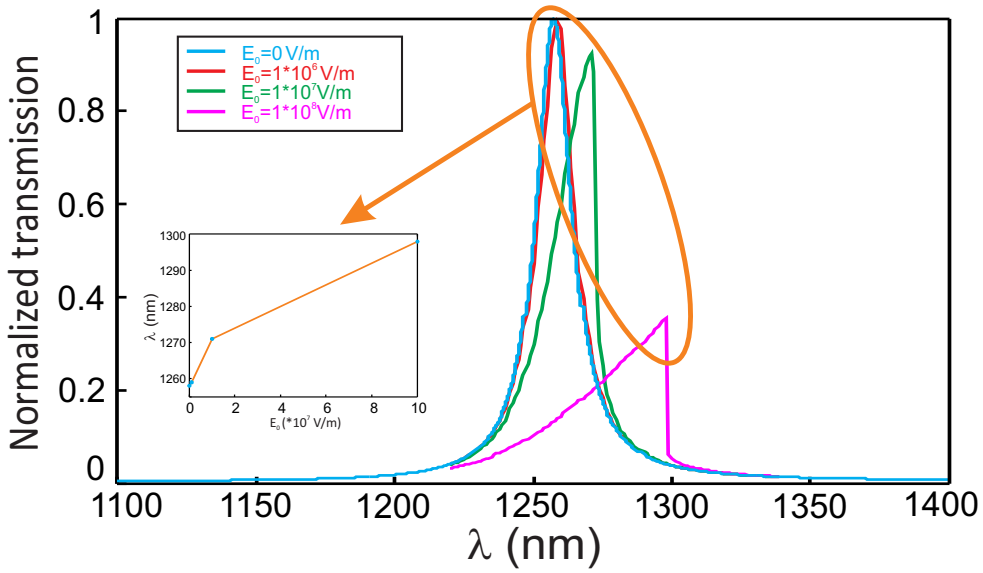


Figure 4.6: Transmission spectrum of the Bragg cavity while applying an external electric field. Results are collected using the self consistent method. The inset represents the variation of the wavelength as a function of $E_0$.

#### 4.5.2.2 Bragg cavity with applied static field

Similarly to the study conducted in the case of one Bragg, we will apply different voltages to our structure and we calculate the optical response corresponding to each case. In figure 4.6 we present the optical response of the structure while applying different voltages using two electrodes placed in parallel to the structure.

In figure 4.6 the blue curve corresponds to an applied external electric field $E = 0\ V/m$, the red curve shows the resonance spectrum corresponding to an applied electric field $E = 10^6\ V/m$, the green curve corresponds to $E = 10^7\ V/m$, and the magenta curve presents the optical response while applying an $E = 10^8\ V/m$. We note that for an $E = 10^5\ V/m$ very small variation of the resonance shift occurred.

From the results we can see that the variation of the applied external electric field has induced a modification in the position of the gap peak and especially on its shape. The resonance wavelength was red shifted when applying an external electric field and

the shift is proportional to the electric field strength (see the inset of figure 4.6), however, the intensity at the resonance is lower for stronger electric fields. On the other hand, the shape of the resonance peak shows an anomaly, which in our opinion comes from the fact that in our self consistent assumption, the modification of the second order tensor, consequently the refractive index, on each spatial cell is dependent on the confinement of the optical electric field in the cell itself. Therefore, the shift induced by the external electric field is limited by the fact that the initial resonance of the structure is sharp, which induced a steep descent on the left side of the resonance peak. The steep descent is located at the left side of the peak because the index of refraction is increasing when applying the external electric field and hence the resonance wavelength is red shifted. We note, that the non-linearity presented by the structure due to the external electric field is of type Duffing [133].

#### 4.5.2.3 Comparative study between different methods for Bragg cavity

In this section we present the comparative study between the different methods cited above. The comparison will be conducted by considering the case of the green curve on figure 4.6 which refers to an applied external electric field of $E_0 = 10^7\ V/m$. The variation of the index of refraction is calculated separately by applying the same external static electric field. This variation is then obtained for each method under the same conditions stated previously and then implemented in the FDTD simulation. Collected results are presented in figure 4.7.

In this figure the blue curve shows the optical response in the absence of an external field, the black curve corresponds to the self consistent method, the red represents the optical response while applying the Average_resonance method, the green curve is for point_resonance method, the dark blue curve corresponds to the average_lambda method

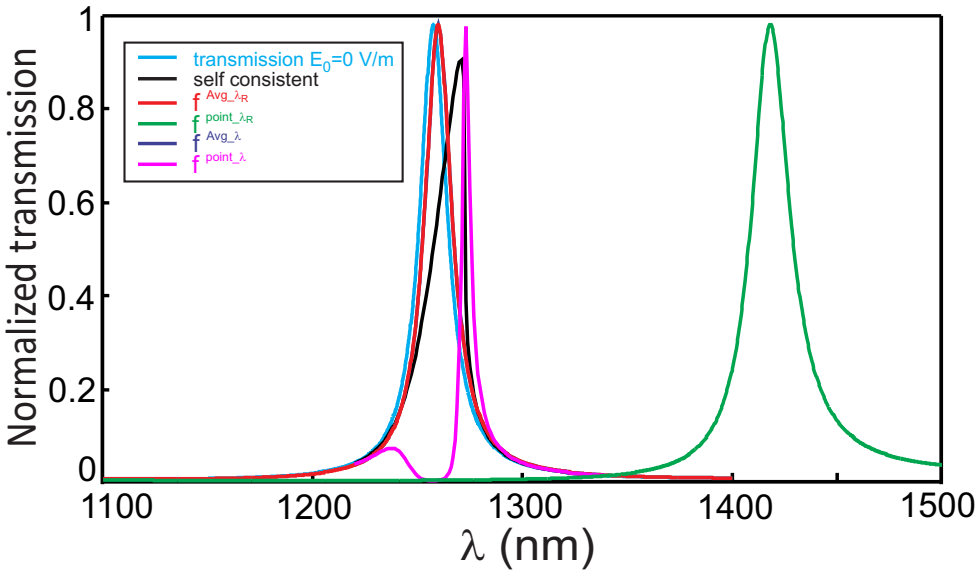


Figure 4.7: Transmission spectrum of the Bragg cavity while applying an external electric field $E_0 = 1.10^7\ V/m$, all methods are used in order to compare the different response.

and finally the magenta curve describes the response for the point_lambda method. Using the average_lambda and the average_resonance methods have conducted to almost the same result (difference of 1 nm), however, the self consistent method and the point_lambda results present almost 2 nm resonance wavelength difference (similar to the Bragg reflector results). The point_resonance method presents a resonance wavelength so far from the other methods (as the electro-magnetic field confinement increase the resonance presented by this method become farther than the resonance calculated using the other methods).

Similarly to the case of the Bragg study, we did not collect the same result using the different methods. However the difference between the results corresponding to each method has become more important. Furthermore, the results collected by the self consistent method are the only ones showing a steep on the left side of the band gap peak and that is due to the variation of the refractive index during the simulation, which is not existing in the other methods. This steep descent appeared on the left side of the band

gap peak since the refractive index is increasing when we apply an external electric field and consequently the peak is red shifted.

### 4.5.3 Infinite PhC

In this last part of the chapter we will study a more complicated structure. We choose a PhC that presents a Fano resonance in order to make a comparative study with a well known structure that was experimentally studied in our team. The PhC in use is a square lattice of air holes milled in LN as shown in figure 4.8. In our model we consider an infinite PhC. The PhC has a period $p_y$ along the $Y$ direction and $p_x = 2p_y$ along the $X$ direction. In addition a shift $s$ is applied to the hole position in every two columns of air holes as schematically shown in figure 4.8(a). This structure was studied extensively by Wentao QIU during her PhD studies and based on her study we have chosen specific geometrical parameters to get resonance near the telecome wavelength. The PhC has a period $a = 630\ nm$, $s = 30\ nm$ and a thickness $t = 700\ nm$, and the holes have a radius $r = 230\ nm$.

The simulation study is achieved using a periodic $3D$-FDTD code, therefore, a computational window of $2a \times a$ in the $XY$ plane is needed. The structure is illuminated by a plan wave traveling along the Z-axis (normal incidence). PBC is applied along the $X$ and $Y$ direction, thus, the simulation consider an infinite structure along these two axes. However, the PML is applied along the Z-axis to eliminate the parasite reflections from the window edges. Spatial step is defined to be uniform along the $X$ and $Y$ with $\delta x = \delta y = 30\ nm$ and non-uniform along the Z-axis where the smaller step $\delta z = 35\ nm$ is applied around the structure and the bigger step $\Delta z = 45\ nm$ is applied in the remaining parts of the window; Non-uniform meshing is applied to well describe the structure thickness and to reduce the calculation time. On the other hand,

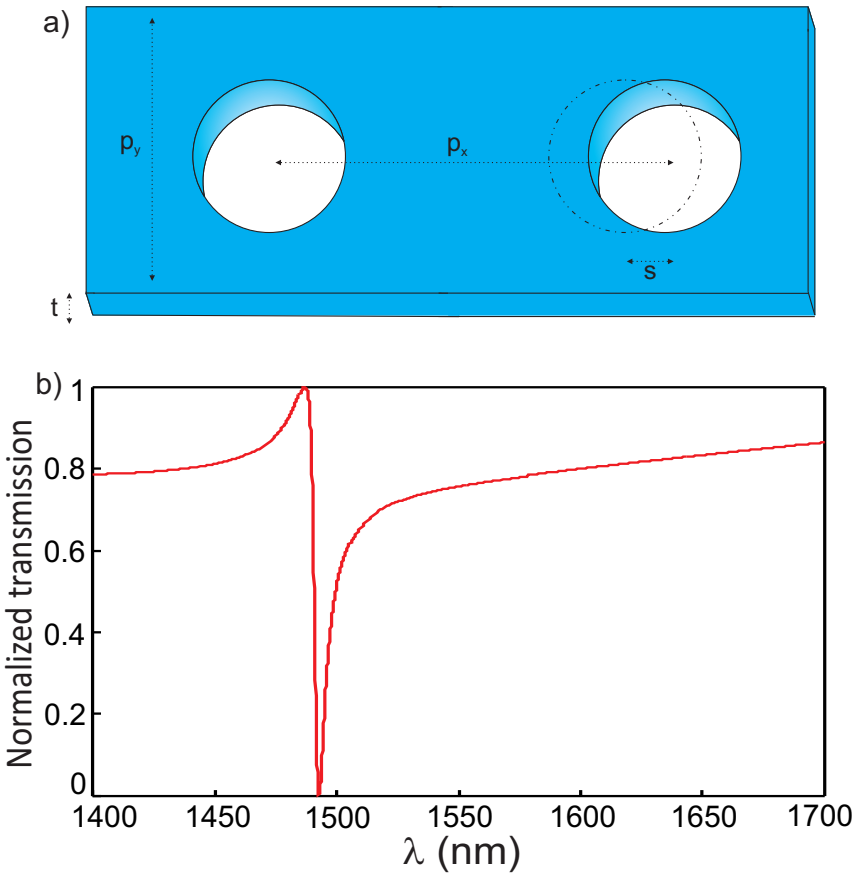


Figure 4.8: 2D PhC composed by holes engraved in a LN substrate, (a) schematic of the structure in which $t$ is the thickness of the LN substrate $p_x$ is the PhC period along the X-axis, $p_y$ the period along the Y-axis and s is the displacement of the second hole column, (b) the optical response of the structure when illuminated by a plane wave with $\lambda = 1000\ nm$.

a sampling technique is applied to define the refractive index distribution by considering the mean value of neighboring cells, leading to a faithful description of the cylindrical air holes. This technique allows us to eliminate any rough change, in terms of refractive index, between two neighboring cells (it only work for dielectric media).

In figure 4.8(b) we show the optical response of the PhC for a wavelength between 1400 nm and 1700 nm when no external electric field is applied. From the graph we see that the transmission spectrum shows a Fano deep resonance for $\lambda_{res} = 1492\ nm$ with a quality factor $Q = 290$. We note that in the study achieved by QUI et al [87] the authors discussed the effect of different geometric parameters on the resonance wavelength

position. In our work, we only chose this specific parameter in order to make a comparison with experimental results for different electric field strength.

#### 4.5.3.1 2D PhC with applied static field

The influence of an applied static electric field on the refractive index of the medium, consequently, on the optical response of the PhC is discussed in this section.

In figure 4.9, we represent the optical response of the PhC, collected by using the self consistent method, when applying two different electric field $E_0 = 3 \times 10^6\ V/m$ and $E_0 = 8.5 \times 10^6\ V/m$. The self consistent method shows a discontinuity between $\lambda = 1504\ nm$ and $\lambda = 1510\ nm$ for $E_0 = 3 \times 10^6\ V/m$ and between $\lambda = 1514\ nm$ and $\lambda = 1518\ nm$ for $E_0 = 8.5 \times 10^6\ V/m$ (around the expected resonance wavelength). This discontinuity comes in fact from the divergence of the simulations when injecting a beam in that wavelength range. For those wavelengths, where the confinement is optimal, the field factor at some cells becomes very high due to the high confinement of light. Therefore, the refractive index, which is updated at each time step of the simulation, undergoes a high variation at consecutive time steps which leads to the divergence of the simulation see figure 4.10.

#### 4.5.3.2 Effect of the electro-static field factor

In the previous parts of this study we have only consider the effect of the optical field factor and neglecting the contribution of the electro-static field factor (the previous structure were not presenting a complex geometry). However, in the PhC crystal and as we can see from figure 4.11(a) the distribution of the external electric field is not homogenous along the structure. The optical response of the structure, for both $E_0$, is red shifted relatively

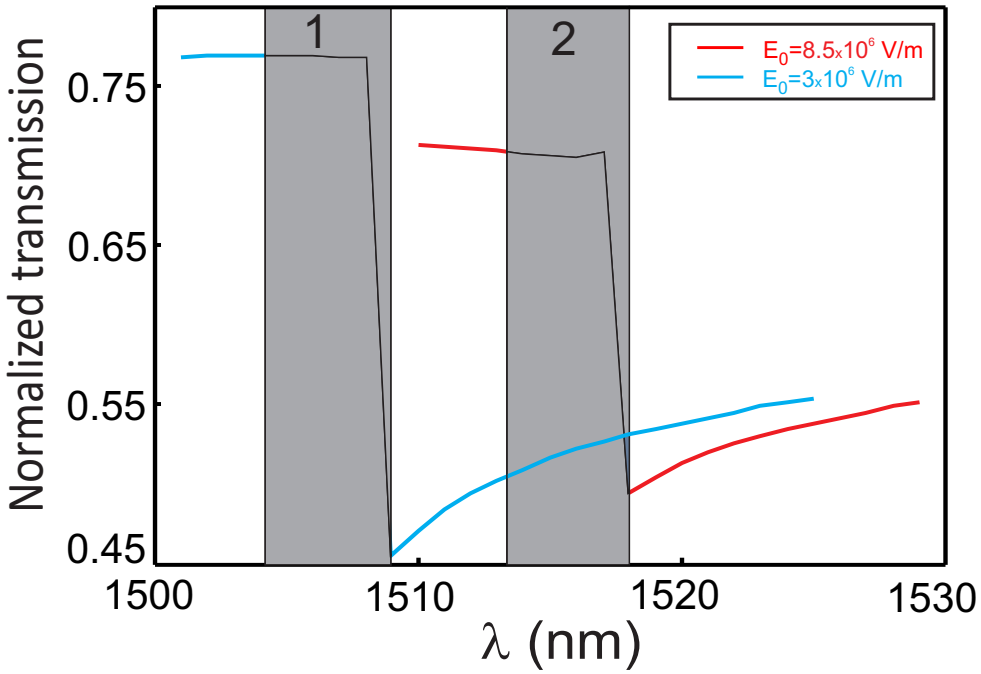


Figure 4.9: The optical response of the PhC when applying different external electric field and by using (a) the self consistent method. The gray zone correspond to the wavelength where the simulation have diverged.

to the one presented in figure 4.9. As well the divergence wavelength has also bee shifted to the red (figure 4.11(b)).

#### 4.5.3.3 Comparative study case of PhC

In this section we are going to compare the results collected by the self consistent method with the 4 other ones. The study was achieved by considering a static electric field strength $E_0 = 8.5 \times 10^6\ V/m$ (red curve of figure 4.9) and the results are presented in figure 4.12. The optical response of the PhC while using the average_lambda method shows a deep resonance at $\lambda = 1509\ nm$ (dark blue curve of figure 4.12), however the point_lambda method gives a resonance at $\lambda = 1529\ nm$ (magenta curve of figure 4.12). On the other hand, the average_resonance (red curve) and the point_resonance (green curve) shows respectively, a resonance at $\lambda = 1586\ nm$ and $\lambda = 1703\ nm$.

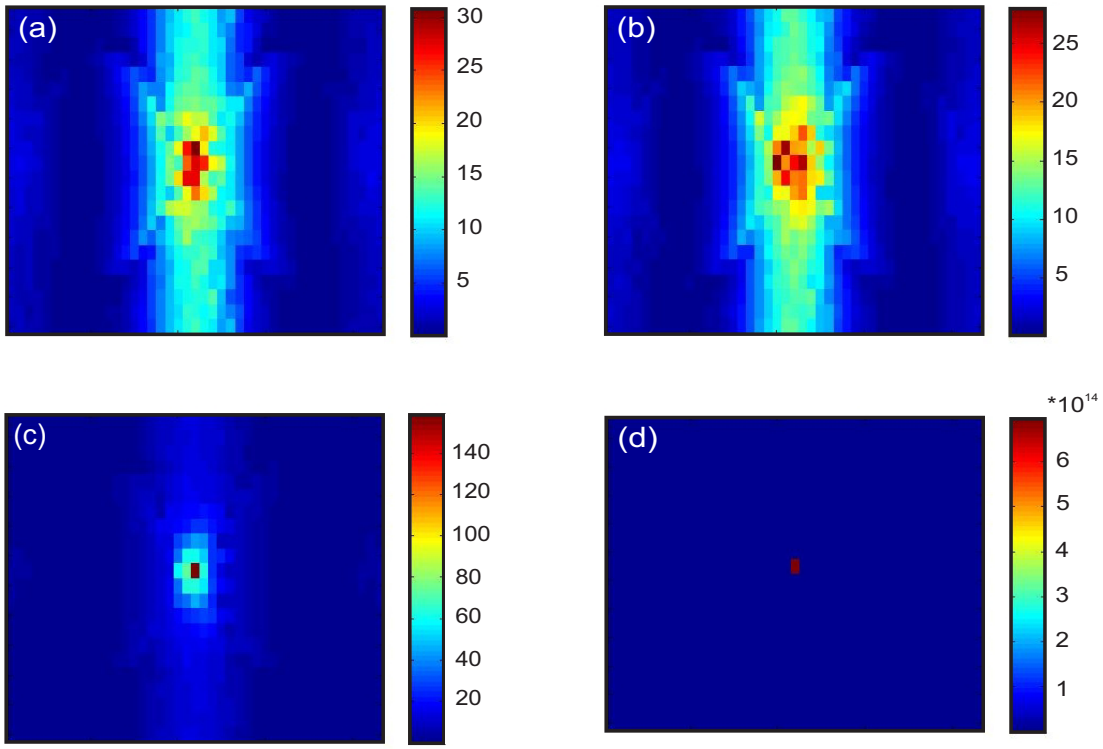


Figure 4.10: Distribution of the field factor all over the PhC, (a) 4 time steps before divergence, (b) 3 time steps before divergence, (c) 2 time steps before divergence and (d) 1 time step before divergence.

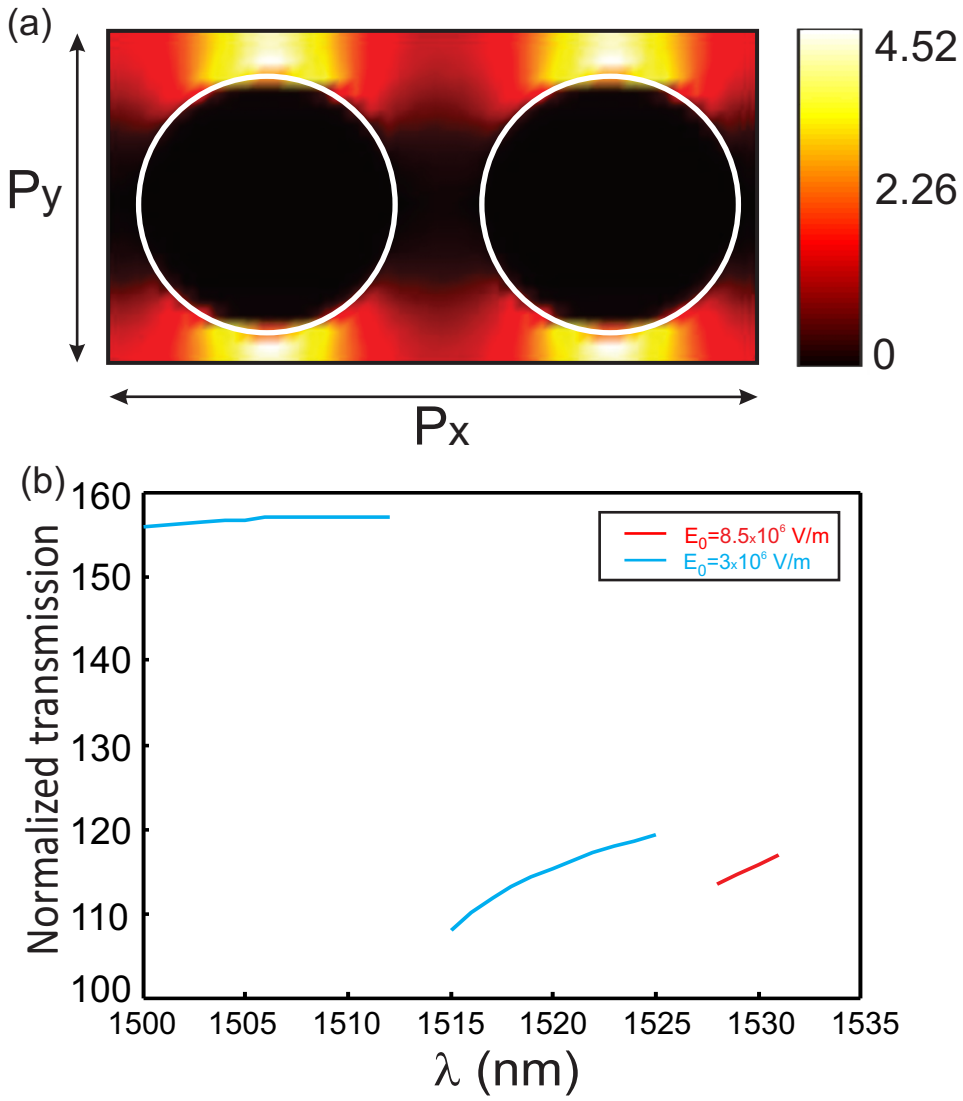


Figure 4.11: (a) Distribution of the static electric field along the structure, (b) optical response by taking into account the contribution of $f_{el}$ (missing points correspond to a diverging wavelength).

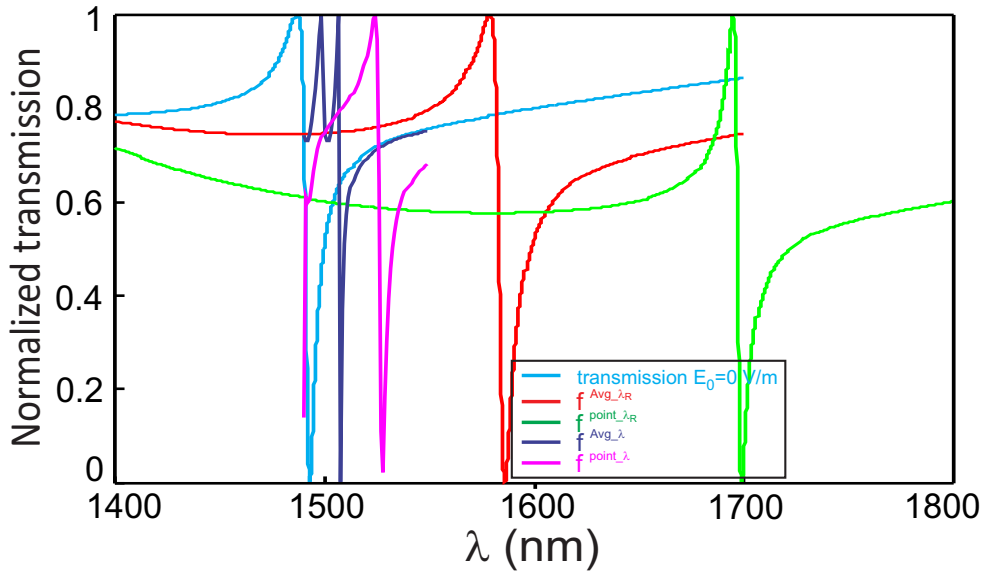


Figure 4.12: The optical response by using different optical field calculation methods and considering an electric field $E_0 = 8.5 \times 10^6\ V/m$.

As we can see, these results show somehow a similarity to the results collected by the other methods. Result collected by the self consistent method and the one by the point_lambda method, present a small difference (about 5 nm) in term of the resonance wavelength. This difference as we can see has become larger while going from a Bragg reflector structure to the current structure, due to the difference if the confinement factor. As well, the point_resonance method continue to presents a resonance wavelength so far from the all other methods.

#### 4.5.3.4 Comparison with experimental results

An experimental study of this structure has also been conducted by (Wentao QIU Abdullaye NDAO) and the results obtained show that when heating the structure the resonance shifts with respect to the temperature in a quasi linear form (see figure 4.13). A relationship between the Pyro-electric effect and the EO effect is given through the relationship defining the static electric field in terms of the temperature:

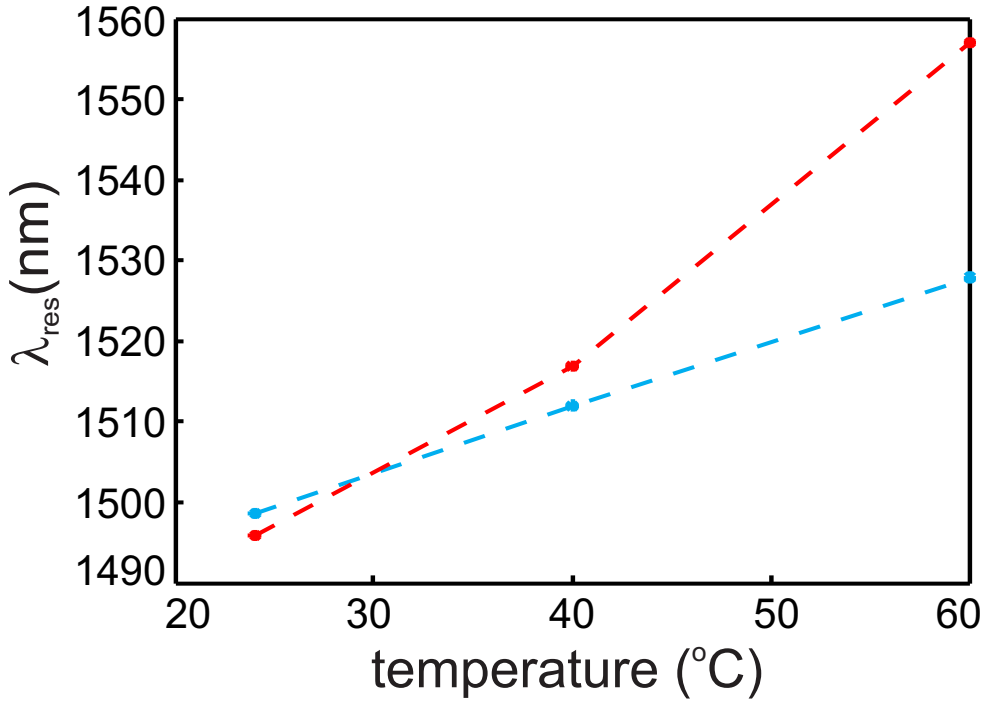


Figure 4.13: Experimental result showing the resonance wavelength as a function of the PhC temperature.

$$\Delta n = \frac{1}{2} n_e^3 r_{33} E_0 \qquad \text{where} \qquad E_0 = \frac{1}{\varepsilon_0 \varepsilon_r} \rho \Delta T \tag{4.15}$$

Where $\varepsilon_0$ and $\varepsilon_r$ are the vacuum the LN and relative electrostatic dielectric constants ($\varepsilon_r = 28.7$), and $\rho$ is the pyro-electric coefficient ($\rho = -6{\times}10{-}5\, Cm^{-2}K^{-1}$). From equation 4.15 we can calculate that a temperature variation $\Delta T = 36^oC$ corresponds to a static field $E_0 = 8.5 \times 10^6\ V/M$. From figure 4.13 for $T = 60\ ^oC$ a resonance wavelength of $\Delta\lambda = 50\ nm$ is recorded. This result is comparable to red curve in figure 4.9 as they both correspond to $E_0 = 8.5 \times 10^6\ V/m$. By comparing both results we can see that the shift recorded experimentally is more significant than the shifts collected using the average_lambda and point_lambda methods.

In the theoretical results, the EO effect is the only effect that modifies the optical response of the structure, however, in the experiment multiple effects can affect the optical

response such as the mechanical stress which comes from heating the structure, and due to this heat process the geometry of the structure could be modified and consequently the optical response would also be modified.

#### 4.5.3.5 Effect of time step on the divergence

The divergence of simulations when using the self consistent method requires more intensive studies in order to bypass it. For that, we have studied the influence of the time step $\Delta t$ at the diverging point. In the main code we were using the FDTD stability condition to define the time step (see equation 2.23), thus we require to minimize the time step in a way that the difference of $\Delta n$ at a consecutive time steps remains acceptable. Therefore, we choose to study the case of an applied $E_0 = 8.5 \times 10^6\ V/M$ and for $\lambda = 1517\ nm$ which is expected to be the resonance wavelength and we decrease the time step by a factor of 2 in order to conserve reasonable simulation time. The variation of the diverging point have presented a slightly nonlinear variation, unfortunately, we cannot count on it to bypass the divergence. High confinement of the optical field in the structure leads to a variation of the refractive index of the medium in an unphysical way (see figure 4.10). Various ways could be used to overcome this limitation. For example by minimizing the spatial step size. However it is worth noting that in the results that we presented, we have only taken into account the optical field factor and assuming a static electric field that has only one component along the axis of propagation. Introducing the other components and the electro-static field factor will be another challenge with more complicated diverging sources. This approach will not be discussed in this work, nevertheless, it constitutes a new challenge to be undertaken.

## 4.6 Conclusion

This chapter was reserved to the study of the EO effect of various structures. Various methods have been used to study the effect of an applied electric field on the optical response of the structure and a new method has been presented in order to estimate the variation of the refractive index in a self consistent way.

The beginning was by validating the conventional Pockels effect in bulk where no confinement of optical electric field is present. In order to validate the variation of the refractive index of the medium as a function of the applied electric field, we have calculated the phase velocity of the propagating beam. The results collected and presented in table 4.2 show a high accordance between analytical and numerical results.

In addition, a study discussing the case of a 1D PhC has been conducted. In the study we have considered two different structures: a simple Bragg reflector with 10 layers and a Bragg cavity structure described in figure 4.5. The results obtained show a modification of the optical response of the structure which comes from the variation of the refractive index. A comparison between the results corresponding to each structure shows that in the case of a Bragg reflector results obtained using the various methods are more close than the results in the case of the Bragg cavity. In addition, the self-consistent method diverges for a lower applied electric field in the case of the Bragg cavity. The difference between the two structures comes from the fact that the field is more confined in the case of the Bragg cavity which leads to a higher field factor and consequently to a higher variation of the refractive index at consecutive time steps.

In the last part of this chapter we discussed a more complicated structure by considering a 2D PhC. As in the case of the previous structure a comparison study between different methods have demonstrated that the higher is the field confinement in the struc-

ture the more different are the results corresponding to each method, and the divergence in the case of the self consistent method appears now for a lower static field.

# Chapter 5

# Conclusion and Perspectives

To end our this thesis we will present a general conclusion for the studies that we have presented. In addition, some perspectives for future studies are suggested.

## 5.1 Conclusion

In our work we have discussed two different optical aspects: the linear optical response of a BNA and the electro-optic effect of 1D and 2D PhC. The confinement of light in the structure was the reason behind both effects and their proposed applications. In the BNA case, the dependency of the volume mode and the optical properties of the structure to the medium effective index were the reason behind the high sensitivity of the BNA which paved the way toward a new alternative nano-positioning technique. However, the optical confinement of light in the PhC in addition to an external static electric field are the reason of the variation of the medium refractive index, consequently, to the appearance of the EO effect.

### 5.1.1 Sensitivity of the BNA

In the first section of the thesis, we have presented the ability of using a BNA, engraved at the apex of a metal-coated tip, as an optical technique of nano-positioning based on the monitoring of diffraction-free plasmon resonance, offering an alternative to nano-mechanical and diffraction-limited optical interference-based devices. In our work we have conducted a full theoretical study and an experimental study in order to validate our theoretical results. In the theoretical study we have considered the emission mode and the collection mode of the antenna, as well we have discussed the cases of two different substrates (high and low refractive index) and a view of the resonance wavelength variation of the BNA with respect to the refractive index of the substrate placed at a distance $D$. Therefore, a 3D-FDTD code, was used to complete the numerical simulation and we note that we implemented a linear Drude dispersion model to well describe the metal properties and we used the perfectly matching layer to eliminate any reflection of light from the simulation window interfaces.

On the other hand, in the experimental study we have discussed the case of a BNA operating only in collection mode. The study discusses the case of two different BNA (BNA1 and BNA2), with different geometrical parameters, when they are placed in front of a high refractive index substrate (silicon $n = 3.4$). Experimental results present a high accordance with the one recorded in the theoretical study. BNA1 presented experimentally a sensitivity of about $-119\ mV.nm^{-1}$, $-41\ mV.nm^{-1}$, $-15\ mV.nm^{-1}$ and $-5\ mV.nm^{-1}$ at tip-to-sample distances of $15\ nm$, $30\ nm$, $100\ nm$ and $200\ nm$, respectively. However, BNA2 experimental curves of Fig. 3.18(c) show local tangential slopes of about $233\ mV.nm^{-1}$, $46\ mV.nm^{-1}$, $-19\ mV.nm^{-1}$ and $-4\ mV.nm^{-1}$ for the same distances. Thus, in the case of a BNA we can expect distance regulation to be at least two orders of magnitude higher than the sensitivity corresponding to shear

force and atomic force microscopy techniques.

We conclude that the BNA sensitivity is dependent on various parameters, such as the antenna geometry, the refractive index of the sample in front and the separating distance between the antenna and the sample. The sensitivity of the antenna is higher for small distances, because the confinement mode localized in the gap of the antenna is more affected by the displacement of the substrate. In other words, the confinement mode of the BNA localized at the gap center is at the origin of the sensitivity phenomena measured in our study, thus, the sensitivity of the BNA is proportional to the light confinement in the vicinity of the BNA.

### 5.1.2 Electro-optic effect

In the second part of our work, we were concerned with studying the EO effect of different types of PhC going from the simplest (Bragg reflector) to a more complicated PhC (holes engraved in LN substrate). In this study we were looking to present a new algorithm in which we estimate the variation of the medium refractive index directly in the code and at each time step.

We have proposed an algorithm in which the variation of the refractive index of the medium is instantaneous, the variation of the index is described by the variation of the second order susceptibility tensor elements. Results of this method were compared with the results collected with 4 different other methods and to the results of the experimental study for the case of the 2D PhC. The study demonstrates that the application of the self consistent method is limited by various diverging sources and the efficiency of its results could vary depending on the structure in use (optical field factor). In the case of a Bragg reflector the applied electric field is limited to be less than $E_0 = 10^9\ V/m$ however, it

is smaller than that in the case of a Bragg gratting with cavity and much smaller in the case of 2D PhC. The limit of the applied electric field is related to the variation of the refractive index between two consecutive time steps.

On the other hand, results collected by the other 4 methods have as well presented a dissimilarity for different structures. In these methods the variation of the refractive index is calculated separately and implemented in the FDTD code thus the refractive index of the medium does not change during the simulation. The results collected by those methods and the one corresponding to the self consistent method were quite similar for the case of Bragg reflector in which the confinement of light is smaller than the others two structures. Whereas the difference between the results collected by the various methods became larger in the case of the Bragg reflector with cavity structure and even more so for the 2D PhC. This dissimilarity is due to the difference in the light confinement factor for each structure. For high light confinement the optical field factor become higher and consequently $\Delta n$ becomes bigger.

The light confinement is at the origin of various optical phenomena. In our study we have demonstrated that this confinement plays the key role behind the high sensitivity of the BNA to a sample placed at a distance D in front of it. As well, this confinement is one of the main reasons behind the variation of the medium refractive index when this medium is subjected to an applied external electric field (EO effect).

## 5.2 Perspective

Modeling the EO effect of an optical structure remains an important goal to achieve. As we have show in our experiments, an important difference between the results collected by the experimental study and the theoretical one still exists even while using different

methods. This difference is proportional to the confinement of light in the structure as well to the strength of the applied static electric field. Various physical effects could appear during the experimental study which are not defined in our simulation code. These could be incorporated in future work by:

- Studying the mechanical stress coming from heating the sample and looking into the existence of other physical effects in order to be introduced in our FDTD code, which then allows a faithful study of the electro-optics effect that could be dependent on other phenomena in addition to its dependency on the strength of the electric field and light confinement.

- Bypassing the diverging source of the self consistent method coming from the high value of the optical field factor and thus making the difference between the susceptibility tensor elements at two consecutive time steps become very large.

- Modeling the BNA in order to enhance its lateral and vertical sensitivity to the distance from a sample. However many other studies could take place to benefit from the high confinement of light in a small region (gap zone).

# Publication

## List of publication

**Paper 1** Etude numrique de la rsonance dŠune nano-antenne optique ouverture papillon Elie M. Atie, Ali El Eter, Thierry Grosjean, Tony Tannous et Fadi I. Baida Lebanese sciences journal

**Paper 2** Fiber-integrated optical nano-tweezer based on a bowtie-aperture nano-antenna at the apex of a SNOM tip El Eter, Ali; Hameed, Nyha M; Baida, Fadi I; Salut, Roland; Filiatre, Claudine; Nedeljkovic, Dusan; Atie, Elie; Bole, Samuel; Grosjean, Thierry Optics Express, Vol. 22 Issue 8, pp.10072-10080 (2014)

**Paper 3** Light funneling from a photonic crystal laser cavity to a nano-antenna: overcoming the diffraction limit in optical energy transfer down to the nanoscale Mivelle, Mathieu; Viktorovitch, Pierre; Baida, Fadi I; El Eter, Ali; Xie, Zhihua; Vo, Than-Phong; Atie, Elie; Burr, Geoffrey W; Nedeljkovic, Dusan; Rauch, Jean-Yves; Callard, Sgolne; Grosjean, Thierry Optics Express, Vol. 22 Issue 12, pp.15075-15087 (2014)

**Paper 4** High optical resonance sensitivity to its environmentof a fibred Bowtie Nano-aperture Antenna Elie M. Atie, Tony Tannous, Thierry Grosjean and Fadi I. Baida Applied Physics B, Vol 120 Issue 4, pp. 581-586 (2015)

**Paper 5** Remote optical sensing on the nanometer scale with a bowtie aperture nano-antenna on a fiber tip of scanning near-field optical microscopy Elie M. Atie, Zhihua Xie, Ali El Eter, Roland Salut, Dusan Nedeljkovic, Tony Tannous, Fadi I. Baida, and Thierry Grosjean Appl. Phys. Lett. Vol 106, 151104 (2015)

# Peer-reviewed Conference Proceedings

## Oral Presentations

**Oral 1** Etude numrique de la rsonance dŠune nano-antenne optique pour des applications en biologie Elie Atie, T. Grosjean, Tony Tannous, Ali El Eter, Abdoulaye Ndao et Fadi I. Baida seconde Journe Franco-Libanaise, ULCO, 22-25 Octobre 2013

**Oral 2** NanostructureŠs fabrication and applications in nano-optics E. Atie, M.-P. Bernal, A. Ndao, A. El Eter, T. Grosjean, C. Guyot, N. Courjal, R. Salut, F. Chollet, T. Tannous and F. I. Baida Workshop of Nanotechnology, Lebanese University, 28-29 Avril 2014

**Oral 3** Resonance sensitivity of a fibered Bowtie Nano-Aperture E. Atie, Z. Xie, A. El Eter, R. Salut, D. Nedeljkovic, Tony Tannous, T. Grosjean et F. I. Baida OSA Photonics day, FEMTO-ST Besancon, 4 Decembre 2014

**Oral 4** Bowtie nano-antenna mounted on a fibered tip for different applications: tweezers and remote sensing. Elie M. ATIE, Ali El ETER, Nyha M. HAMEEd, Zhihua XIE, Roland SALUT, Tony TANNOUS, Thierry GROSJEAN and Fadi I. BAIDA Le 18me Forum des microscopies  sonde locale, Troyes, 16-20 mars 2015 Page 30

## Poster Contributions

**Poster 1** Sensibilit de la rsonance dŠune nano-antenne optique  ouverture papillon fibre Elie Atie, Tony Tannous, T. Grosjean et Fadi I. Baida 34mes Journes Nationales d'Optique Guide (JNOG), Nice France, 29-31 octobre 2014

# Bibliography

[1] I Abdoulkader Ibrahim, Mathieu Mivelle, T Grosjean, J-T Allegre, GW Burr et FI Baida : Bowtie-shaped nanoaperture: a modal study. *Opt. Lett.*, 35(14):2448–2450, 2010.

[2] Kane S. Yee et others : Numerical solution of initial boundary value problems involving Maxwells equations in isotropic media. *IEEE Trans. Antennas Propag*, 14(3):302–307, 1966.

[3] Allen Taflove et Morris E. Brodwin : Numerical solution of steady-state electromagnetic scattering problems using the time-dependent Maxwell's equations. *IEEE Trans. Microw. Theory Tech.*, 23(8):623–630, 1975.

[4] Theodore H Maiman : Stimulated optical radiation in ruby. 1960.

[5] Jean-Claude Weeber, Alain Dereux, Christian Girard, Joachim R Krenn et Jean-Pierre Goudonnet : Plasmon polaritons of metallic nanowires for controlling submicron propagation of light. *Phys. Rev. B*, 60(12):9061, 1999.

[6] OL Muskens, V Giannini, JA Sssnchez-Gil et J Gmez Rivas : Optical scattering resonances of single and coupled dimer plasmonic nanoantennas. *Opt. Express*, 15(26):17736–17746, 2007.

[7] Uwe KREIBIG et Michael VOLLMER : *Optical properties of metal clusters*, volume 25. Springer Science & Business Media, 2013.

[8] B PALPANT, B PRÉVEL, J LERMÉ, E COTTANCIN, M PELLARIN, M TREILLEUX, A PEREZ, JL VIALLE et M BROYER : Optical properties of gold clusters in the size range 2–4 nm. *Phys. Rev. B*, 57(3):1963, 1998.

[9] K Lance KELLY, Eduardo CORONADO, Lin Lin ZHAO et George C SCHATZ : The optical properties of metal nanoparticles: the influence of size, shape, and dielectric environment. *J. Phys. Chem. B*, 107(3):668–677, 2003.

[10] Javier AIZPURUA, Garnett W BRYANT, Lee J RICHTER, FJ García DE ABAJO, Brian K KELLEY et T MALLOUK : Optical properties of coupled metallic nanorods for field-enhanced spectroscopy. *Phys. Rev. B*, 71(23):235420, 2005.

[11] David P FROMM, Arvind SUNDARAMURTHY, P James SCHUCK, Gordon KINO et WE MOERNER : Gap-dependent optical coupling of single bowtie nanoantennas resonant in the visible. *Nano Lett.*, 4(5):957–961, 2004.

[12] Holger FISCHER et Olivier JF MARTIN : Engineering the optical response of plasmonic nanoantennas. *Opt. Express*, 16(12):9144–9154, 2008.

[13] Nan ZHOU, Edward C KINZEL et Xianfan XU : Complementary bowtie aperture for localizing and enhancing optical magnetic field. *Opt. Lett.*, 36(15):2764–2766, 2011.

[14] T GROSJEAN, Mathieu MIVELLE, FI BAIDA, GW BURR et UC FISCHER : Diabolo nanoantenna for enhancing and confining the magnetic optical field. *Nano Lett.*, 11(3):1009–1013, 2011.

[15] K SENDUR et W CHALLENER : Near-field radiation of bow-tie antennas and apertures at optical frequencies. *J. Microsc*, 210(3):279–283, 2003.

[16] Liang WANG et Xianfan XU : High transmission nanoscale bowtie-shaped aperture probe for near-field optical imaging. *Appl. Phys. Lett.*, 90(26):261105, 2007.

[17] Valentin FLAURAUD, Thomas S van ZANTEN, Mathieu MIVELLE, Carlo MANZO, Maria F GARCIA PARAJO et Jurgen BRUGGER : Large-scale arrays of bowtie nanoaperture antennas for nanoscale dynamics in living cell membranes. *Nano Lett.*, 15(6):4176–4182, 2015.

[18] Guowei LU, Wenqiang LI, Tianyue ZHANG, Song YUE, Jie LIU, Lei HOU, Zhi LI et Qihuang GONG : Plasmonic-enhanced molecular fluorescence within isolated bowtie nano-apertures. *Acs Nano*, 6(2):1438–1448, 2012.

[19] Fadi I BAIDA et Thierry GROSJEAN : Double-way spectral tunability for the control of optical nanocavity resonance. *Sci. Rep.*, 5, 2015.

[20] Lukas NOVOTNY et Niek VAN HULST : Antennas for light. *Nat. Photon*, 5(2):83–90, 2011.

[21] Dae-Seo PARK, Hyun Jun KIM, Se Geun PARK, El-Hang LEE, Seung Gol LEE *et al.* : Effect of incident beam width on light transmission enhancement by bow-tie-shaped nano-aperture. *Jpn. J. Appl. Phys*, 46(12R):7991, 2007.

[22] Mathieu MIVELLE, Pierre VIKTOROVITCH, Fadi I BAIDA, Ali EL ETER, Zhihua XIE, Than-Phong VO, Elie ATIE, Geoffrey W BURR, Dusan NEDELJKOVIC, Jean-Yves RAUCH *et al.* : Light funneling from a photonic crystal laser cavity to a nano-antenna: overcoming the diffraction limit in optical energy transfer down to the nanoscale. *Opt. Express*, 22(12):15075–15087, 2014.

[23] Elie M ATIE, Zhihua XIE, Ali EL ETER, Roland SALUT, Dusan NEDELJKOVIC, Tony TANNOUS, Fadi I BAIDA et Thierry GROSJEAN : Remote optical sensing on

the nanometer scale with a bowtie aperture nano-antenna on a fiber tip of scanning near-field optical microscopy. *Appl. Phys. Lett.*, 106(15):151104, 2015.

[24] Ertugrul CUBUKCU, Nanfang YU, Elizabeth J SMYTHE, Laurent DIEHL, Kenneth B CROZIER et Federico CAPASSO : Plasmonic laser antennas and related devices. *IEEE J. Sel. Top. Quantum Electron.*, 14(6):1448–1461, 2008.

[25] Encai HAO et George C SCHATZ : Electromagnetic fields around silver nanoparticles and dimers. *J. Chem. Phys.*, 120(1):357–366, 2004.

[26] Hongcang GUO, Todd P MEYRATH, Thomas ZENTGRAF, Na LIU, Liwei FU, Heinz SCHWEIZER et Harald GIESSEN : Optical resonances of bowtie slot antennas and their geometry and material dependence. *Opt. Express*, 16(11):7756–7766, 2008.

[27] Bedir B YOUSIF et Ahmed S SAMRA : Modeling of optical nanoantennas. *Phys. Res. Int.*, 2012, 2012.

[28] Robert D GROBER, Robert J SCHOELKOPF et Daniel E PROBER : Optical antenna: Towards a unity efficiency near-field optical probe. *Appl. Phys. Lett.*, 70(11):1354–1356, 1997.

[29] RICHARDC COMPTON, ROSSC MCPHEDRAN, Zorana POPOVIC, GABRIELM REBEIZ, Peter TONG et D RUTLEDGE : Bow-tie antennas on a dielectric half-space: theory and experiment. *IEEE Trans. Antennas. Propag.*, 35(6):622–631, 1987.

[30] E OESTERSCHULZE, G GEORGIEV, M MÜLLER-WIEGAND, A VOLLKOPF et O RUDOW : Transmission line probe based on a bow-tie antenna. *J. Microsc*, 202(1):39–44, 2001.

[31] Liang WANG, Sreemanth M UPPULURI, Eric X JIN et Xianfan XU : Nanolithography using high transmission nanoscale bowtie apertures. *Nano Lett.*, 6(3):361–364, 2006.

[32] Xiaolei WEN, Luis M TRAVERSO, Pornsak SRISUNGSITTHISUNTI, Xianfan XU et Euclid E MOON : Optical nanolithography with $\lambda/15$ resolution using bowtie aperture array. *Appl. Phys. A*, 117(1):307–311, 2014.

[33] Maurizio RIGHINI, Giovanni VOLPE, Christian GIRARD, Dmitri PETROV et Romain QUIDANT : Surface plasmon optical tweezers: tunable optical manipulation in the femtonewton range. *Phys. Rev. Lett.*, 100(18):186804, 2008.

[34] Chang CHEN, Mathieu L JUAN, Yi LI, Guido MAES, Gustaaf BORGHS, Pol VAN DORPE et Romain QUIDANT : Enhanced optical trapping and arrangement of nano-objects in a plasmonic nanocavity. *Nano Lett.*, 12(1):125–132, 2011.

[35] Yuanjie PANG et Reuven GORDON : Optical trapping of a single protein. *Nano Lett.*, 12(1):402–406, 2011.

[36] Brian J ROXWORTHY, Kaspar D KO, Anil KUMAR, Kin Hung FUNG, Edmond KC CHOW, Gang Logan LIU, Nicholas X FANG et Kimani C TOUSSAINT JR : Application of plasmonic bowtie nanoantenna arrays for optical trapping, stacking, and sorting. *Nano Lett.*, 12(2):796–801, 2012.

[37] Brian J ROXWORTHY et Kimani C TOUSSAINT JR : Femtosecond-pulsed plasmonic nanotweezers. *Sci. Rep.*, 2, 2012.

[38] I-Chun HUANG, Russel JENSEN, Ou CHEN, Jennifer CHOY, Thomas BISCHOF, Moungi BAWENDI et Marko LONCAR : Optical trapping of a colloidal quantum dot. *In CLEO: QELS_Fundamental Science*, pages FF2C–5. Optical Society of America, 2015.

[39] Nyha M HAMEED, Ali EL ETER, Thierry GROSJEAN et Fadi I BAIDA : Stand-alone three-dimensional optical tweezers based on fibred bowtie nanoaperture. *IEEE Photon. J.*, 6(4):1–10, 2014.

[40] Ali EL ETER, Nyha M HAMEED, Fadi I BAIDA, Roland SALUT, Claudine FILIATRE, Dusan NEDELJKOVIC, Elie ATIE, Samuel BOLE et Thierry GROSJEAN : Fiber-integrated optical nano-tweezer based on a bowtie-aperture nano-antenna at the apex of a snom tip. *Opt. Express*, 22(8):10072–10080, 2014.

[41] Zhilong RAO, Lambertus HESSELINK et James S HARRIS : High-intensity bowtie-shaped nano-aperture vertical-cavity surface-emitting laser for near-field optics. *Opt. Lett.*, 32(14):1995–1997, 2007.

[42] Mathieu MIVELLE, Thomas S van ZANTEN, Lars NEUMANN, Niek F van HULST et Maria F GARCIA-PARAJO : Ultrabright bowtie nanoaperture antenna probes studied by single molecule fluorescence. *Nano Lett.*, 12(11):5972–5978, 2012.

[43] Robert W. BOYD : *Nonlinear optics*. Academic press, 2003.

[44] Alexandre BOUHELIER, M BEVERSLUIS, Achim HARTSCHUH et Lukas NOVOTNY : Near-field second-harmonic generation induced by local field enhancement. *Phys. Rev. Lett.*, 90(1):013903, 2003.

[45] EH BARAKAT, M-P BERNAL et FI BAIDA : Second harmonic generation enhancement by use of annular aperture arrays embedded into silver and filled by lithium niobate. *Opt. Express*, 18(7):6530–6536, 2010.

[46] Rodney LOUDON : The raman effect in crystals. *Adv. Phys*, 13(52):423–482, 1964.

[47] Maxim KARPOV, Hairun GUO, Arne KORDTS, Victor BRASCH, Martin HP PFEIFFER, Michail ZERVAS, Michael GEISELMANN et Tobias J KIPPENBERG : Raman

self-frequency shift of dissipative kerr solitons in an optical microresonator. *Phys. Rev. Lett.*, 116(10):103902, 2016.

[48] Osamu ASO, Masateru TADAKUMA et Shu NAMIKI : Four-wave mixing in optical fibers and its applications. *dEp*, 1:2, 1999.

[49] Luca RAZZARI, Denis TRÄGER, Magali ASTIC, Philippe DELAYE, Robert FREY, Gérald ROOSEN et Régis ANDRÉ : Kerr and four-wave mixing spectroscopy at the band edge of one-dimensional photonic crystals. *Appl. Phys. Lett.*, 86(23):231106, 2005.

[50] Q WU et X-C ZHANG : Free-space electro-optic sampling of terahertz beams. *Appl. Phys. Lett.*, 67(24):3523–3525, 1995.

[51] M ROUSSEY, M-P BERNAL, N COURJAL, D VAN LABEKE, FI BAIDA et R SALUT : Electro-optic effect exaltation on lithium niobate photonic crystals due to slow photons. *Appl. Phys. Lett.*, 89(24):241110, 2006.

[52] Bartos CHMIELAK, Michael WALDOW, Christopher MATHEISEN, Christian RIPPERDA, Jens BOLTEN, Thorsten WAHLBRINK, Michael NAGEL, Florian MERGET et Heinrich KURZ : Pockels effect based fully integrated, strained silicon electro-optic modulator. *Opt. Express*, 19(18):17212–17219, 2011.

[53] RR SUBKHANGULOV, RV MIKHAYLOVSKIY, AK ZVEZDIN, VV KRUGLYAK, Th RASING et AV KIMEL : Terahertz modulation of the faraday rotation by laser pulses via the optical kerr effect. *Nat. Photon*, 2016.

[54] Mohammed F SALEH, Wonkeun CHANG, John C TRAVERS, Philip St J RUSSELL et Fabio BIANCALANA : Plasma-induced asymmetric self-phase modulation and modulational instability in gas-filled hollow-core photonic crystal fibers. *Phys. Rev. Lett.*, 109(11):113902, 2012.

[55] Vivek VENKATARAMAN, Kasturi SAHA et Alexander L GAETA : Phase modulation at the few-photon level for weak-nonlinearity-based quantum computing. *Nat. Photon*, 7(2):138–141, 2013.

[56] Robert OLSHANSKY, Vincent A LANZISERA et Paul M HILL : Subcarrier multiplexed lightwave systems for broad-band distribution. *J. Lightwave Technol.*, 7(9):1329–1342, 1989.

[57] Ji Hoon JEON, Ho-Young JOO, Young-Min KIM, Duk Hyun LEE, Jin-Soo KIM, Yeon Soo KIM, Taekjib CHOI et Bae Ho PARK : Selector-free resistive switching memory cell based on bifeo3 nano-island showing high resistance ratio and nonlinearity factor. *Sci. Rep.*, 6, 2016.

[58] Peng HUANG, Jinfeng KANG, Yudi ZHAO, Sijie CHEN, Runze HAN, Zheng ZHOU, Zhe CHEN, Wenjia MA, Mu LI, Lifeng LIU *et al.* : Reconfigurable nonvolatile logic operations in resistance switching crossbar array for large-scale circuits. *Adv. Mater.*, 28(44):9758–9764, 2016.

[59] Somenath DUTTA, Tanmoy DATTA, Mrinal SEN et Arpan DEYASI : Design of efficient photonic coupler structures for lumped raman amplification in silicon waveguides. *In Devices, Circuits and Communications (ICDCCom), 2014 International Conference on*, pages 1–4. IEEE, 2014.

[60] John COVEY, Aaron D FINKE, Xiaochuan XU, Wenzhi WU, Yaguo WANG, François DIEDERICH et Ray T CHEN : All-optical switching with 1-ps response time in a ddmebt enabled silicon grating coupler/resonator hybrid device. *Opt. Express*, 22(20):24530–24544, 2014.

[61] Wanjun ZHENG, Shuangchen RUAN, Min ZHANG, Wenli LIU, Yingying ZHANG et Xi YANG : Switchable multi-wavelength erbium-doped photonic crystal fiber laser

based on nonlinear polarization rotation. *Optics & Laser Technology*, 50:145–149, 2013.

[62] Yuzo SASAKI, Yuichi OKABE, Masahiro UENO, Seiji TOYODA, Junya KOBAYASHI, Shogo YAGI et Kazunori NAGANUMA : Resolution enhancement of kta1-xnbxo3 electro-optic deflector by optical beam shaping. *Appl. Phys. Express*, 6(10):102201, 2013.

[63] Imed MHAOUECH, Virginie CODA, Germano MONTEMEZZANI, Mathieu CHAUVET et Laurent GUILBERT : Low drive voltage electro-optic bragg deflector using a periodically poled lithium niobate planar waveguide. *Opt. Lett.*, 41(18):4174–4177, 2016.

[64] Peng ZU, Chi Chiu CHAN, Wen Siang LEW, Limin HU, Yongxing JIN, Hwi Fen LIEW, Li Han CHEN, Wei Chang WONG et Xinyong DONG : Temperature-insensitive magnetic field sensor based on nanoparticle magnetic fluid and photonic crystal fiber. *IEEE Photon. J.*, 4(2):491–498, 2012.

[65] Huihui LU, Benattou SADANI, Gwenn ULLIAC, Clement GUYOT, Nadège COURJAL, Manuel COLLET, Fadi Issam BAIDA et Maria-Pilar BERNAL : Integrated temperature sensor based on an enhanced pyroelectric photonic crystal. *Opt. Express*, 21(14):16311–16318, 2013.

[66] B TAN et K VENKATAKRISHNAN : A femtosecond laser-induced periodical surface structure on crystalline silicon. *J. Micromech. Microeng.*, 16(5):1080, 2006.

[67] Robert G LINDQUIST : Wavelength selective cross-connect switch using a mems shutter array, mars 18 2003. US Patent 6,535,311.

[68] Yu-xin QIN, Jing-qiu LIANG, Zhong-zhu LIANG, Chao TIAN, Jin-guang LÜ et Wei-biao WANG : Design and experimental research on a visible-near infrared spatial

modulating fourier transform spectrometer based on micro multi-step mirrors. *Optoelectron Lett.*, 10:172–175, 2014.

[69] David K BIEGELSEN, Gary K STARKWEATHER et James C ZESCH : Acousto-optic modulation device, février 17 1976. US Patent 3,938,881.

[70] Semere A TADESSE, Huan LI, Qiyu LIU et Mo LI : Acousto-optic modulation of a photonic crystal nanocavity with lamb waves in microwave k band. *Appl. Phys. Lett.*, 107(20):201113, 2015.

[71] Hong-Sik JUNG : Electro-optic electric field sensor utilizing ti: Linbo 3 symmetric mach-zehnder interferometers. *J Opt Soc Korea*, 16(1):47–52, 2012.

[72] Youfu GENG, Xuejin LI, Xiaoling TAN, Yuanlong DENG et Xueming HONG : Compact and ultrasensitive temperature sensor with a fully liquid-filled photonic crystal fiber mach–zehnder interferometer. *IEEE Sens. J.*, 14(1):167–170, 2014.

[73] Toshihiko BABA : Slow light in photonic crystals. *Nat. Photon*, 2(8):465–473, 2008.

[74] Lanlan GU, Wei JIANG, Xiaonan CHEN, Li WANG et Ray T CHEN : High speed silicon photonic crystal waveguide modulator for low voltage operation. *Appl. Phys. Lett.*, 90(7):071105, 2007.

[75] C BOSSHARD, M CANVA, L DALTON, U GUBLER, J-I JIN, H-K SHIM, GI STEGEMAN et K-S LEE : *Polymers for Photonics Applications I*, volume 158. Springer Science & Business Media, 2002.

[76] Y ENAMI, CT DEROSE, D MATHINE, C LOYCHIK, C GREENLEE, Robert A NORWOOD, TD KIM, J LUO, Y TIAN, AK-Y JEN *et al.* : Hybrid polymer/sol–gel waveguide modulators with exceptionally large electro–optic coefficients. *Nat. Photon*, 1(3):180–185, 2007.

[77] Christian KOOS, Philipp VORREAU, Thomas VALLAITIS, Pieter DUMON, Wim BOGAERTS, Roel BAETS, Bweh ESEMBESON, Ivan BIAGGIO, Tsuyoshi MICHINOBU, François DIEDERICH *et al.* : All-optical high-speed signal processing with silicon–organic hybrid slot waveguides. *Nat. Photon*, 3(4):216–219, 2009.

[78] Ansheng LIU, Richard JONES, Ling LIAO, Dean SAMARA-RUBIO, Doron RUBIN, Oded COHEN, Remus NICOLAESCU et Mario PANICCIA : A high-speed silicon optical modulator based on a metal–oxide–semiconductor capacitor. *Nature*, 427(6975):615–618, 2004.

[79] Jan Hendrik WÜLBERN, Jan HAMPE, Alexander PETROV, Manfred EICH, Jingdong LUO, Alex K-Y JEN, Andrea DI FALCO, Thomas F KRAUSS et Jürgen BRUNS : Electro-optic modulation in slotted resonant photonic crystal heterostructures. *Appl. Phys. Lett.*, 94(24):241107, 2009.

[80] M SCHMIDT, M EICH, U HUEBNER et R BOUCHER : Electro-optically tunable photonic crystals. *Appl. Phys. Lett.*, 87(12):121110, 2005.

[81] RICHARDA SOREF et BRIANR BENNETT : Electrooptical effects in silicon. *IEEE J. Quantum Electron.*, 23(1):123–129, 1987.

[82] Qianfan XU, Bradley SCHMIDT, Sameer PRADHAN et Michal LIPSON : Micrometre-scale silicon electro-optic modulator. *nature*, 435(7040):325–327, 2005.

[83] Tatyana VOLK et Manfred WÖHLECKE : *Lithium niobate: defects, photorefraction and ferroelectric switching*, volume 115. Springer Science & Business Media, 2008.

[84] Huihui LU, Benattou SADANI, Gwenn ULLIAC, Nadège COURJAL, Clément GUYOT, J-M MEROLLA, Manuel COLLET, Fadi Issam BAIDA et M-P BERNAL : 6-micron interaction length electro-optic modulation based on lithium niobate photonic crystal cavity. *Opt. Express*, 20(19):20884–20893, 2012.

[85] H Lu, B Sadani, N Courjal, G Ulliac, N Smith, V Stenger, M Collet, FI Baida et M-P Bernal : Enhanced electro-optical lithium niobate photonic crystal wire waveguide on a smart-cut thin film. *Opt. Express*, 20(3):2974–2981, 2012.

[86] Wentao Qiu, Abdoulaye Ndao, Venancio Calero Vila, Roland Salut, Nadège Courjal, Fadi Issam Baida et Maria-Pilar Bernal : Fano resonance-based highly sensitive, compact temperature sensor on thin film lithium niobate. *Opt. Lett.*, 41(6):1106–1109, 2016.

[87] Wentao Qiu, Abdoulaye Ndao, Huihui Lu, Maria-Pilar Bernal et Fadi Issam Baida : Guided resonances on lithium niobate for extremely small electric field detection investigated by accurate sensitivity analysis. *Opt. Express*, 24(18):20196–20209, 2016.

[88] Shangping Guo et Sacharia Albin : Simple plane wave implementation for photonic crystal calculations. *Opt. Express*, 11(2):167–175, 2003.

[89] Shouyuan Shi, Caihua Chen et Dennis W. Prather : Plane-wave expansion method for calculating band structure of photonic crystal slabs with perfectly matched layers. *J. Opt. Soc. Am. A*, 21(9):1769, septembre 2004.

[90] C. M. Soukoulis, éditeur. *Photonic Band Gaps and Localization*, volume 308 de *NATO ASI Series*. Springer US, Boston, MA, 1993.

[91] Charalambos C. Katsidis et Dimitrios I. Siapkas : General transfer-matrix method for optical multilayer systems with coherent, partially coherent, and incoherent interference. *Appl. Opt.*, 41(19):3978, juillet 2002.

[92] MG Moharam et TK Gaylord : Rigorous coupled-wave analysis of grating diffractionŮe-mode polarization and losses. *JOSA*, 73(4):451–455, 1983.

[93] Philippe LALANNE et G. Michael MORRIS : Highly improved convergence of the coupled-wave method for TM polarization. *JOSA A*, 13(4):779–784, 1996.

[94] Karl S KUNZ et Raymond J LUEBBERS : *The finite difference time domain method for electromagnetics*. CRC press, 1993.

[95] Attila MEKIS, Shanhui FAN et J. D. JOANNOPOULOS : Absorbing boundary conditions for FDTD simulations of photonic crystal waveguides. *IEEE Microw. Guided Wave Lett.*, 9(12):502–504, 1999.

[96] A. TAFLOVE et S.C. HAGNESS : *Computational Electrodynamics: The Finite-difference Time-domain Method*. Artech House antennas and propagation library. Artech House, 2005.

[97] Kurt L. SHLAGER et John B. SCHNEIDER : A survey of the finite-difference time-domain literature. *Advances in Computational Electrodynamics: The Finite-Difference Time-Domain Method*, 1:1–62, 1998.

[98] Lin ZSCHIEDRICH, Sven BURGER, Benjamin KETTNER et Frank SCHMIDT : Advanced finite element method for nano-resonators. *In Integrated Optoelectronic Devices 2006*, pages 611515–611515. SPIE, 2006.

[99] Jan POMPLUN, Sven BURGER, Lin ZSCHIEDRICH et Frank SCHMIDT : Adaptive finite element method for simulation of optical nano structures. *Phys. Status Solidi B*, 244(10):3419–3434, octobre 2007.

[100] Gerrit MUR : Absorbing boundary conditions for the finite-difference approximation of the time-domain electromagnetic-field equations. *IEEE Trans. Electromagn. Compat.*, (4):377–382, 1981.

[101] Jean-Pierre BERENGER : A perfectly matched layer for the absorption of electromagnetic waves. *J. Comput. Phys.*, 114(2):185–200, 1994.

[102] Raymond J LUEBBERS et Forrest HUNSBERGER : Fdtd for n th-order dispersive media. *IEEE Trans. Antennas. Propag.*, 40(11):1297–1301, 1992.

[103] Zachary S SACKS, David M KINGSLAND, Robert LEE et Jin-Fa LEE : A perfectly matched anisotropic absorber for use as an absorbing boundary condition. *IEEE Trans. Antennas. Propag.*, 43(12):1460–1463, 1995.

[104] David F KELLEY et Raymond J LUEBBERS : Piecewise linear recursive convolution for dispersive media using fdtd. *IEEE Trans. Antennas. Propag.*, 44(6):792–797, 1996.

[105] J Alan RODEN et Stephen D GEDNEY : Convolutional pml (cpml): An efficient fdtd implementation of the cfs-pml for arbitrary media. *Microw. Opt. Technol. Lett.*, 27(5):334–338, 2000.

[106] Peter M. GOORJIAN et Allen TAFLOVE : Direct time integration of maxwell's equations in nonlinear dispersive media for propagation and scattering of femtosecond electromagnetic solitons. *Opt. Lett.*, 17(3):180, février 1992.

[107] Guowu ZHENG et Kangsheng CHEN : Transient analysis of microstrip lines with ferrite substrate by extended fd-td method. *Int J Infrared Millimeter Waves*, 13(8): 1115–1125, 1992.

[108] P. TRAN : Photonic-band-structure calculation of material possessing Kerr nonlinearity. *Phys. Rev. B*, 52(15):10673, 1995.

[109] Youg XU, Reginald K. LEE et Amnon YARIV : Propagation and second-harmonic generation of electromagnetic waves in a coupled-resonator optical waveguide. *JOSA B*, 17(3):387–400, 2000.

[110] Matthieu ROUSSEY, Maria-Pilar BERNAL, Nadège COURJAL et Fadi I BAIDA : Experimental and theoretical characterization of a lithium niobate photonic crystal. *Appl. Phys. Lett.*, 87(24):1101, 2005.

[111] Y.R. SHEN : *The Principles of Nonlinear Optics*. Pure & Appl. Opt. Series: 1-349. Wiley, 1984.

[112] Richard COURANT, Kurt FRIEDRICHS et Hans LEWY : On the partial difference equations of mathematical physics. *IBM journal*, 11(2):215–234, 1967.

[113] Charles KITTEL, Paul MCEUEN, Julie DION et Paul MCEUEN : *Physique de l'état solide: cours et problèmes*. Dunod, 2007.

[114] YU PETER et Manuel CARDONA : *Fundamentals of semiconductors: physics and materials properties*. Springer Science & Business Media, 2010.

[115] Lukas NOVOTNY et Bert HECHT : *Principles of nano-optics*. Cambridge university press, 2012.

[116] Pablo G ETCHEGOIN, EC LE RU et M MEYER : An analytic model for the optical properties of gold. *J. Chem. Phys.*, 125(16):164705, 2006.

[117] Alexandre VIAL et Thierry LAROCHE : Description of dispersion properties of metals by means of the critical points model and application to the study of resonant structures using the FDTD method. *J. Phys. D: Appl. Phys.*, 40(22):7152–7158, novembre 2007.

[118] Rose M JOSEPH, Susan C HAGNESS et Allen TAFLOVE : Direct time integration of maxwell's equations in linear dispersive media with absorption for scattering and propagation of femtosecond electromagnetic pulses. *Opt. Lett.*, 16(18):1412–1414, 1991.

[119] G. PARENT, D. VAN LABEKE et F. I. BAIDA : Theoretical study of transient phenomena in near-field optics. *J. Microsc*, 202(2):296–306, 2001.

[120] Alexandre VIAL, Anne-Sophie GRIMAULT, Demetrio MACÍAS, Dominique BARCHIESI et Marc Lamy de LA CHAPELLE : Improved analytical fit of gold dispersion: Application to the modeling of extinction spectra with a finite-difference time-domain method. *Phys. Rev. B*, 71(8):085416, 2005.

[121] W KO et R MITTRA : Implementation of floquet boundary condition in fdtd for fss analysis. *In Antennas and Propagation Society International Symposium, 1993. AP-S. Digest*, pages 14–17. IEEE, 1993.

[122] Paul HARMS, Raj MITTRA et Wai KO : Implementation of the periodic boundary condition in the finite-difference time-domain algorithm for fss structures. *IEEE Trans. Antennas. Propag.*, 42(9):1317–1324, 1994.

[123] A BELKHIR et FI BAIDA : Three-dimensional finite-difference time-domain algorithm for oblique incidence with adaptation of perfectly matched layers and nonuniform meshing: Application to the study of a radar dome. *Phys. Rev. E*, 77(5):056701, 2008.

[124] Elie M ATIE, Tony TANNOUS, Thierry GROSJEAN et Fadi I BAIDA : High optical resonance sensitivity to its environment of a fibered bowtie nano-aperture antenna. *Appl. Phys. B*, 120(4):581–586, 2015.

[125] Mathieu MIVELLE, I Abdoulkader IBRAHIM, F BAIDA, GW BURR, D NEDELJKOVIC, D CHARRAUT, JY RAUCH, R SALUT et T GROSJEAN : Bowtie nano-aperture as interface between near-fields and a single-mode fiber. *Opt. Express*, 18(15):15964–15974, 2010.

[126] Christoph MENZEL, Erik HEBESTREIT, Stefan MÜHLIG, Carsten ROCKSTUHL, Sven BURGER, Falk LEDERER et Thomas PERTSCH : The spectral shift between near-and far-field resonances of optical nano-antennas. *Opt. Express*, 22(8):9971–9982, 2014.

[127] Renaud BACHELOT, Carole ECOFFET, Denis DELOEIL, Pascal ROYER et Daniel-Joseph LOUGNOT : Integration of micrometer-sized polymer elements at the end of optical fibers by free-radical photopolymerization. *Appl. Opt.*, 40(32):5860–5871, 2001.

[128] Wolfgang SELLMEIER : Zur erklärung der abnormen farbenfolge im spectrum einiger substanzen. *Annalen der Physik und Chemie*, 219(6):272–282, 1871.

[129] RS WEIS et TK GAYLORD : Lithium niobate: summary of physical properties and crystal structure. *Appl. Phys. A*, 37(4):191–203, 1985.

[130] U SCHLARB et K BETZLER : Refractive indices of lithium niobate as a function of wavelength and composition. *Journal of applied physics*, 73(7):3472–3476, 1993.

[131] Amnon YARIV et Pochi YEH : Optical waves in crystal propagation and control of laser radiation. 1983.

[132] M IZDEBSKI, W KUCHARCZYK et RE RAAB : On relationships between electro-optic coefficients for impermeability and nonlinear electric susceptibilities. *J. Opt. A Pure Appl. Op.*, 6(4):421, 2004.

[133] Ivana KOVACIC et Michael J BRENNAN : *The Duffing equation: nonlinear oscillators and their behaviour*. John Wiley & Sons, 2011.

## Abstract:

Our research is concerned with the optical response of nano-structures by modeling them in order to enhance the confinement of light in these structures, which leads to the exaltation of linear and nonlinear optical effects.
Our work is divided into two sections, which are based on the enhancement of the electric field inside the structure. In the first section, we study the optical properties of a Bowtie Nano-aperture, BNA, as a function of the refractive index of the surrounding medium. The study discusses the variation of the resonance wavelength and the intensity of the enhanced field in the gap of the BNA as a function of the distance from a sample placed in front of our BNA. The BNA is engraved at the apex of a metallic coated fiber tip. In this section a theoretical study was achieved using the Finite Difference Time Domain method FDTD in which we implement a Drude dispersion model to faithfully describe the optical properties of metals. In addition, a validating experimental study was achieved and a high accordance between both results is recorded.
In the second section, the electro optical effect of nano-structures is studied. Electro-optical effect or Pockels effect is the variation of the refractive index of a nonlinear media as a function of an applied external electric field. The electro-optical effect is a linear variation of the media refractive index. However it is also related to the second order nonlinear susceptibility tensor, thus it becomes a nonlinear effect that only occurs in non-centrosymetric material. In our study we chose the case of a nano-structure fabricated with Lithium Niobate. Lithium Niobate is widely used in photonic applications due to its electro-optical, acousto-optical and nonlinear optical properties. We present a theoretical study of the electro-optical effects using the FDTD simulation method. We started by approving the ability to use the FDTD to calculate the refractive index variation in bulk Lithium Niobate then we suggest different approximations to estimate the refractive index variation when the light is confined inside the structure. In addition we suggest a new self-consistent method in which the variation of the refractive index is modified during the simulation. The study shows a comparison between different assumptions (used in previous research) and the self-consistent method for various structures, like Bragg reflectors, cavity structures and 2D photonic crystals. The study shows that the difference between the results of each assumption becomes greater when the optical confinement in the structure becomes more important.

**Keywords:** Bowtie aperture, photonic crystal FDTD, electro-optic effect

SPIM

■ École doctorale SPIM 1 rue Claude Goudimel F - 25030 Besançon cedex
■ tél. +33 (0)3 81 66 66 02 ■ ed-spim@univ-fcomte.fr ■ www.ed-spim.univ-fcomte.fr

UFC UNIVERSITÉ DE FRANCHE-COMTÉ

UNIVERSITY OF BALAMAND